ACIBADEM MEHMET ALİ AYDINLAR UNIVERSITY

GRADUATE SCHOOL OF NATURAL AND APPLIED SCIENCES

DEVELOPMENT OF TARGETED AND PEEL-OFF NANO DRUG DELIVERY SYSTEMS FOR TREATMENT OF NEUROINFLAMMATION

BEYZA DÖNMÜŞ

M.Sc. THESIS

DEPARTMENT OF BIOMATERIALS

SUPERVISOR

Assoc. Prof. Özgül Gök Özatay

ISTANBUL-2025

ACIBADEM MEHMET ALİ AYDINLAR UNIVERSITY

GRADUATE SCHOOL OF NATURAL AND APPLIED SCIENCES

DEVELOPMENT OF TARGETED AND PEEL-OFF NANO DRUG DELIVERY SYSTEMS FOR TREATMENT OF NEUROINFLAMMATION

BEYZA DÖNMÜŞ

M.Sc. THESIS

DEPARTMENT OF BIOMATERIALS

SUPERVISOR

Assoc. Prof. Özgül Gök Özatay

ISTANBUL-2025

DECLARATION

I declare that this thesis work is my own work, I had no unethical behavior at any stages from the planning to the writing of the thesis, I obtained all the information in this thesis in accordance with academic and ethicel rules, I cited all the information and comments that were not obtained with this thesis work, and I provided resources in the list of references. I also declare that there was no violation of any patents and copyrights during the study and writing of this thesis.

03/02/2025

Beyza Dönmüş

PREFACE AND ACKNOWLEDGEMENT

Firstly, I would like to express my profound gratitude to my thesis advisor and academic idol, Assoc. Prof. Dr. Özgül Gök Özatay, for her unwavering support throughout this entire process and for her invaluable contributions to my academic development. I consider myself extremely fortunate to have had her as a guiding light throughout my journey since 2018 when our paths first crossed. Her guidance has expanded my horizons and has shaped my vision.

Moreover, I am grateful to all former and present GOK Research Group members who have always supported me as a second family. I will always be grateful to all of them for making my master's journey truly unique for me. I am deeply thankful to Begüm Ceren Bacınoğlu, Onurhan Yorulmaz, Çiğse Yıldırım, Engin Kemal Seven, and Zeynep Bacın for being the most supportive friends in the world for 13 years. I would also like to express my gratitude to my academic brother, Anılcan Kuş, who has always supported me and never lost faith in me, and to Serhat Bayrak, who has been by my side throughout this entire process, my greatest supporter, and my safe place. I feel so lucky to have you all in my life!

I would like to express my profound gratitude to my parents, Gülhiz Dönmüş ve Birol Dönmüş, to my brother Karan Dönmüş, to my grandmother Şükran Özkan, and to my grandfather Fahri Özkan for their unconditional and selfless love, their trust and unwavering support in every moment of my life, and for shaping me into the person I am today. They have always been my greatest source of motivation and driving force.

This thesis project was supported by both TÜBİTAK 1001 (title with "Nöroinflamasyona Bağlı Sinir Hücre Hasarının Tedavisi İçin Beyine Hedefli ve Soyulabilir Akıllı Nanoterapilerin Geliştirilmesi," project no. 122S724) and Acıbadem Mehmet Ali Aydınlar University Scientific Research Projects Commission (ABAPKO,

titled “Nöroinflamasyona Yönelik Hedefli ve Soyulabilir Nano İlaç Taşıma Sistemleri Geliştirilmesi,” project no. FYL-2024-2156).

TABLE OF CONTENTS

DECLARATION ..... **i**
PREFACE AND ACKNOWLEDGEMENT ..... **ii**
TABLE OF CONTENTS ..... **iv**
LIST OF ABBREVIATIONS AND SYMBOLS ..... **vi**
LIST OF FIGURES ..... **xi**
LIST OF TABLES ..... **xv**
ÖZET **1**
SUMMARY **2**
1. INTRODUCTION AND AIM **3**
2. BACKGROUND **5**
2.1 Drug Delivery Systems 5
2.2 Nanoparticles 10
2.3 Polymeric Nanoparticles 13
2.3.1 Chitosan Nanoparticles 15
2.4 Functionalızation Methods 17
2.4.1 Surface Modification Strategies 17
2.4.2 Conjugation via Cleavable Bonds 18
2.5 Neuroinflammation 18
2.5.1 Blood Brain Barrier (BBB) 20
2.5.2 BBB Penetrating Peptides 22
3. MATERIALS AND METHODS **25**
3.1 Materials 25
3.2 Nanoparticle Preparation and Characterization 25
3.2.1 Preparation and Characterization of Chitosan Nanoparticles (Ch-NPs) 25
3.2.2 Drug Loaded Polymer and Nanoparticle Preparation (LA-Ch-NPs) 27
3.2.3 Preparation of the Flourescent Dye Conjugated Nanoparticles (Cy3-Ch-NPs) 31
3.2.4 Preparation of Targeted Nanoparticles 32

3.2.5 Characterization of NPs 42
3.3 In-Vitro Experiments 43
3.3.1 In Vitro Cytotoxicity Assay (CCK-8) 43
4. RESULTS 45
4.1 Nanoparticle Preparation and Characterization 45
4.1.1 Preparation and Characterization of Chitosan Nanoparticles (Ch-NPs) 45
4.1.2 Drug Loaded Polymer and Nanoparticle Preparation (LA-Ch-NPs) 60
4.1.3 Preparation of the Flourescent Dye Conjugated Nanoparticles (Cy3-Ch-NPs) 65
4.1.4 Preparation of Targeted Nanoparticles 68
4.2 In Vitro Experiments 81
4.2.1 In Vitro Cytotoxicity Assay (CCK-8) 81
5. DISCUSSION 84
6. CONCLUSION 91
7. REFERENCES 92
8. APPENDIX 106
9. CURRICULUM VITAE 109

LIST OF ABBREVIATIONS AND SYMBOLS

^{1}H-NMR	Proton nuclear magnetic resonance
α-LA	Alpha Lipoic Acid
α-LA-Ch	Alpha Lipoic Acid conjugated Chitosan polymer
ACN	Acetonitrile
Ant-Ch-NPs	Antibody conjugated Chitosan nanoparticles
BBB	Blood Brain Barrier
BCA	Bicinchoninic Acid Assay
CCK-8	Cell Counting Kit-8
CD11b-T7- LA-Ch-NPs	Antibody and peptide conjugated drug loaded nanoparticles
CNS	Central Nervous System
Ch	Chitosan
Ch-NP	Chitosan Nanoparticles
Cy3	Cyanine-3 flourescent dye
Cy3-CD11b-Ch-NP	Cy3 and antibody conjugated nanoparticles
Cy3-Ch-NP	Cy3 conjugated nanoparticles
ddH_2O	Double distilled water
DDS	Drug Delivery System
DIC	N,N'-Diisopropylcarbodiimide
DLS	Dynamic light scattering
DMEM/F-12	Dulbecco's Modified Eagle Medium F-12 Nutrient Mixture
DMF	N,N'-Dimethylformamide

DMSO	Dimethyl sulfoxide
EPR	Enhanced permeability and retention
Et_3N	Triethylamine
FBS	Fetal Bovine Serum
FDA	US Food and Drug Administration
FT-IR	Fourier transform infrared spectroscopy
HPLC	High performance liquid chromotography
LA-Ch-NP	LA conjugated chitosan nanoparticles
LC/MS-MS	Liquid chromotography/mass spectrometry-mass spectrometry
MDR	Multi Drug Resistance
NPs	Nanoparticles
PBS	Phosphate buffer saline
PDI	Polydispersity index
PEG	Poly(ethylene glycol)
PES	Polyethersulfone
RT	Room temperature
SEM	Scanning electron microscopy
T7-LA-Ch-NPs	Peptide conjugated drug loaded nanoparticles
T7-PEG-ss-NHS	Peptide conjugated polymer
TEM	Transmission electron microscopy
TFA	Trifluoroacetic acid
TIS	Triisopropylsilane
TfR	Transferrin receptor

LIST OF FIGURES

Figure 2.1. Types of targeted drug delivery systems (15). 7
Figure 2.2. Different types of ligands for active targeting of nanoparticles (21). 9
Figure 2.3. Different types of nanocarriers depending on their dimension (41). 11
Figure 2.4. Biological, chemical, physical and surface properties of NPs (created with Biorender.com). 12
Figure 2.5. Overview of advantages and challenges of the PNPs (56). 14
Figure 2.6. Chemical structure of the Chitosan. 16
Figure 2.7. Schematic representation of the neurovascular unit comprising endothelial cells, pericytes, astrocytes, and microglia, regulates brain function and forms the structural basis of the blood-brain barrier (100). 21
Figure 2.8. The BBB structure and the different transport mechanisms. (A) The structure of the BBB, (B) Different transport mechanism to the CNS through the BBB (103). 22
Figure 3.1. The chemical structure of α-Lipoic Acid conjugated chitosan polymer. 29
Figure 3.2. Chemical structure of Cy3-NHS ester dye molecule. 31
Figure 3.3. Solid phase peptide synthesis (SPSS) method and steps (122). 33
Figure 3.4. Synthesis steps of the T7-PEG-$_{S\text{-}S}$-NHS functional polymer. 38
Figure 3.5. Summary of the CD11b-T7-LA-Ch-NPs. (created with Biorender.com). 42
Figure 4.1. Effect of the molecular weight to the NP size. Comparison of nanoparticles prepared with low and medium molecular weight polymer at 1:1 Polymer:Crosslinker ratio. **(A)** NPs prepared with 0.1% low molecular weight chitosan at 1:1 ratio; **(B)** NPs prepared with 0.1% medium molecular weight chitosan at 1:1 ratio. 46
Figure 4.2. Effect of the molecular weight to the NP size. Comparison of nanoparticles prepared with low and medium molecular weight polymer at 1:0.5 Polymer:Crosslinker ratio. **(A)** NPs prepared with 0.1% low molecular weight chitosan at 1:0.5 ratio; **(B)** NPs prepared with 0.1% medium molecular weight chitosan at 1:0.5 ratio. 47

Figure 4.3. Effect of the reaction time to the NP size. Comparison of nanoparticles prepared with low molecular weight polymer with 1:0.5 and 1:1 [C]:[T] ratios at different time intervals. (A) NP prepared with 1:1 ratio of 0.1% Low molecular weight chitosan and 0,05% STPP in 30 min; (B) NP prepared with 1:1 ratio of 0,1% Low molecular weight chitosan and 0.05% STPP in 60 min; (C) NP prepared with 1:0.5 ratio of 0,1% Low molecular weight chitosan and 0,05% STPP in 30 min; (D) NP prepared with 1:0.5 ratio of 0,1% Low molecular weight chitosan and 0,05% STPP in 60 min. 48

Figure 4.4. Effect of the polymer concentration to the NP size. Comparison of nanoparticles prepared with 0,05 wt% STPP and 0,05 wt% polymer at 1:0.5 and 1:1 [C]:[T] ratios for 60 min. (A) NP prepared with 0,05 wt% low molecular weight chitosan at 1:1 ratio; (B) NP prepared with 0.05 wt% low molecular weight chitosan at 1:0.5 ratio. 54

Figure 4.5. Effect of the polymer concentration to the NP size. Comparison of nanoparticles prepared with 0,05 wt% STPP and 0,1 wt% polymer at 1:0.5 and 1:1 [C]:[T] ratios for 60 min. (A) NP prepared with 0,1 wt% low molecular weight chitosan at 1:1 ratio; (B) NP prepared with 0.1 wt% low molecular weight chitosan at 1:0.5 ratio. 54

Figure 4.6. Effect of the crosslinking concentration to the NP size. Comparison of nanoparticles prepared with 0,1 wt% polymer and 0,01 wt% STPP at 1:0.5 and 1:1 [C]:[T] ratios for 60 min. (A) NP prepared with 0,01 wt% STPP at 1:1 ratio; (B) NP prepared with 0,01 wt.% STPP at 1:0.5 ratio. 55

Figure 4.7. Zeta potential measurement of Ch-NPs. 56

Figure 4.8. Comparative FT-IR spectra for chitosan nanoparticles (Ch-NPs). 57

Figure 4.9. Proton NMR spectrum (in D_2O) for chitosan nanoparticle (Ch-NP)..... 58

Figure 4.10. Morphological analysis results of Ch-NPs. (A) TEM microgpraph, (B) SEM micrograph. 59

Figure 4.11. Time-dependent stability results of Ch-NPs at two different pH values. 60

Figure 4.12. ^{1}H-NMR spectrum for lipoic acid conjugated chitosan polymer (α-LA-Ch). 62

Figure 4.13. Comparative FT-IR spectra for the lipoic acid conjugated chitosan polymer (α-LA-Ch). 62
Figure 4.14. Effect of the crosslinking concentration to the drug loaded nanoparticle size. Comparison of nanoparticles prepared with 0,1 wt% polymer and 0,01 wt% STPP at 1:0.5 and 1:1 [C]:[T] ratios for 60 min. (A) NP prepared with 0,01 wt% STPP at 1:1 ratio; (B) NP prepared with 0,01 wt.% STPP at 1:0.5 ratio. 63
Figure 4.15. Zeta potential measurement of LA-Ch-NPs. 64
Figure 4.16. Time dependent drug-release profile of LA-Ch-NPs after incuation in pH 7.4 PBS, pH 5.5 AB, pH 5.5 AB + esterase, and pH 7.4 PBS + esterase for 30 days. 65
Figure 4.17. Cy3 conjugated NP (Cy3-Ch-NP) ultra-filtered using Amicon filters with Mwt cut-off: 100 kDa for 3 min at 2500 rpm, centrifuged 3 times with ddH_2O. 66
Figure 4.18. Zeta potential measurement of Cy3-Ch-NPs. 67
Figure 4.19. Morphological analysis results of Cy3-Ch-NPs. (A) TEM microgpraph, (B) SEM micrograph. 68
Figure 4.20. HPLC chromotogram of T7 peptide. 68
Figure 4.21. LC-MS/MS chromatograms of T7 peptide. 69
Figure 4.22. ^{1}H-NMR spectrum for T7 peptide (in DMSO-d_6). 70
Figure 4.23. FT-IR spectrum of the T7 peptide. 71
Figure 4.24. HPLC chromotogram of the Amine-PEG-Thiol conjugate. 73
Figure 4.25. FT-IR spectrum of the Amine-PEG-Thiol conjugate. 73
Figure 4.26. HPLC chromotogram of the T7-PEG-ss-NHS. 74
Figure 4.27. FT-IR spectrum of the T7-PEG-ss-NHS. 74
Figure 4.28. ^{1}H-NMR spectrum for T7-PEG-ss-NHS (in $CDCl_3$). 76
Figure 4.29. Effect of filtration on the preparation of flourescent labeled microglia targeted nanoparticles (Cy3-CD11b-Ch-NPs). (A) Cy3-CD11b-Ch-NPsultrafiltered by centrifugation with ddH2O 17 times using Amicon filters (Mwt cut-off: 100 kDa) for 3 min at 2500 rpm. (B) Cy3-CD11b-Ch-NPsultrafiltrated by centrifugation with ddH2O 17 times using Amicon filters (Mwt cut-off: 100 kDa) for 3 min at 2500 rpm followed by filtration through a PES (0,22 μm) syringe filter. 76
Figure 4.30. Zeta potential measurement of Cy3-Ant-Ch-NPs. 77

Figure 4.31. Morphological analysis results of Cy3-CD11b-Ch-NPs. (A) TEM microgpraph, (B) SEM micrograph. 78
Figure 4.32. Dual-targeted nanoparticles CD11b-T7- LA-Ch-NPs ultra-filtered using Amicon filters with Mwt cut-off: 100 kDa at 2500 rpm, centrifuged 3 times with ddH_2O..... 79
Figure 4.33. Zeta potential measurement of CD11b-T7- LA-Ch-NPs. 80
Figure 4.34. Time-dependent peel-off test results of T7-PEG conjugated nanoparticles with Glutathione-SH. 81
Figure 4.35. Cytotoxicity based on cell viability vs. dose graph for Ch-NPs, n = 3. 82
Figure 4.36. Cytotoxicity based on cell viability vs. dose graph for T7-PEG-ss-NHS, n = 3. 82
Figure 4.37. Cytotoxicity based on cell viability vs. drug concentration (μM) graph for LA-Ch-NPs and α-Lipoic Acid, n = 3. 83
Figure 8.1. Cy3 dye solutions at different concentrations prepared for the calibration curve.In the photograph, it can be seen that the Cy3 dye, which appears pink at visible wavelength, decreases in pinkness as the concentration decreases from left to right. 106
Figure 8.2. Calibration curve of Cy3 flourescent dye molecule on Vairoskan Flash. 106
Figure 8.3. Calibration curve of Cy3 flourescent dye molecule on Nanodrop spectrophotometer. 107
Figure 8.4. Calibration curve of BSA for BCA assay on Varioskan Flash. 108
Figure 8.5. Calibration curve for BCA protein quantification method using the standards. Standards were prepared from high concentration to low concentration. (1) 2000 μg/mL, (2) 1500 μg/mL, (3) 1000 μg/mL, (4) 750 μg/mL, (5) 500 μg/mL, (6) 250 μg/mL, (7) 125 μg/mL and (8) 0 μg/mL. The prepared Cy3-Ant-Ch-NPs are shown in the section marked with a black box below. 108

LIST OF TABLES

Table 3.1. Amount of amino acids, deprotectors, activators, bases and resins used to synthesize T7 Peptide (HAIYPRH). 33
Table 3.2. Amounts of material used for the cleavage cocktail prepared for the cleavage of T7 Peptide (HAIYPRH). 34
Table 3.3. Chemicals and amounts used in the Cy3-Ant-NP Anti-CD11b binding reaction. 40
Table 4.1. Effect of the reaction time and filtration to the NP size. Comparison of nanoparticles prepared with low molecular weight polymer with 1:0.5 [C]:[T] ratios at different time intervals and filtered using two different filters. 50
Table 4.2. Effect of the reaction time and filtration to the NP size. Comparison of nanoparticles prepared with low molecular weight polymer with 1:1 [C]:[T] ratios at different time intervals and filtered using two different filters. 50
Table 4.3. Effect of the different filters to the NP size.Comparison of nanoparticles prepared with 1:1 and 1:0.5 [C]:[T] ratios containing 0.05% STPP, 0.05% STPP, 0.05% chitosan, 60 min and filtered with different filters. 53
Table 4.4. Size details for imaging agent conjugated nanoparticle (Cy3-Ch-NP). Effect of dye conjugation on the size of nanoparticles containing 0.1% chitosan, 0.01% STPP, prepared with 1:1 [C]:[T] ratio and passed through 1 time Nylon and 1 time PES filter for 60 minutes. 65

ÖZET

Nöroinflamasyona Yönelik Hedefli ve Soyulabilir Nano İlaç Taşıma Sistemleri Geliştirilmesi

Nöroinflamasyon, çeşitli nörolojik bozukluklarda kritik bir rol oynar ve devam etmesi, özellikle travmatik beyin hasarını (TBH) takiben ilerleyen düzeyde nöronal hasara yol açabilir. Geleneksel ilaç taşıma sistemleri (İTS), çok seçici olan kan-beyin bariyerinin (KBB) engelleyici doğası, kullanılan tedavilerde ilaç biyoyararlanımının düşük olması ve istenmeyen hedef dışı etkiler nedeniyle nöroinflamasyonun tedavisinde önemli zorluklarla karşılaşılmaktadır. Bu kısıtlamaların üstesinden gelmek için nanoparçacık (NP) bazlı ilaç taşıma sistemleri, etkili beyin hedefli tedavilerin geliştirilebilmesi için umut verici bir yaklaşım olarak ortaya çıkmaktadır. Sunulan tez projesi, aktif ilaç moleküllerinin bu bariyeri geçmesini ve hasarlı sinir hücrelerinin iyileşmesini sağlayabilecek özel bir ilaç taşıyıcı sistemin geliştirilmesine odaklanmaktadır. Bu çalışmada, anti-enflamatuar ve antioksidan bir ilaç olan α-lipoik asit enkapsüle edilmiş polietilen glikol (PEG) kaplı kitosan bazlı nanoparçacıklar geliştirilmiştir. İlk olarak, PEGile edilmiş T7 peptidi, BBB penetrasyonunu kolaylaştırmak için NP'lerin en dış yüzeyine konjuge edilmiştir. Beyine ulaşan nanoparçacıkların dış katmanındaki PEG kabuğunun, nöroinflamasyona duyarlı bağlarla yüzeye tutturulan PEG zincirlerinin "soyulması" sayesinde, yüzeyinde mikroglia hedefleyici anti-CD11b antikorunu bulunduran nanoparçacıkların açığa çıkması beklenmektedir. Ayrıca, nanoparçacıklar, içinde enkapsüle edilmiş ilaç moleküllerinin inflamasyon bölgesindeki aktive olmuş mikroglialarda yavaş ve sürekli salınımını sağlayacak şekilde optimize edilmiş ve hedeflenen NP'ler sürekli ve kontrollü bir ilaç salım profili göstermiştir. Hücre kültürü çalışmaları, hazırlanan nanopartiküllerin toksik olmadığını göstermiştir. Sonuç olarak, oksidatif stresi ve nöroinflamasyonu azaltarak sinir hücresi hasarını iyileştirmek için özgün bir çift hedefli nano-ilaç taşıma sistemi elde edilmiştir.

Anahtar Kelimeler: Hedefli İlaç Taşıyıcı Sistemler, Nöroinflamasyon, PEGilasyon, Kontrollü İlaç Salımı, Kan Beyin Bariyeri

SUMMARY

Development of Targeted and Peel-Off Nano Drug Delivery Systems for Treatment of Neuroinflammation

Neuroinflammation plays a critical role in various neurological disorders, and its persistence can lead to progressive neuronal damage, particularly following traumatic brain injury (TBI). Conventional drug delivery systems (DDS) face significant challenges in treating neuroinflammation due to the restrictive nature of the blood-brain barrier (BBB), low drug bioavailability, and off-target effects. To overcome these limitations, nanoparticle-based drug delivery has emerged as a promising approach for effective brain-targeted therapy. Within the scope of this thesis, a dual-targeted and peelable NP system was designed for the treatment of neuroinflammation-induced nerve damage. In this study, polyethylene glycol (PEG)-coated chitosan NPs encapsulating α-lipoic acid, an anti-inflammatory and antioxidant drug, were developed. First, a PEGylated T7 peptide was conjugated to the outermost surface of NPs to facilitate BBB penetration. After reaching the brain, the PEG shell was designed to detach in response to the neuroinflammatory environment, exposing an anti-CD11b antibody to direct the NPs toward activated microglia. Cy3 fluorescent dye was used to monitor cellular uptake of NPs and drug release was optimized for pH-sensitive controlled delivery. Cell culture studies demonstrated that the prepared nanoparticles are non-toxic. Furthermore, targeted NPs showed a sustained and controlled drug release profile. Overall, a novel dual-targeted nano-drug delivery system was achieved to reduce oxidative stress and neuroinflammation and, thus, to recover nerve cell damage.

Keywords: Targeted Drug Delivery Systems, Neuroinflammation, PEGylation, Controlled Drug Release, Blood Brain Barrier

1. INTRODUCTION AND AIM

The aim of this thesis is to design a nanoparticle-based platform based on chitosan and PEG chains that can have a more hydrophilic and neutral charge. The nanoparticles were loaded with the active ingredient "α-lipoic acid", a drug with non-steroidal anti-inflammatory and anti-oxidant properties to be used in the treatment of diseases based on brain damage caused by neuroinflammation. This anti-inflammatory drug, which is frequently preferred in treatments, has also been shown in the literature to contribute to cell regeneration by reducing the effect of inflammation on nerve cells, especially due to brain damage (1) . In addition, one of the unique aspects of this design is the targeting of the drug-loaded nanoparticle to the brain and the functionalization of its surface with the T7 peptide that enables it to cross the blood-brain barrier. One novelty of this research project is that the designed drug delivery system is peelable in response to neuroinflammation. While the drug-loaded chitosan nanoparticle structure in the core is used as a drug reservoir, lipoic acid molecules will be attached to the chitosan side branches with hydrolysis-induced cleavable ester bonds to prevent the release of the drug in the systemic circulation and to increase the stability of the drug. In addition, there is no study in the literature in which the drug molecules (α-lipoic acid) that this nanoparticle is intended to carry to active microglia cells are conjugated with any bond that is covalent but can be broken by hydrolysis within the cell. On the other hand, a hydrophilic and highly branched shell was formed by conjugating PEG chains containing disulfide bonds to the surface of this nanoparticle, which can only be broken in the activated region due to neuroinflammation. The T7 peptide covalently bound to the other ends of the PEG chains is predicted to increase the penetration of this drug delivery system and cross the blood-brain barrier. Therefore, it is possible to develop a drug delivery system in which both the PEG chains will break in the brain-targeted and neuroinflammation area and then the chitosan nanoparticle will be loaded with an anti-inflammatory drug that can be released slowly and in a long time.

With this thesis proposal, a drug delivery system that is more advantageous than other nanoparticle-based drug delivery systems published in the literature in terms of polymer-drug combination and neuroinflammation in the brain with a dual targeting group is presented.

2. BACKGROUND

2.1 Drug Delivery Systems

A drug, as defined by the U.S. Food and Drug Administration (FDA), refers to a substance “intended for use in diagnosis, cure, mitigation, treatment, or prevention of disease.” Additionally, drugs are acknowledged as Active Pharmaceutical Ingredient (API) as per official pharmacopeia (2). Drugs are not inherently effective on their own; their effectiveness is dependent on the method of administration. The manner in which a drug is administered affects its absorption, distribution, metabolism, duration of therapeutic effect, excretion, toxicity and pharmacokinetics (PK) (3). Ideally, drugs are supposed to target disease-causing cells precisely at therapeutic concentrations for an effective treatment. In reality, stabil and effective cell or tissue specific targeting are unpredictable and difficult to control for certain reasons. To overcome these challenges, drug delivery systems (DDSs) have been developed (4).

The term “drug delivery system” (DDS) indicates a device or a formulation designed to introduce drugs more effectively into the body for therapeutic purposes.This process involves the application of the therapeutic substance, the release of the active ingredients, and the following transportation of the active ingredients to the site of action (5). The main reason for using an appropriate drug delivery system is the ability to achieve higher and long-lasting drug bioavailability, thus improving therapeutic efficacy. Herein, the objectives and approaches of drug delivery systems can be categorized into three main areas:

1. Choice of delivery route and enhancement of absorption,
2. Controlled release from pharmaceutical formulations,
3. Targeting to the zone of influence (6).

Over the years, the need for DDSs has gained more importance within the developments in the biomaterials field (7–9). The continuous development and design of optimized strategies, including polymers, nanoparticles, dendrimers, liposomes, carbon nanotubes, and other active or passive delivery systems, has revolutionized the way drugs are delivered, and many new strategies continue to be developed and tested. The problems associated with the traditional drug delivery systems, including poor pharmacokinetics, insufficient solubility and rapid degradation of drugs, lack of target specificity, and expensiveness, have led to the need for recent drug delivery systems. Even though drug delivery has progressed significantly in the last 20 years, delivering drugs to specific sites remains a crucial biomedical aspect (10–12). Non-specific drug administration results in poor drug efficacy and undesired side effects in other parts of the body, as deficient amounts of the administered drug reach the target tissue or cell type, causing the drugs to be distributed throughout the body. To overcome these problems, targeted drug delivery systems (TDDSs) are used to deliver drugs to specifically targeted tissues/cells while increasing drug efficacy and reducing side effects (13,14).

The main goal of targeted drug delivery is to achieve high local drug concentrations with low systemic exposure. In this scope, TDDSs can be used for treating a wide range of physiological diseases, such as cancer, diabetes, cardiovascular, diseases and neurodegenerative diseases. Targeting of drugs can be achieved through multiple ways and these ways are divided into subgroups. These pathways are grouped as follows: Active and passive targeting (active targeting alsoclassfied as first, second, third and fourth order targeting); local and systemic targeting; biological, physical, and chemical targeting; inverse, dual, double, and combination targeting (Fig. 2.1).

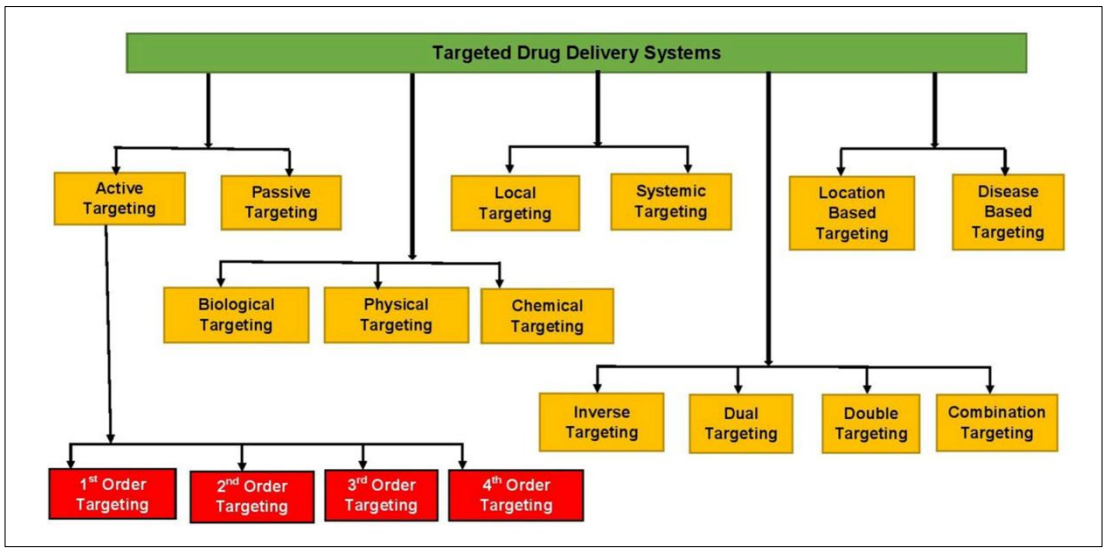

Figure 2.1. Types of targeted drug delivery systems (15).

Passive targeting relies on the unique properties of the tumor vasculature, which is often characterized by a highly permeable structure. (15). This allows nanocarriers to penetrate the tumor blood vessels and accumulate in the tumor tissue due to the Enhanced Permeation and Retention (EPR) effect. The EPR effect improves the delivery of therapeutics encapsulated in nanocarriers, increasing their concentration at the tumor site while minimizing exposure to healthy tissues. This targeted approach aims to improve the effectiveness of cancer treatments and reduce the side effects associated with conventional therapies (16). However, passive targeting approaches have several limitations, such as tumor characteristics variability, poor nanoparticle-cell interactions, and challenges related to PEGylation, resulting in drug expulsion and multidrug resistance (MDR) (16). In order to overcome those limitations, approaches such as the optimization of nanoparticle design, strategies to enhance the EPR effect to increase blood flow and vascular permeability in the tumor, and the combination of passive targeting methods with complementary methods such as active targeting or biological carriers are often used (17,18).

On the other hand, active targeting relies on the interactions of ligands with the receptors expressed on the targeted cell surface. Ligands are one of the most important

surface modification elements in targeted drug delivery systems, along with the physicochemical properties of nanocarriers. This targeting approach facilitates NPs uptake into the targeted cells by using ligands on the nanoparticle surface (Figure 2). They can be chemically conjugated, physically adsorbed or directly bound to other components of the system such as polymers (19). It is crucial to ensure an optimum number of ligand molecules are bound to the surface of the nanocarrier, asthis facilitates effective interaction and enhances the nanocarrier's binding affinity to the receptor site via the multivalent effect.

Biological ligands including antibodies, aptamers, peptides, sugars, small molecules, nucleic acids and lipids, each offering unique advantages in targeting mechanisms (Fig. 2.2). These ligands specifically bind to receptors that are overexpressed on the surfaces of target cells, promoting cellular uptake of nanoparticles carrying drug molecules, reducing side effects and significantly increasing therapeutic efficacy, and delivering a much higher drug concentration to the diseased site. Among these, antibodies are the most widely studied and utilized due to their high specificity and affinity for target antigens, which enhances the precision of drug delivery systems. Antibodies are potent tools which can be engineered to improve their pharmacokinetic properties, allowing for prolonged circulation times and enhanced accumulation at tumor sites through mechanisms such as the EPR effect (20).

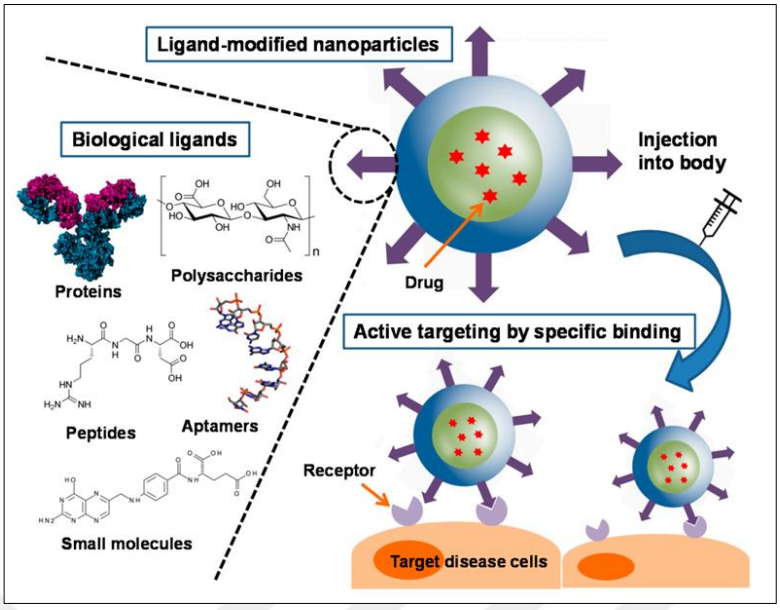

Figure 2.2. Different types of ligands for active targeting of nanoparticles (21).

Another biological ligands, such as aptamers and nucleic acids, have also been intensively studied in recent years. Aptamers offer advantages such as smaller size, lower production costs, biodegradability, ease of chemical modification, and immunogenicity, making them attractive candidates for drug delivery systems (22,23). In the literature, studies published in the last 5 years have shown that aptamers can effectively target cancer cells and complement antibodies in therapeutic contexts by modulating gene (24–27).

Furthermore, nucleic acids, including small interfering RNAs (siRNAs) and messenger RNAs (mRNAs), are also used as ligands. Although these molecules have the disadvantage of being rapidly degradable in the body environment, these disadvantages can be overcome by using nanocarrier systems such as liposomes and polymeric nanoparticles (28,29). The development of smart nanocarriers that can respond to specific stimuli in the tumor microenvironment has further increased the efficacy of nucleic acid-based therapies(30,31).

Peptides are biologically active molecules, typically less than 50 amino acids in length, with unique properties. Due to their biocompatibility, small size, high selectivity, and self-assembly properties, they are highly advantageous ligands for drug delivery systems.Moreover, peptides are capable of binding to and penetrating different barriers found in cells and tissues due to their physical, chemical and biological properties, therefore these functional peptides can be used to enhance drug delivery systems via conjugated on NPs surface. For instance, a well-known peptide such as RGD (arginine-glycine-aspartic acid) has been shown to enhance drug accumulation in tumor tissues by targeting integrins overexpressed in the tumor vasculature (32). Similarly, transferrin receptor-binding peptides have been demonstrated to enhance the permeation of drugs across the blood-brain barrier, thereby facilitating their entry into the central nervous system (33).

2.2 Nanoparticles

Historically, the first use of nanotechnology dates back to the Ancient Egyptians. However, nanomaterials were not used or understood scientifically until the late 1900s (7). In December 1959, the famous Nobel laureate physicist Feynmandescribed nanotechnology to the world with the concept of "a billion tiny factories" in his famous lecture “There’s Plenty of Room at the Bottom” (34). Nanotechnology identified as to design and use of materials at the nano-scale which offers numerous advantages in several scientific fields (35,36). In this regard, nanoparticles (NPs) are considered the key components of nanotechnology.

Nanoparticles are materials ranging in size from 1 to 1000 nanometers (nm) which have unique dimensional properties that distinguish them from other materials (37,38). Regarding their shape, NPs can be of 0D, 1D, 2D, or 3D structure types (Fig. 2.3). They can be categorized into different categories depending on their source/material type, such as metal, carbon, lipid, or polymeric-based nanoparticles (14). NPs have been of great interest due to their small size and high surface-to-volume

ratio, alongside their physical, biological, surface, and chemical properties and reactivity (Fig. 2.4) (39). Owing to these properties, they find applications in a variety of different fields such as healthcare, pharmaceuticals, biomimetics, materials, electronics, robotics and many others (40).

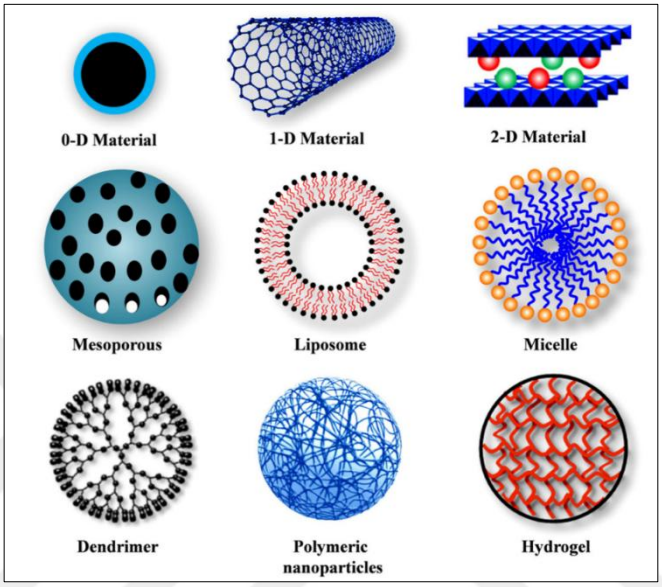

Figure 2.3. Different types of nanocarriers depending on their dimension (41).

Nanoparticles employed as drug carriers have a vital role to play in overcoming the problems associated with conventional drug and drug delivery systems while improving the treatment efficacy of drugs, protecting drugs from the challenging environment of the body, offering multiple agents together for combination therapy and diagnostics, and thus providing a promising approach to all kinds of drug delivery systems due to the nanomaterials' certain properties such as their shape, biocompatibility, biodegradability, and high surface area-to-volume ratio (42–44).

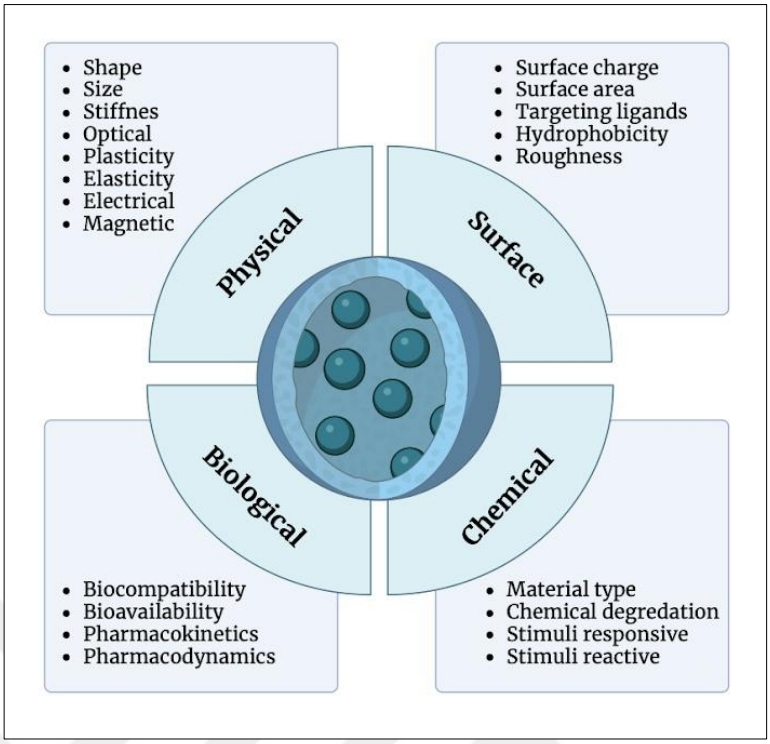

Figure 2.4. Biological, chemical, physical and surface properties of NPs (created with Biorender.com).

Various methodologies focusing on different material types and techniques have been used to optimize the drug loading efficiency, stability, and release profiles of nanoparticles prepared for drug delivery systems (45). The design and preparation of drug-loaded NPs can significantly influence the method of interaction between the drug and the nanoparticle matrix. Several strategies are available for drug incorporation, including adsorbing, trapping, dispersing, attaching, and encapsulation, and each one is adapted to optimize drug delivery based on the intended application (46).

Dispersion and encapsulation are common methods for loading drugs into nanoparticles, particularly in polymeric systems (47). In the literature, Zhao et al. Developed folic acid-conjugated pH-responsive polymeric nanoparticles that encapsulated doxorubicin (DOX) and a near-infrared (NIR) dye for combined photothermal-chemotherapy treatment (48). Their study demonstrating the potential of

encapsulation strategies to enhance therapeutic efficacy. Similarly, the use of hydrophobic interactions to encapsulate drugs within polymeric matrices has been reported, where DOX was successfully loaded into nanorods formed from polycaprolactone (PCL), resulting in improved cellular uptake compared to free DOX (49).

Trapping and adsorption are other feasible methods for loading drug molecules to nanoparticles, particularly for the specific release profiles. In 2018, Tan et al. designed a photosensitive hyperbranched polymer (HBP) that conjugates DOX within hydrophobic cavities and enables controlled drug release upon UV irradiation (50). This study also demonstrates the versatility of attachment methods in modifying the release kinetics of therapeutic agents.

2.3 Polymeric Nanoparticles

Polymeric nanoparticles (PNPs) have attracted considerable attention in recent years for their potential in drug delivery systems, owing to their unique physicochemical properties, such as tunable size (1-1000 nm), shape, surface charge, and functionality, which enable them to cross various biological barriers and ensure precise delivery of therapeutic agents to targeted sites in the body, and enhances the therapeutic efficacy of drugs and minimizes potential side effects (10,51–53).

The versatility of polymers allows the design of nanoparticles that can encapsulate a wide range of both synthetic and natural agents, including proteins, peptides, drugs and small molecules (54). Depending on the preparation method, the drug may be dissolved, entrapped, encapsulated, or attached to the nanoparticle matrix, forming various types of polymeric nanoparticles, such as nanospheres or nanocapsules (Fig. 2.5) (55).

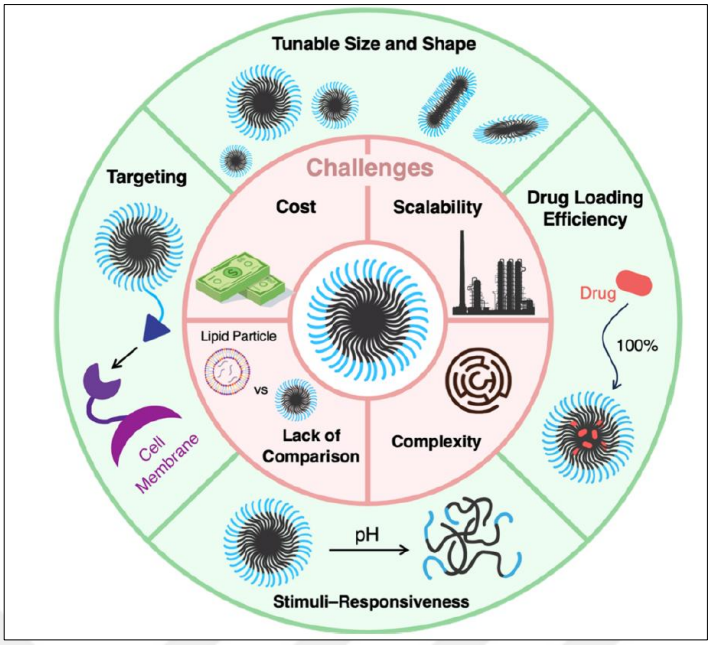

Figure 2.5. Overview of advantages and challenges of the PNPs (56).

The choice of polymeric materials for nanoparticle formulation significantly impacts their performance. Both synthetic and natural polymers, such as poly(lactic-co-glycolic acid) (PLGA), poly(lactide) (PLA), poly(ε-caprolactone) (ε-PCL), chitosan or collagen used in the formation of PNPs due to their favorable degradation profiles and low toxicity (56). In addition to these natural and synthetic polymers, functionalized polymers are increasingly utilized to optimize the performance of PNPs. Amphiphilic block copolymers, for example, facilitate the formation of micelles capable of encapsulating hydrophobic drugs, thereby improving their solubility and stability in aqueous environments (57).

Among the various materials used for PNP formulations, biodegradable polymers stand out from traditional non-biodegradable materials, making them ideal candidates for biomedical applications. Polymers such as PLGA, PCL and chitosan have garnered significant attention for their ability to degrade into non-toxic byproducts that are readily metabolized or excreted, thereby minimizing adverse effects (58,59). For instance, PLGA hydrolyzes into lactic and glycolic acids, metabolites naturally processed by the human body (59). Chitosan is a well-known natural polymer for its

low toxicity and biocompatibility, making it particularly suitable for various biomedical applications (60). The degradation rate of biodegradable polymers can be tuned to specific therapeutic needs, facilitating the formation of sustained drug delivery systems. For example, PLGA nanoparticles can be designed to deliver drugs in a controlled and prolonged manner, minimizing the need for frequent dosing (61,62). Similarly, chitosan nanoparticles exhibit adjustable release profiles, which can be further optimized through various formulation strategies (63,64). Additionally, the ability of these polymers to encapsulate both hydrophilic and hydrophobic therapeutic agents broadens their applicability across diverse drug classes (62,64).

2.3.1 Chitosan Nanoparticles

Chitosan, is a naturally occuring polysaccharide, a bioplymer made from deacetylation of chitin. The chemistry of Chitosan is characterized by its unique structure, β-1,4-linked 2-amino-2-deoxy-β-d-glucose (deacetylated d-glucosamine) and N-acetyl-d-glucosamine units (Fig. 2.6). The degree of deacetylation determines the functional properties and the solubility (65). Due to the protonation of the amine groups ($-NH_2$) on Chitosan, it is soluble in acidic conditions, and this solubility allows the formation of nanoparticles through different methods which makes it attractive for different applications (66). It is a well known bioactive compound possessing many biological properties, including antifungal, antimicrobial, antioxidant, and wound-healing activities. In addition to these properties, unique characteristics such as non-toxicity, biodegradability, biocompatibility, non-antigenicity, and low cost have led to its use in broad applications in drug delivery systems, tissue engineering, and many other fields (67,68).

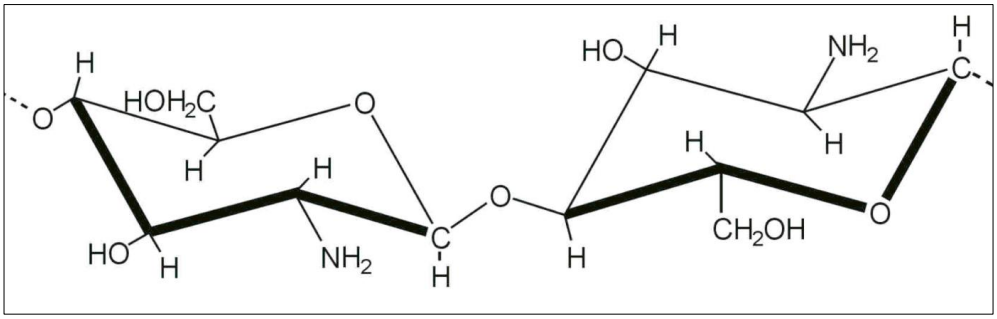

Figure 2.6. Chemical structure of the Chitosan.

Different therapeutic agents can be encapsulated with ChNPs, and their properties can be tailored using various synthesis methods such as ionic gelation, solvent evaporation, emulsificatin solvent diffusion, spray drying, etc. The ionic gelation method allows the formation of nanoparticles through electrostatic interactions between chitosan and anionic crosslinking agents such as sodium tripolyphosphate (TPP) (69). The number of amine groups (the degree of deacetylation) of chitosan and the concentration of TPP significantly influence the size and stability of the nanoparticles. For instance, increasing the concentration of TPP typically results in smaller nanoparticles due to enhanced crosslinking, which can improve the encapsulation efficiency of hydrophilic drugs (70). Additionally, the molecular weight of chitosan affects the release profile of the encapsulated drugs; lower molecular weight chitosan tends to produce nanoparticles with faster degradation rates and quicker drug release, while higher molecular weight chitosan results in slower degradation and prolonged release (71). Moreover, surface modifications of chitosan nanoparticles can enhance their biocompatibility and targeting capabilities, making them suitable for various biomedical applications.

2.4 Functionalızation Methods

2.4.1 Surface Modification Strategies

Nanoparticle modification can be carried out via chemical methods such as covalent conjugation, electrostatic interactions, and surface adsorption. Peptides and antibodies increase the stability, biodistribution, and efficiency of targeting of the cells. In this context, PEGylation is often used to impact circulation time and avoid nonspecific binding with various proteins (72). Avoiding nonspecific binding and increased circulation time provides increased drug delivery efficiency.

As known in the literature, the T7 peptide is commonly studied since it helps BBB penetration of the NPs (73). Combining PEG linkers and the T7 peptide reduces the steric hindrance; therefore, binding affinity to the receptors increases. In addition to this effect, the stability increases due to reduced aggregation and enhanced circulation (74).

Dual modification of peptides with antibodies such as anti-CD11b via conjugating the amide bond formation between C=O functionalized NPs and antibody's amine groups (75). The anti-CD11b is a crucial marker for targeting the activated microglia with high selectivity. The main benefit of using anti-CD11b is achieving site-specific drug delivery by using the integrin expression of the microglia and macrophages (76).

In summary, the modification helps molecules to pass through the BBB and aids in the selective targeting of neuroinflammation. Dual modifications of peptides and antibodies increase the specific and compelling drug delivery while binding the activated microglia and lowering the energy of BBB crossing, respectively.

2.4.2 Conjugation via Cleavable Bonds

As the upcoming chapters will show the data on modifications using chitosan nanoparticles, this section will explain the idea behind the methodology used in the thesis. Chitosan functionalization with anti-CD11b antibodies and PEGylated T7 peptides should be carried out with careful steps to achieve stability and targeting efficiency. Increasing the efficiency, therefore, will help for the controlled release of the drug into BBB (77). The cleavable linkers are mainly used to control the detachment of the ligands and responses toward the biological stimulants. Ligands are covalently bonded to the nanoparticle, and conjugation establishes easy attachment and removes the possibility of the drug's early release (78). The conjugation methods consist of various chemical processes, but the main two are PEGylation using maleimide-thiols and EDC/NHS chemistry (79,80). EDC/NHS was the chosen method in the experiments since it is less time-consuming and cost-efficient. The chemistry of EDC/NHS conjugation is based on carboxy and amine groups supplying irreversible attachment and stability and sustaining the functionality of the antibody.

The integration of conjugation linkers supplies controlled degradation of the molcules, controls the response towards stimulation and releasing of the ligands when the NPs reach the target site. PEGylated NPs have disulfide linkages which are sensitive to intracellular environments. The cells contains higher concentration of the glutathione which gives a reduction reaction with disulfide bonds. These reactions help releasing the peptides and increases the transport towards the BBB.

2.5 Neuroinflammation

Neuroinflammation represents a critical mechanism involved in the pathology of various neurodegenerative diseases, including Alzheimer's disease (AD) and Parkinson's disease (PD), amyotrophic lateral sclerosis (ALS), and multiple sclerosis (MS). Multiple neuroimaging studies have established the association of

neuroinflammation with cognitive dysfunction (81). For instance, Leng et al. highlight that neuroinflammation, particularly microglia activation, correlates with cognitive decline in patients with AD, with neuroimaging findings linked to lower cognition and faster cognitive decline (82). This evidence suggests that neuroinflammatory processes may precede or exacerbate neurodegenerative changes. Further emphasizing the connection between neuroinflammation and Alzheimer's pathology, research indicates that neuroinflammation continues to be an independent driver of disease progression even when considering amyloid and tau pathologies (83).

Pro-inflammatory cytokines, such as IL-6 and IL-8, align with the hypothesis that inflammation contributes to cognitive impairments and is a target for therapeutic interventions (84). These inflammatory responses are part of the neurodegenerative disease process and interact with other pathological mechanisms, including oxidative stress and mitochondrial dysfunction (85).

The intersection of neuroinflammation and traumatic brain injuries (TBI) further complicates its role in brain pathology. Following a TBI, the brain undergoes a complex inflammatory cascade involving microglial activation and increased release of inflammatory mediators, exacerbating the initial injury and leading to secondary brain damage (86,87). Studies have shown that neuroinflammation post-TBI can persist for years, playing a crucial role in long-term neurological outcomes and contributing to conditions such as Alzheimer's disease and other neurodegenerative disorders (88,89). In particular, the prolonged activation of microglia and astrocytes following TBI has promoted a chronic neuroinflammation state directly associated with cognitive deficits (87,90). Strokes, particularly ischemic strokes, are fundamentally linked to neuroinflammatory processes that significantly impact recovery outcomes. In the initial phase of a stroke, neuroinflammation is observed, resulting in BBB dysfunction, increased oxidative stress, and the activation of inflammatory cells that can propagate further neuronal damage (91,92). The interplay between peripheral immune responses and central nervous system inflammation highlights a significant aspect of neuroinflammation's role in ischemic events (93). Moreover, neuroinflammation in stroke not only contributes to immediate damage but

also alters the course of recovery by influencing neurogenesis and repair mechanisms (91,94).

The cellular players in neuroinflammation, primarily microglia, and astrocytes, have been found to exhibit aberrant activation patterns in various stages of neurodegeneration. Researchers have elucidated the RGS5-TNFR axis in astrocytes as a significant contributor to chronic neuroinflammation in conditions like PD (95). This coordinated response highlights the neuroinflammatory component as not merely reactive but as a potentially orchestrated mechanism promoting neurodegeneration, where activated glial cells release inflammatory mediators that exacerbate neuronal damage (96).

The dynamic interplay between neuroinflammation and BBB disruption is a critical factor in the progression of various neurological disorders. A comprehensive understanding of this relationship is essential for developing therapeutic strategies aimed at reducing neuroinflammation, thereby maintaining BBB integrity and facilitating recovery following acute neurological injuries such as strokes or traumatic brain injuries. Investigating the mechanistic pathways linking these processes has significant potential for advancing neuroprotective interventions. To fully understand the complexity of targeting neuroinflammation, it is first necessary to study the structure and function of the BBB and the challenges it presents for effective drug delivery.

2.5.1 Blood Brain Barrier (BBB)

The central nervous system (CNS), consisting of the brain and spinal cord, is responsible for processing sensory information perceived by peripheral nerves and coordinating appropriate responses. Given their critical role in maintaining homeostasis as the primary control centers of the body, the brain and spinal cord are protected by numerous protective structures, including bones, meninges, the choroid

plexus epithelium (blood-cerebrospinal fluid barrier), the avascular arachnoid epithelium (cerebrospinal fluid–blood barrier) and the blood-brain barrier (31,32).

The Blood-Brain Barrier (BBB) is a complex structural, functional, and physiological barrier regulating the exchange of ions, nutrients, and cells between the bloodstream and the brain. Structurally, it comprises cerebral endothelial cells, pericytes, astrocytes, and a basement membrane. The BBB forms the "neurovascular unit" with neurons and glial cells (Fig. 2.7) (97–99). In this manner, the BBB provides the brain with the necessary nutrients, glucose, and oxygen to maintain normal neural functioning. At the same time, the BBB acts as a shield against neurotoxic substances and thus creates the neural microenvironment that is crucial for healthy brain function (99). Thus, the presence of the BBB prevents damage to the brain. But it also limits the drugs that enter the CNS to treat brain diseases such as such as Alzheimer'sdisease (AD), Parkinson's disease (PD), amyotrophic lateral sclerosis (ALS), multiple sclerosis (MS), and several types of brain cancers.

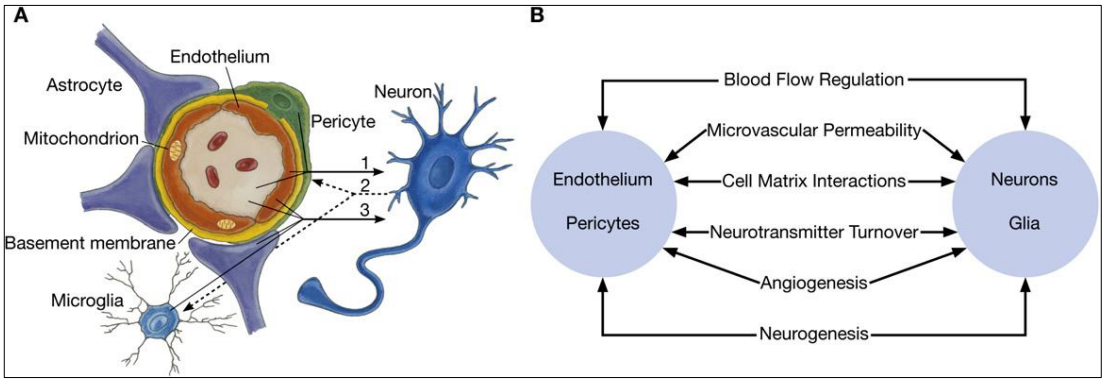

Figure 2.7. Schematic representation of the neurovascular unit comprising endothelial cells, pericytes, astrocytes, and microglia, regulates brain function and forms the structural basis of the blood-brain barrier (100).

The blood-brain barrier (BBB) severely limits drug delivery, blocking over 98% of small-molecule drugs and nearly all large-molecule drugs. Only small, lipophilic molecules (<400 Da) can diffuse across the BBB, while transporting larger,

hydrophilic, or lipid-insoluble molecules is highly restricted (101). Additionally, viruses such as HIV use infected immune cells as a “Trojan horse” to penetrate the BBB and access to the brain (102). However, BBB permeability is influenced by size and weight, protein-to-protein interactions, lipophilicity and factors such as a molecule's affinity for specific transport systems. In pathological conditions such as neuroinflammation, traumatic brain injury, and cancer, disruption of the structural integrity and functionality of the BBB can also lead to an alteration of permeability. The BBB limits the entry of substances to the CNS through its tight junctions, efflux transporters, pericytes, and astrocytes. However, different access routes to the CNS through the BBB can be listed as follows: paracellular diffusion, transcellular diffusion, carrier-mediated diffusion, receptor-mediated transport, adsorptive-mediated transport, and cell-mediated transport (Fig. 2.8).

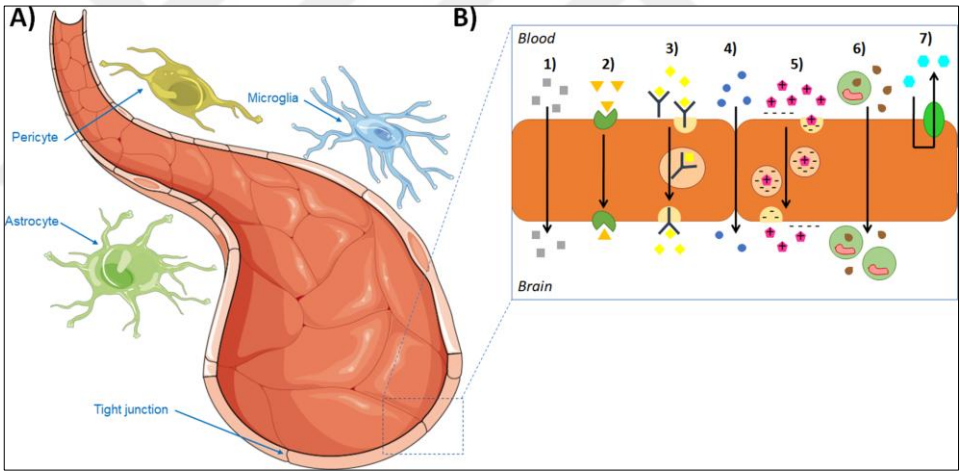

Figure 2.8. The BBB structure and the different transport mechanisms. (A) The structure of the BBB, (B) Different transport mechanism to the CNS through the BBB (103).

2.5.2 BBB Penetrating Peptides

Due to its highly selective permeability, the BBB is a significant obstacle in developing therapies for CNS disorders. In order to address this, researchers have investigated the potential of blood-brain barrier penetrating peptides (BBPPs) for drug

delivery. The BBPPs have emerged as promising tools to transport therapeutic agents across the BBB. These peptides typically exhibit a net positive charge and specific amino acid sequences that interact with negatively charged cell membranes, enabling BBB penetration.

Cadherin-derived peptides such as HAV6 have demonstrated the ability to transiently modulate BBB permeability, allowing targeted delivery of therapeutic agents to the brain (104,105).

Likewise, cyclic peptides such as ADT and cHAVc3 are able to facilitate the delivery of small molecules while maintaining BBB openings for prolonged periods (106,107). These findings underline the potential of cadherins and cyclic peptides as effective agents for BBB modulation. Cell-penetrating peptides (CPPs) represent another class of compounds that can effectively cross the BBB. Arginine-rich CPPs, including PVEC and Tat, have superior BBB efflux properties over other peptides (108,109). It has been suggested that integrating active targeting ligands with CPPs further enhances the delivery efficiency of therapeutic peptides across the BBB (77).

The T7 peptide with HAIYPRH sequence has attracted attention for its ability to increase BBB permeability. T7 peptide-modified low-density lipoprotein particles have significantly improved glioma therapy by facilitating targeted delivery of vincristine across the BBB (73,110). Furthermore, the T7 peptide has been shown to inhibit angiogenesis, a critical process in tumor growth and metastasis, positioning it as a promising candidate for glioma therapy (111). Likewise, integrating T7 peptide into nanoparticle formulations has been explored to enhance therapeutic efficacy. Zong et al. utilized T7 in dual-ligand doxorubicin liposomes, which improved targeting and therapeutic efficacy against glioma in animal models (112). This approach underscores the potential of T7-modified delivery systems in enhancing the bioavailability of chemotherapeutic agents in the CNS.

The development of predictive tools for BBB-penetrating peptides, such as B3Pred and BrainPepPass, has facilitated the identification of promising candidates for further experimental validation (108,113). These computational approaches may facilitate the design of novel peptides for improved drug delivery across the BBB.

In addition to the peptides discussed above, other BBB-penetrating peptides have also been investigated. Angiopep-2, for example, has been used to functionalize transporters and deliver various therapeutic agents, including anticancer drugs, to the brain, as it can target the low-density lipoprotein receptor-related protein overexpressed in cancer cells (114).

Furthermore, penetration-derived cell-penetrating peptides, in combination with targeting ligands such as the NGR peptide, have been used to enhance the delivery of therapeutic payloads to the brain (115). Using dual peptide-functionalized nanoparticles has also attracted attention as a strategy to improve targeted drug delivery to the brain. By combining cell-targeting peptides such as cRGD and GE11 with BBB-penetrating peptides, researchers have increased the selectivity and transport of therapeutic agents across the BBB (116,117).

3. MATERIALS AND METHODS

3.1 Materials

α-Lipoic Acid (Sigma Aldrich, US), Chitosan (Sigma Aldrich, catalog number 448869, 448877), anhydrous dimethyl sulfoxide (DMSO, Sigma Aldrich, US), anhydrous dichloromethane (DCM, Sigma Aldrich, US), EDC (N-(3-Dimethylaminopropyl)-N′-ethylcarbodiimide hydrochloride), N-Hydroxy Succinimide (NHS, Sigma Aldrich, USA), Concanavalin A. Alexa Fluor 488 (Thermo Fisher, USA), anti-CD11b antibody ((M1/70), eBioscience™), Cy3-NHS ester (BP-22535, BroadPharm, USA),Amicon® UltraCentrifugal Filter Unit (Mwt cut-off: 100 kDa), Acetonitrile (ISOLAB Chemicals), GLPbio cell counting kit-8, Peptide Synthesizer (CEM, Liberty™ Blue and CEMDiscover™Razor Microwave) DLS, LC/MS-MS (6420 Triple Quad LC/MS, Agilent Technologies), HPLC (260 Infinity Quaternary LC systems, Agilent Technologies),^{1}H NMR, ZetaSizer (Malvern Zetasizer Nano ZS), Scanning Electron Microscopy (Thermo Fischer Scientific, Quattro ESEM), Transmissive Electron Microscopy (Thermo Fischer Scientific, Talos L120C), Lyophilizer (HyperCOOL 8080) Varioskan (Thermo Scientific Varioskan Flash), microplate reader (Biotek Microplate Reader), EVOS Imaging System (Invitrogen™ EVOS™ M5000 Imaging System), FT-IR Spectroscopy (Thermo Scientific NICOLET iS10 instrument), NanoDrop (Thermo Scientific™ NanoDrop™ One Microvolume UV-Vis Spectrophotometer).

3.2 Nanoparticle Preparation and Characterization

3.2.1 Preparation and Characterization of Chitosan Nanoparticles (Ch-NPs)

A variety of different types of nanoparticles were prepared to find the optimal nanoparticle formulation for this project. Polymer solutions were prepared by dissolving different molecular weight of the chitosan polymer (Low mwt: 50-190 kDa,

and medium mwt: 200-310 kDa) in low concentration acetic acid (0,1 M, pH: 5). Different concentrations of these polymer solution then subjected to a ionic gelation reaction by addingsodium tripolyphosphate (STPP), a negatively charged cross-linker solution in phosphate saline buffer (10 mM, pH: 7.4) at a [C]:[T] ratio of 1:1 and 1:0.5 for 15 min, 30 min, 60 min, and 120 min on a magnetic stirrer (1300 rpm) at room temprature (RT). After then, prepared nanoparticle solutions filtered using different types of syringe filters (Nylon, PES (Polyethersulfone), and RC (Regenerated Cellulose) filters) to eliminate unbound STPP molecules, buffer solution salts, and possible polymeric aggregates.

The most ideal Ch-NP was prepared as follows: 4 mg of chitosan (50-190 kDa) was dissolved in 4 mL acetic acid (0.1 M, pH: 5) for 1h at 1300 rpm, RT to obtain 0.1% w/v. Then, 4 mL STPP (0.01% w/v) was added dropwiseonto the polymer solution ([C]:[T] = 1:1) and left on the magnetic stirrer for 1h at 1300 rpm, RT. After one hour of reaction, the obtained nanoparticles were filtered twice; first with 0,45 µm Nylon and then with 0,22 µm PES filters, respectively. The purified Ch-NP solution stored at -20°C.

3.1.1.1 Stability Test of Chitosan Nanoparticles (Ch-NPs)

The prepared Ch-NPs at suitable size were diluted by 1:2 with the total volume in both pH 7.4 10 mM PBS buffer (as a model of healthy tissues) and pH 5.5 acetate buffer (as a model of inflammation in the tissues) and incubated at 37˚C (body temperature) by shaking at 200 rpm on an orbital shaker for 2 weeks. During incubation, the hydrodynamic diameter of the NPs was measured by DLS at certain time (0h, 0.5h, 1h, 2h, 4h, 6h, 8h, 10h, 12h, 24h, 48h, 42h, 120h, 168h, and every other day for 2 weeks) intervals.

3.2.2 Drug Loaded Polymer and Nanoparticle Preparation (LA-Ch-NPs)

3.2.2.1 Lipoic Acid Conjugated Chitosan Polymer Synthesis

In order to synthesize the drug-conjugated polymer, the primary hydroxyl groups in the chemical structure of chitosan were used. The anti-oxidant drug molecule (α-Lipoic Acid) was conjugated to chitosan with the carboxylic acid functional group (-COOH) in its chemical structure. Following this esterification reaction, the drug molecules were attached to the side branches of chitosan through hydrolyzable ester bonds, which are sensitive to the pH of the environment and can be broken by hydrolysis (118).

The synthesis of the drug-conjugated polymer involves 4 main steps. The first step is the protection of free amine ($-NH_2$) groups on the side branches of chitosan polymer with phthalic anhydride. For this step, 1 g of chitosan polymer and 2,76 g (18,6 mmol) of phthalic anhydride were weighted in a reaction vessel and then dissolved in 5% w/w DMF mixture (1 mL dH_2O and 19 mL DMF) and stirred at 100 ˚C for 8h. Subsequently, this mixture was cooled down to RT and poured into 50 mL of cold double distilled water to soldify and precipitate the polymer. The collected solid material was washed with pure methanol for 1h RT, then filtered and dried overnight in a desiccator. The product (Ph-CH), light yellow, 3,15 g was obtained.

Meanwhile, as the second step, the carboxylic acid group in the structure of the lipoic acid molecule was activated with thionyl chloride ($SOCl_2$). Therefore, 2 g of α-LA was dissolved in 20 mL of toluene and 1,41 mL of $SOCl_2$ (19,39 mmol) was added, and the mixture was refluxed in a condenser by heating and stirring at a temperature around the boiling temperature of toluene (between 60-80˚C) for 6h (119). This mixture was then cooled down to the RT and purged with nitrogen gas to eliminate any remaining molecules such as SO_2 and $SOCl_2$ from the environment in gaseous form

(degassing). The obtained product was then evaporated with toluene by using a rotary evaporator to give 2,81 g powder.

A basic environment was created in the third step for these two substances to couple and for the primary hydroxyl groups of chitosan to attack the chlorinated acyl group of α-LA and bind it with an ester bond. 500 mg of chitosan polymer with amines protected by a phthalic group (Ph-Ch) was soaked in 20 mL of pyridine the night before. Following day, 250 mg of the chlorinated lipoic acid molecule (LA-Cl) was dissolved in 5 mL of Toluene and added to this basic polymer medium. This mixture was then rotated for 2h at RT and then refluxed and heated at 60-80 ˚C, overnight. Accordingly, it is aimed that the hydroxyl groups in the Ph-Ch attack the LA-Cl molecule and the -Cl group is released as HCl and an ester bond is formed between them.The next day, prepared mixture was cooled down to RT, transferred to 50 mL of pure methanol and precipitated. Afterwards, this solid material was washed 2 times with methanol and dried in a desiccator for 2 days, and LA-Ph-Ch polymer was obtained as 680 mg in a slightly yellow form.

The final step is the removal of the phthalic groups and reconstituting the drug-conjugated polymer to attain its free amine groups. This reaction was carried out with a basic hydrazine monohydrate solution. 500 mg of LA-Ph-Ch polymer was mixed with 466 mg of hydrazine monohydrate solution dissolved in 11,6 mL DMF at 4% w/v, and stirred at 100 for 1h placed under nitrogen gas while heating. After this deprotection step, the mixture was again cooled down to RT and purified by using an RC dialysis membrane (Mwt cut-off: 10 kDa). The purified solution was freeze-dried in a lyophilizer to obtain 340 mg of the product. This final product is the chitosan polymer (LA-Ch), in which the amine groups remain free on the side branches and are linked to the hydroxyl groups of the lipoic acid drug molecules by ester bonds. The final product LA-Ch polymer was analysed using both FT-IR and proton nuclear magnetic resonance (^{1}H NMR) to determine the chemical structure.

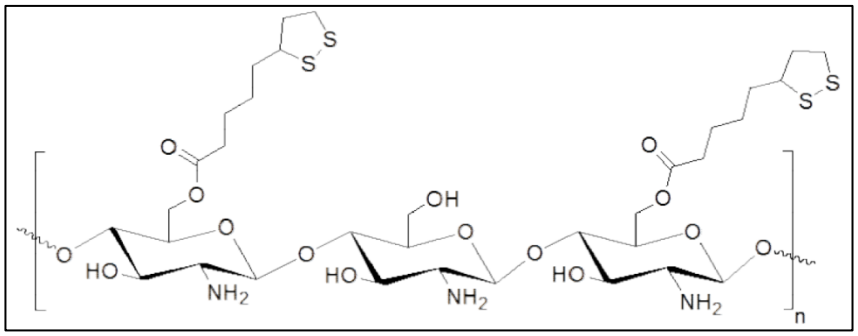

Figure 3.1. The chemical structure of α-Lipoic Acid conjugated chitosan polymer.

3.2.2.2 Preparation of LA-Ch-NPs

In the literature, it is stated that lipoic acid molecules can be physically encapsulated into the chitosan structure at a rate of approximately 45%, but 70% of the encapsulated drug is released into the environment within 30 minutes (120). Alternatively, the release of lipoic acid molecules covalently bound to the side branches of chitosan by amide bonds that remain stable in a physiological environment was observed to be a maximum of 10% (121). Accordingly, the quantity of the drug encapsulated in the nanoparticles was calculated to be 1.5-2 times higher than the value stated in the literature, with a final concentration of 15-20%. This approach was employed to enhance the efficacy of the drug by increasing the concentration delivered inside the cell while simultaneously slowing down the release of the drug.

For the preparation of the drug-loaded nanoparticles,the optimized procedure for the Ch-NPs was used.In this regard, the drug-loaded chitosan polymer (LA-Ch) was dissolved in 0.01M acetic acid solution at 0.1 wt% (w/v) and 0.01% STPP (w/v) was added at 1:1 by volume. This solution was stirred at 1300 rpm on a magnetic stirrer at RT, overnight. After that, the obtained nanoparticles were filtered twice; first with 0,45 µm Nylon and then with 0,22 µm PES filters, respectively. Subsequently, obtained drug-loaded nanoparticles (LA-Ch-NPs) ultrafiltered 5 times against ultra distilled water (ddH_2O) using an Amicon ultracentrifuge filter (Mw cut-off: 100 kDa) to remove unbound polymeric aggregates, and was sonicated for two minutes, respectively.

3.2.2.3 Determination of Drug Release Profiles from Drug-Loaded Nanoparticles

In order to determine the time-dependent drug release profile of LA-Ch-NPs, the nanoparticles were incubated in four different media: 10 mM phosphate-buffered saline (PBS) solution at pH 7.4, which mimics the physiological environment of healthy tissue and 0,1 mM acetate buffer solution at pH 5.5, which mimics the acidic inflammatory environment of tissue. In addition to these media, PBS and AB solutions with the esterase enzyme extracted from porcine liver were used.

Each 1 mL of LA-Ch-NP was placed on dialysis membranes (Mwt cut-off: 1kDa). Then, 40 mL of buffer solution was added, and incubation was started. These dialysis systems were incubated at 37 °C and 120 rpm on an orbital shaker, and 100 µL of samples from different media were taken at different time intervals (0-15-30-45 minutes, 1-2-3-4-6-8-10-12 hours, 1-2-3-4-5-6-8-10-15-20-25-30 days) and stored at -20 °C. After collection, the samples were analyzed using LC-MS/MS.

In the next step, the drug release profiles of the drug-loaded nanoparticles were analyzed both in human serum solution (10, 20, and 50 mg/mL concentrations separately) and 10 mM PBS (pH: 7.4) buffer solution containing esterase enzyme (at a ratio of 1 unit of enzyme: 1 µmol ester bond) using the dialysis method described above. These dialysis systems were incubated at 37 °C and 120 rpm on an orbital shaker. The free drug molecules released into the medium were analyzed by LC-MS/MS using the appropriate calibration curve and flow method.

3.2.3 Preparation of the Flourescent Dye Conjugated Nanoparticles (Cy3-Ch-NPs)

For the preparation of dye-conjugated nanoparticles, Cyanine-3 (ex550/em570, red) flourescent dye selected as imaging agent due to the free carboxylic acid group in its sturcture and by considering the excitation/emission wavelenghts of other dyes to be employed in in-vitro cell culture studies. The Cyanine-3 (Cy3) dye molecule was provided as Cy3-NHS ester (BP-22535, BroadPharm, USA), which has a NHS (N-Hydroxy succinamide) activated carboxylic acid group in its structure (Figure 3.2).

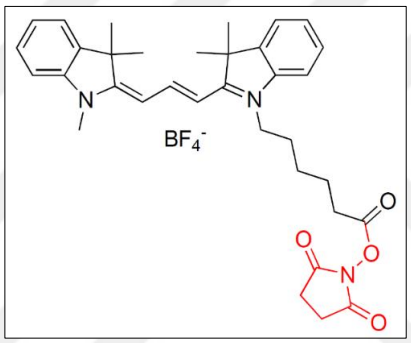

Figure 3.2. Chemical structure of Cy3-NHS ester dye molecule.

For the first step of this conjugation reaction, the ratio of free amine groups in Ch-NPs was calculated theoretically and subjected to 1:0.05 conjugation compared to dye molecule amines. For this purpose, 5 µl of triethyl amine (Et_3N) slowly dropped onto the previously prepared Ch-NPs and left on a magnetic stirrer at 1000 rpm, RT, to create a slightly basic environment. Meanwhile, 15 µg Cy3-NHS was prepared from the stock solution (0,1 mg/100µl) made by dissolving the solid Cy3-NHS dye in DMSO (99%, high purity) and diluted in 1 ml PBS (10 mM, pH 7.4). This dye solution was added to the activated Ch-NP solution at 1200 rpm, RT, in dark for 36h. After 36h, a pink dye-conjugated nanoparticles solution obtained and were then purified via centrifugation against ddH_2O with Amicon ultracentrifuge tubes (MW cut-off: 100 kDa) at 2500 rpm for 3 min and this process was repeated three times.

Additionally, Cy3 dye amount of the Ch-NPs was measured using NanoDrop (Thermo Scientific™ NanoDrop™ One Microvolume UV-Vis Spectrophotometer), and Varioskan (Thermo Scientific™ Varioskan Flash) devices. The details of the calibration curves created are given in the Appendices.

3.2.4 Preparation of Targeted Nanoparticles

3.2.4.1 Synthesis and Characterization of T7 Peptide

The T7 peptide chain (HAIYPRH) selected the target and cross the blood-brain barrier (BBB) by the nanoparticles was synthesized using Liberty Blue™ (CEM) Automated Microwave Solid Phase Peptide Synthesizer.

Solid phase peptide synthesis (SPSS) is a synthesis method that covalently links the newly formed peptide chain by sequencing amino acids to an insoluble polymeric support (resin) (Figure 3.3). At the same time, this method is an approach to reduce losses in the final product through simplified filtration and washing of the device of the reagents used for the synthesis. It is synthesized to extend from the C-terminal end of the peptides to the N-terminal end. Amino acids and resin have protective groups to prevent unwanted side reactions during synthesis. The first step of the synthesis cycle is to load the resin into the device. In this step, after removing the protecting group in the resin (deprotection step), the first amino acid dissolved in DMF is bound to the resin at the C terminus. The bound peptide is elongated by adding amino acids in cycles involving repeated deprotection and binding steps. When chain elongation is complete, the peptide is separated from the resin in its crude form, and simultaneously, the protective groups on the side chain are removed.

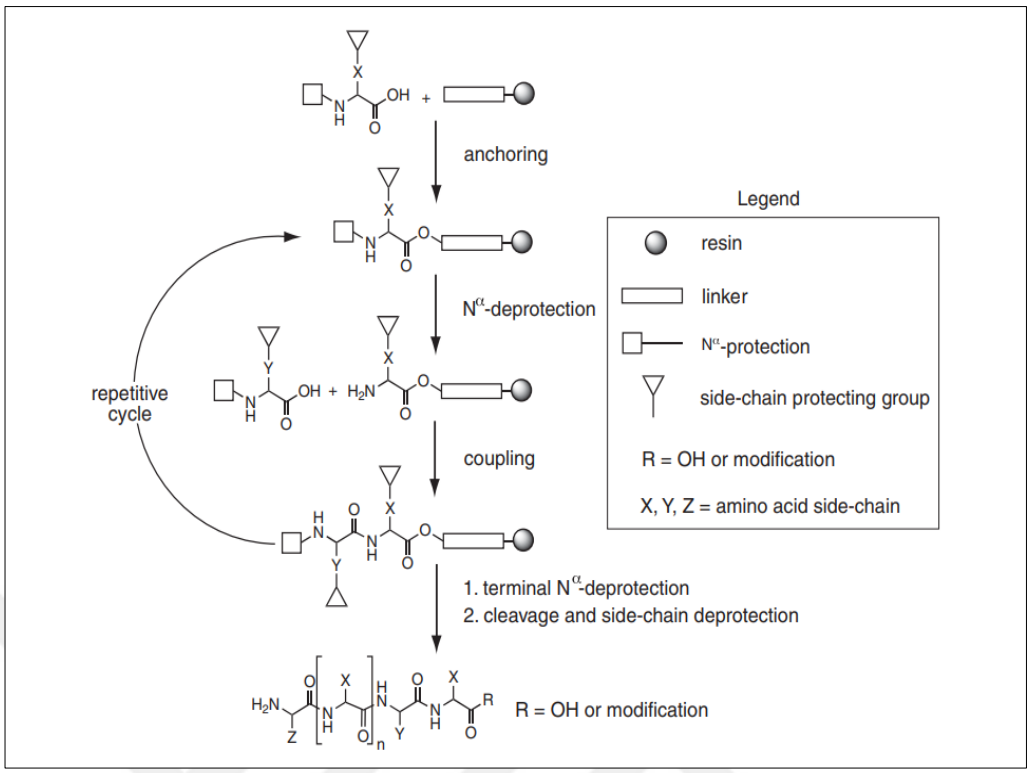

Figure 3.3. Solid phase peptide synthesis (SPSS) method and steps (122).

Amino acids and other materials used for the peptide synthesis reaction were prepared according to the ratios indicated in Table 3.1. For the synthesis, 0,19 g Alanine (Ala) in 3 mL DMF, 0,78 g Arginine (Arg) in 6 mL DMF, 0,75 g Histidine (His) in 6 mL DMF, 0,22 g Isoleucine (Ile) in 3 mL DMF, 0,21 g Proline (Pro) in 3 mL DMF and 0,28 g Tyrosine (Tyr) in 3 mL DMF were prepared and 0.143 g resin was swollen in 7,5 mL DMF, respectively.

Table 3.1. Amount of amino acids, deprotectors, activators, bases and resins used to synthesize T7 Peptide (HAIYPRH).

Materials	Volume in DMF (ml)	Mass (g)
Alanine (A)	3 mL	0,19 g
Arginine (R)	6 mL	0,78 g
Histidine (H)	6 mL	0,75 g

Isoleucine (I)	3 mL	0,22 g
Proline (P)	3 mL	0,21 g
Tyrosine (Y)	3 mL	0,28 g
Piperidine	40 mL	6,88 g
DIC	10 mL	0,631 g
Oxyma	5 mL	0,711 g
Resin	7,5 mL	0,143 g
DMF	224 mL	-

In the final step, the cleavage reaction was performed to remove the peptide from the resin For the cleavage reaction, the cleavage filter was washed 3 times with DCM and then placed in a cleavage cocktail prepared using 125 µL distilled water, 125 µL triisopropylsilane (TIS) and 4.75 mL trifluoroacetic acid (TFA) in the RazorTM Peptide Cleavage System (CEM) at 38 °C for 30 min (Table 3.2). Then the obtained peptide precipitated in 15 mL of cold diethyl ether (-20 °C) and centrifuged 2 times for 3 min at 5000 rpm. After centrifugation, the diethyl ether and cleavage cocktail were carefully removed from the precipitated peptide and the peptide was placed under vacuum in a desiccator overnight. The next day, the peptide was removed from the desiccator and placed in a lyophilizer (HyperCOOL 8080) overnight for better drying. The chemical characterization of the synthesized T7 peptide was completed using an LC/MS-MS (6420 Triple Quad LC/MS, Agilent Technologies), HPLC (260 Infinity Quaternary LC systems, Agilent Technologies), and ^{1}H-NMR.

Table 3.2. Amounts of material used for the cleavage cocktail prepared for the cleavage of T7 Peptide (HAIYPRH).

Materials	**Volume (µl)**
TFA	4,75 mL
TIS	125 µL

ddH_2O	125 µL

3.2.4.1.1 HPLC Analysis

HPLC analysis was performed for the purity control of synthesized peptide. 1 mg of T7 peptide was dissolved in 500 µL acetonitrile (ACN) and 500 µL ddH_2O and analyzed by HPLC (260 Infinity Quaternary LC system, Agilent Technologies) with C-18 column. Peaks were detected based on ultraviolet (UV) absorption at 214 nm and 254 wavelengths. In the analysis, ddH_2O containing 0,05% trifluoroacetic acid (TFA) as mobile phase A and acetonitrile (ACN) containing 0,025% TFA as mobile phase B were used with a flow rate of 2 mL/min.

3.2.4.1.2 LC/MS-MS Analysis

LC/MS-MS analysis was performed for the chemical characterization of the T7 peptide.In the analysis of 20 µL of the synthesized peptide, mass analysis was performed by considering the theoretical molecular weight and ionization degree of the peptide. The C18 stationary phase column was used by adding 0,05% (by volume) Formic Acid (FA) to the mobile phase mixture (50% ACN & 50% ddH2O) to ionize the peptide molecules. The analysis was performed using the MS2Scan mode for both negative and positive regions.

3.2.4.1.3 FT-IR Analysis

The functional group analysis of the T7 peptide were performed by Fourier transform infrared spectroscopy (FT-IR, Nicolet iS10 Thermo Fisher). Air was used as the background reference before analyzing the sample. The spectrum was measured from 400 to 4000 cm^{-1} with multiple scans at RT.

3.2.4.1.4 ^{1}H-NMR Analysis

The chemical structure of the T7 peptide was characterized using proton nuclear magnetic resonance (^{1}H NMR,) on a 400 MHz Bruker NMR spectrometer (Mercury-VX 400 BB) in deuterated DMSO (DMSO-d_6).

3.2.4.2 Synthesis of PEG Conjugated T7 Polymer

The first step of the synthesis of the T7-PEG conjugate is the protection of the thiol group of the heterofunctional PEG polymer (Mwt: 2000 gmol^{-1}), the starting material, with a free primary amine (-NH_2), using Aldrithiol (123). A total of 37,5 mg (0,01875 mmol) of Amino-PEG-Thiol polymer and 25,8 mg (0,02813 mmol) of Aldrithiol (1.5 times molar excess) were weighed in a 25 ml round-bottom flask. After purging with nitrogen gas, all solid materials in the reaction vessel were dissolved in 1 mL of pure methanol (MeOH) with sonication. The reaction was then carried out on a magnetic stirret at 1000 rpm, in the dark, at RT under a nitrogen balloon for 18h. Without opening the flask, the mixture was directly subjected to the second step of the total synthesis.

In the second step, the T7 peptide was conjugated to the other end of the obtained Amine-PEG-PDS polymer. For this purpose, the carboxylic acid group (-COOH) in the chemical structure of the T7 peptide was first activated with NHS by using EDCI/NHS chemistry where NHS molecules were bound to the -COOH group of the T7 peptide through its coupling agent, EDCI (124). 30 mg (0,00336 mmol) of T7 peptide, 12,9 mg (0.0672 mmol) of EDCI, and 7,7 mg (0,0672 mmol) of NHS were weighed at a 1:2:2 ratio into a 10 mL round bottom flask and dissolved in a 1 mL anhydrous DMF and the reaction was carried out on a magnetic stirrer at 1300 rpm, RT for 2h. After the reaction, NHS activated T7 peptide is obtained.

Afterward, this solution was added dropwise directly to the solution of the Amine-PEG-PDS synthesis reaction started the previous day, and nitrogen gas was passed through. This reaction was carried out overnight on a magnetic stirrer at 1300 rpm, RT, in the dark due to the PDS group at the end of the PEG chain. As a result of this reaction, the NHS-activated T7 peptide was bound to the amine end of the amine-PEG-PDS polymer, whose thiol end was protected by a PDS group, via an amidation reaction.

The following day, the solution was precipitated by adding it dropwise into 40 mL of cold diethyl ether, and the mixture was stored at -20 ˚C for 24 hours. The resulting precipitated T7-PEG-PDS conjugate was then collected by filtration using a sintered filter, and the solid product was dried under vacuum in a desiccator for one day.

Subsequently, to introduce a disulfide group to the other end of the conjugate, the filtered T7-PEG-PDS polymer (50 mg, 0,0149 mmol) was dissolved in 1 mL of MeOH, and 2.45 µL (0,02813 mmol) of 3-mercaptopropionic acid (3-MPA) was added. The reaction was carried out in the dark at RT for two nights, during which all PDS groups in the conjugate were replaced by 3-MPA through a disulfide exchange reaction. To prevent material loss, no purification was performed at this step, and the reaction solution was directly used for the subsequent product synthesis. At the same time, EDCI and NHS were added to the reaction medium to facilitate the formation of T7-PEG-ss-NHS, the final structure of the targeted conjugate. To this end, 5,4 mg (0,02813 mmol) EDCI and 3.2 mg (0,02813 mmol) NHS dissolved in 1 mL DMF were added, assuming that the 3-MPA attachment reaction was completed in 100% yield. Then, reaction was continued overnight at RT in the dark while stirring on a magnetic stirrer and the final conjugate was purified by precipitation in cold diethyl ether. The synthesis steps are summerized in Figure 3.4.

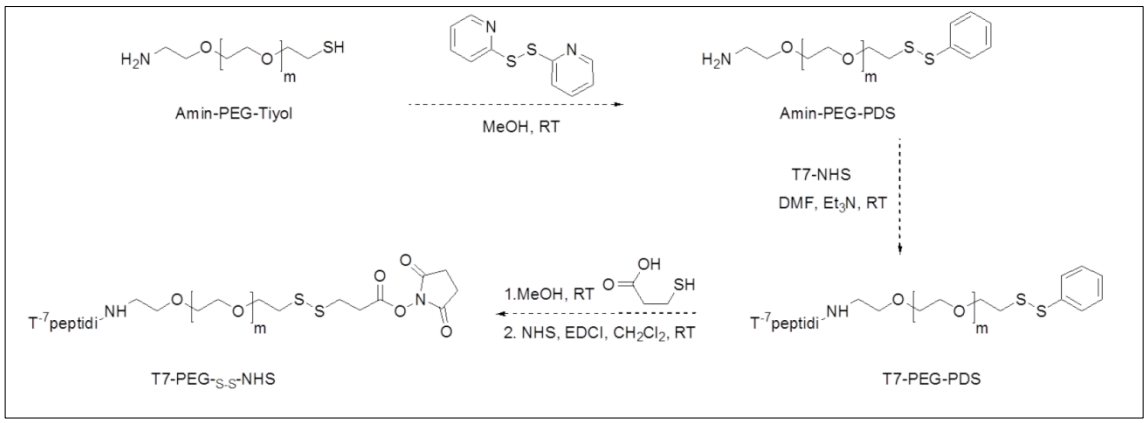

Figure 3.4. Synthesis steps of the T7-PEG-S-S-NHS functional polymer.

3.2.4.2.1 HPLC Analysis

HPLC analysis was performed for the purity control of the Amine-PEG-Thiol polymer and synthesized T7-PEG conjugate. 1 mg of each sample was dissolved in 500 µL acetonitrile (ACN) and 500 µL ddH2O and analyzed by HPLC (260 Infinity Quaternary LC system, Agilent Technologies) with C-18 column. Peaks were detected based on ultraviolet (UV) absorption at 214 nm and 254 wavelengths. In the analysis, ddH_2O containing 0,05% trifluoroacetic acid (TFA) as mobile phase A and acetonitrile (ACN) containing 0,025% TFA as mobile phase B were used with a flow rate of 2 mL/min.

3.2.4.2.2 FT-IR Analysis

The functional group analysis of the Amine-PEG-Thiol polymer and the T7-PEG conjugate were performed by Fourier transform infrared spectroscopy (FT-IR, Nicolet iS10 Thermo Fisher). Air was used as the background reference before analyzing the sample. The spectrum was measured from 400 cm^{-1} to 4000 cm^{-1} with multiple scans at RT.

3.2.4.2.3 ^{1}H-NMR Analysis

The chemical structure of the Amine-PEG-Thiol and T7-PEG conjugate was characterized using proton nuclear magnetic resonance (^{1}H NMR) on a 400 MHz Bruker NMR spectrometer (Bruker 400 mHz) in both deuterated DMSO and deuterated chloroform (DMSO-d_6 and CDCl$_3$, respectively).

3.2.4.3 Preparation of Flourescent Dye Labeled and Microglia Targeted Nanoparticles (Cy3-CD11b-Ch-NPs)

For the *in-vitro* cellular uptake studies, the dye-conjugated nanoparticles (Cy3-Ch-NPs) obtained in Section 3.2.3 were conjugated with Anti-CD11b antibody, which can bind selectively with high affinity to the CD11b receptors synthesized on the cell surface of the active microglias in the inflammation site, used as a targeting group in order to specifially target microgia cells.

The first step was to activate the antibody using EDCI/NHS chemistry. For this, 25 mL of PBS (10 mM, pH: 7.4) was added to a round bottom flask and 100 µL of EDCI (0,47 µg/mL) and 100 µL of NHS (0,35 µg/mL) were added in a ratio of [Antibody]: [EDCI/NHS] 1:10 (The amounts used for the calculation are shown in Table 3.3) and stirred on a magnetic stirrer at 1000 rpm for 30 minutes. At the end of 30 minutes, 4 mL of Cy3-Ch-NP solution was added to the antibody with the carboxylic acid group activated as NHS ester and the reaction was stirred on a magnetic stirrer for 4 hours at room temperature. After 4 hours, the reaction was moved to a room kept at 4°C and continued in the dark for 18 hours. In this way, NHS-activated antibodies were covalently bound to the free amine groups on the surface of chitosan nanoparticles by amide bonds. After 18 hours, the obtained antibody and flourescent dye conjugated nanoparticles (Cy3-CD11b-Ch-NPs) were purified via centrifugation against ddH_2O with Amicon ultracentrifuge tubes (MW cut-off: 100 kDa) at 2500 rpm for 3 min and this process was repeated five times. Following the

centrifugation, nanoparticles filtered again using a 0,22 μm PES filter to eliminate large aggregates.

Table 3.3. Chemicals and amounts used in the Cy3-Ant-NP Anti-CD11b binding reaction.

Chemical	Equivalent	Molecular Weight (g/mol)	Mol (μmol)	Mass (μg)	Volume (mL)
Anti-CD11b	1	165×10^{-3}	$3{,}03 \times 10^{-3}$	50	
EDCI	10	155,2	$3{,}03 \times 10^{-3}$	0,47	
NHS	10	115,09	$3{,}03 \times 10^{-3}$	0,35	
PBS					25 mL

3.2.4.3.1 BCA Assay

The bicinchoninic acid assay (BCA) protein quantification method was used to calculate how much antibody was bound to the surface of the antibody-bound nanoparticles. The BCA method is a two-step colorimetric protein quantification method based on the mechanics of the biuret reaction, which allows highly sensitive measurements over a wide range of 0,02-2 mg/mL. In the first step of the reaction, the reduction of Cu^{+2} copper ions in an alkaline medium to the Cu^{+} form by peptide bonds in the protein-based compound takes place. In the second step, the BCA molecule combines with the reduced copper cations to form a purple BCA-Copper complex. This water-soluble complex gives a strong absorbance at 562 nm, measured with a UV-Vis spectrophotometer.

For the determination of antibody content in nanoparticles, standards in the range of 2-50 μg/mL were prepared according to the kit's (TaKaRa BCA Protein Assay Kit, #T9300A) own procedure and a standard calibration curve was obtained (Details of the calibration curves created are given in the Appendices). For the measurement of the samples, BCA solution was added to the samples as indicated in the kit, incubated at 37°C for 30 minutes and then measured at 562 nm on a plate reader.

3.2.4.4 Preparation of Brain and Microglia Targeted (Dual Targeted) Nanoparticles (T7-LA-Ch-NPs and CD11b-T7- LA-Ch-NPs)

For the preparation of brain-targeted nanoparticles, in the first step, T7-PEG-ss-NHS conjugated to pre-prepared LA-Ch-NPs, and on the other hand, CD11b antibody attached to T7 conjugated nanoparticles (CD11b-T7- LA-Ch-NPs) prepared to obtain dual targeted nanoparticles.

In order to prepare T7-LA-Ch-NPs, 0.375 mg of T7-PEG-ss-NHS was weighed and added into the 2 mL of previously prepared LA-Ch-NP solution ([Conjugate]:[Nanoparticle], 1:10) and left overnight on a magnetic stirrer at 1000 rpm, RT. The following day, obtained nanoparticles (T7-LA-Ch-NPs) were ultrafiltered 5 times against ultra distilled water (ddH2O) using an Amicon ultracentrifuge filter (Mw cut-off: 100 kDa) to remove unbound polymeric aggregates and was sonicated for two minutes, respectively. Meanwhile, the Anti-CD11b antibody was activated using EDC/NHS chemistry, as detailed in section 3.2.4.3, with the exact amounts in Table 3. Then, previously prepared 2 mL T7-LA-Ch-NP solution was added to the activated antibody solution, and the reaction was moved to a room kept at 4°C and continued in the dark for 18 hours. After 18 hours, obtained CD11b-T7- LA-Ch-NPs were ultrafiltered 3 times against ddH2O using an Amicon ultracentrifuge filter to remove excessive amounts of solvent and unbound molecules. After centrifugation, nanoparticles were again filtered using a 0,22 µm PES filter to eliminate large aggregates. The synthesis of dual-targeted nanoparticles is illustrated in Figure 3.5.

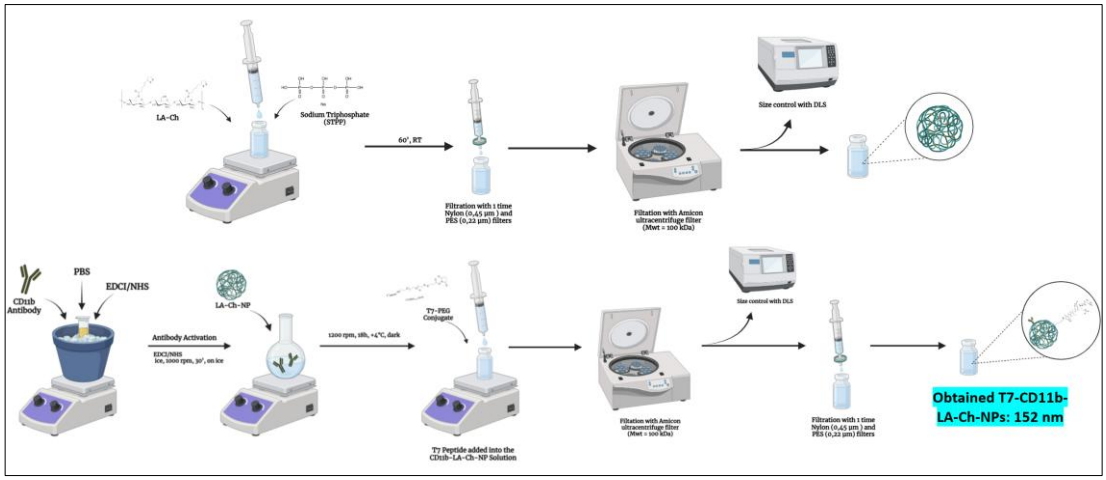

Figure 3.5. Summary of the CD11b-T7-LA-Ch-NPs. (created with Biorender.com).

Subsequently, in order to show that the PEG chains on the surface of the obtained nanoparticles are peelable, the "peeling" test was performed at different time intervals by reacting the disulfide bonds (-S-S-) of the T7-PEG-S-S-NHS conjugate used in surface modification with reduced Glutathione (GSH-SH) in acidic medium. Accordingly, previously prepared T7-Ch-NPs were diluted in water with concentrations of 0.2 mM and 1 mM and 1 mL of the prepared GSH-SH solution was added to 1 mL of T7-Ch-NPs and placed on an orbital stirrer for 60 minutes at RT and DLS measurements of the nanoparticles were taken at 5 minute intervals (0, 5, 10, 15, 15, 20, 20, 25, 30, 35, 40, 45, 50, 55, 60 minutes).

3.2.5 Characterization of NPs

The characterization studies of all nanoparticles synthesized within the scope of the thesis project utilized a variety of analytical methods. DLS analysis was used to determine the size, Zeta potential analysis was used to measure surface charge, FT-IR and ^{1}H-NMR was used for chemical characterization and, SEM and TEM microscopes were used for morphological analysis.

3.3 In-Vitro Experiments

3.3.1 In Vitro Cytotoxicity Assay (CCK-8)

Cytotoxicity tests were performed using the Cell Counting Kit-8 (CCK-8, GLPBIO) on Mouse microglial EOC-20 (*ATCC CRL-2469*) and Mouse skin fibroblast L929 (*ATCC CCL-1*) cell lines.

L929 fibroblast cells were incubated in complete DMEM medium containing 10% FBS and 1% penicillin in a CO_2 incubator at 5% CO_2, 90% humidity and 37°C, changing the medium every two days until the cells reached 80-100% density. Cells were washed with 1X PBS and incubated in 0,25% trypsin-EDTA solution at 37°C for 5 minutes. Afterwards, trypsin was deactivated with medium at room temperature and the detached cells were collected and centrifuged at 800 g for 5 minutes. After centrifugation, the supernatant was carefully discarded and the cells were resuspended in the medium. For cell counting, 10 µL of the thawed cell solution was mixed with trypan blue at a ratio of 1:1 and cells were counted on a hemacytometer using light microscope

EOC-20 microglia cells were cultured in complete DMEM/F-12 medium containing 10% FBS and 1% penicillin in a CO_2 incubator at 5% CO_2, 90% humidity and 37°C, changing the medium every two days until the cells reached 80-100% density. The medium was removed to leave 2-3 mL on the surface of the cells and the cells were removed from the surface of the flask with a cell scraper. The removed cells were then collected and centrifuged at 600 g for 5 minutes. After centrifugation, the supernatant was carefully discarded and the cells were resuspended in the medium. For cell counting, 10 µL of the thawed cell solution was mixed with trypan blue at a ratio of 1:1 and cells were counted on a hemacytometer using light microscope.

After cell counting, cells were seeded with 10^4 cells/100µL medium in each well of a 96-well plate and incubated at 5% CO_2, 37°C for 24 hours to allow cells to attach. The next day, after removing the medium from the cells, different groups of samples (Ch-NP, LA-Ch-NP, T7-PEG conjugate, and Free-LA molecules) prepared in medium with a total volume of 100 µL and sterilized under UV for 2 hours before application were added to the cells. Wells with only medium added cells were used as positive controls. All samples were added to the wells in n=3 replicates. The cells were then incubated at 5% CO_2, 37°C for 24 hours. After 24 hours of incubation, 10 µL of CCK-8 reagent was added to each well and incubated for 1.5 h at 37 $^{\circ}$C, 5% CO_2. After 1.5 hours of incubation, the results were obtianed by a microplate reader at 450 nm.

4. RESULTS

4.1 Nanoparticle Preparation and Characterization

4.1.1 Preparation and Characterization of Chitosan Nanoparticles (Ch-NPs)

In order to find an optimum procedure, a variety of nanoparticle formulations were prepared by changing the molecular weight and/or concentration of the polymer, polymer/crosslinker [C]:[T] ratio, solvent amount, reaction time, and filtering method parameters, resulting in the most suitable size nanoparticle formation according to the measurements and analyses.

Nanoparticles were prepared with chitosan polymer, a widely used polysaccharide that is biocompatible and biodegradable. It is especially outstanding due to its ability to remain stable in the bloodstream at the nanoscale (125,126). Polymer solutions were prepared with low (50-190 kDa) and medium (200-310 kDa) molecular weight chitosan polymers (Sigma Aldrich, catalog number 448869, 448877 for the low and medium molecular weight, respectively). These polymers were subjected to reaction with STPP at a [C]:[T] ratio of 1:1 and 1:0.5 (RT, 1000 rpm). The reaction was continued for 15, 30, 60, and 120 minutes to prepare nanoparticles, filtered using different syringe filters to eliminate oversized polymeric aggregates.

First, to select the molecular weight of the chitosan polymer, polymers with low and medium molecular weight were reacted for 60 min at 0,1 wt% and [C]:[T] ratio of 1:1 and 1:0.5 by volume. In the measurements taken immediately after the reaction, large aggregations were observed in the nanoparticles prepared with the medium molecular weight. When the batches prepared at two different [C]:[T] ratios were compared, it was observed that low molecular weight chitosan formed smaller and homogeneous nanoparticles in both (Figure 4.1 & 4.2).

The nanoparticles prepared with medium-weight polymer had larger sizes and higher PDI values, which can be attributed to the fact that the chains of the polymer were not sufficiently saturated with the crosslinker due to the longer length of the polymer chains compared to the low-weight polymer and polymerized by forming large sized particles by folding on itself. In further studies, nanoparticles prepared under the same conditions were filtered using different filters. During filtration, it was observed that the nanoparticles prepared with medium molecular weight chitosan, in particular, were very difficult to pass through the filters from the first filtration, resulting in a large amount of material loss. Thus, it was decided to continue with low molecular weight chitosan polymer to prepare other nanoparticles.

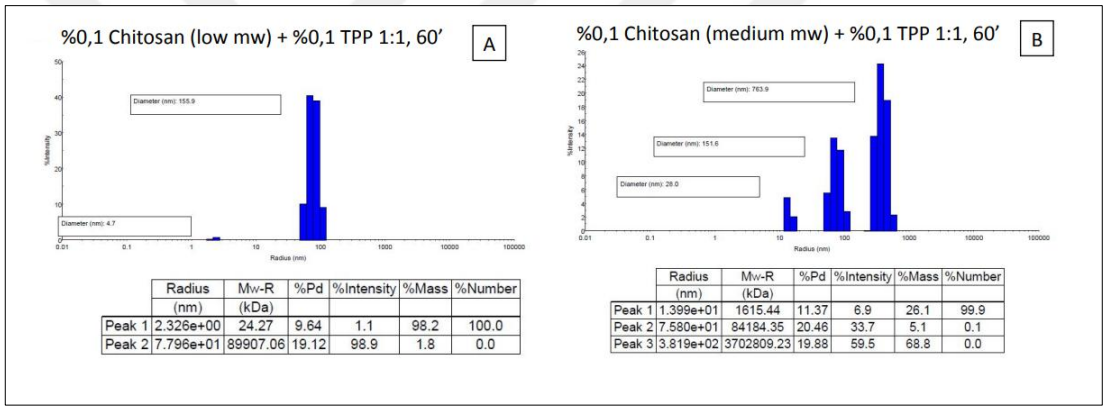

	Radius (nm)	Mw-R (kDa)	%Pd	%Intensity	%Mass	%Number
Peak 1	2.326e+00	24.27	9.64	1.1	98.2	100.0
Peak 2	7.796e+01	89907.06	19.12	98.9	1.8	0.0

	Radius (nm)	Mw-R (kDa)	%Pd	%Intensity	%Mass	%Number
Peak 1	1.399e+01	1615.44	11.37	6.9	26.1	99.9
Peak 2	7.580e+01	84184.35	20.46	33.7	5.1	0.1
Peak 3	3.819e+02	3702809.23	19.88	59.5	68.8	0.0

Figure 4.1. Effect of the molecular weight to the NP size. Comparison of nanoparticles prepared with low and medium molecular weight polymer at 1:1 Polymer:Crosslinker ratio. **(A)** NPs prepared with 0.1% low molecular weight chitosan at 1:1 ratio; **(B)** NPs prepared with 0.1% medium molecular weight chitosan at 1:1 ratio.

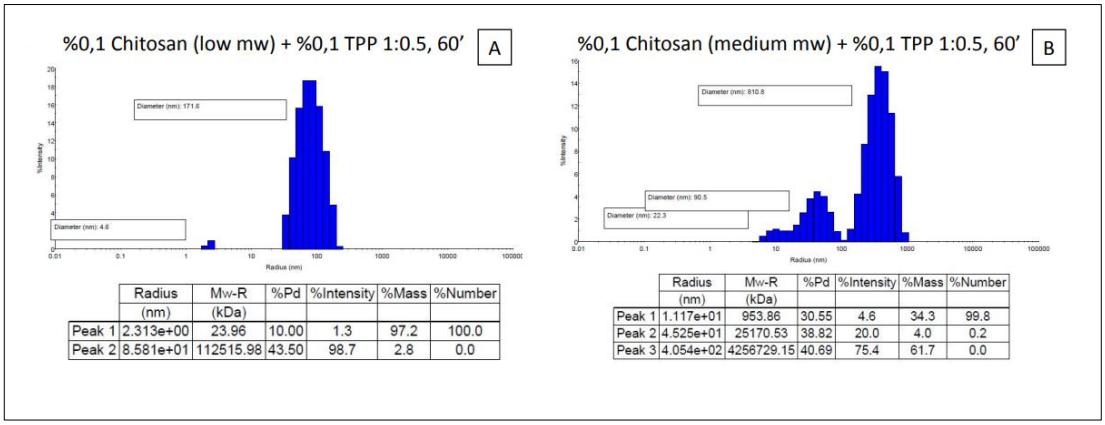

	Radius (nm)	Mw-R (kDa)	%Pd	%Intensity	%Mass	%Number
Peak 1	2.313e+00	23.96	10.00	1.3	97.2	100.0
Peak 2	8.581e+01	112515.98	43.50	98.7	2.8	0.0

	Radius (nm)	Mw-R (kDa)	%Pd	%Intensity	%Mass	%Number
Peak 1	1.117e+01	953.86	30.55	4.6	34.3	99.8
Peak 2	4.525e+01	25170.53	38.82	20.0	4.0	0.2
Peak 3	4.054e+02	4256729.15	40.69	75.4	61.7	0.0

Figure 4.2. Effect of the molecular weight to the NP size. Comparison of nanoparticles prepared with low and medium molecular weight polymer at 1:0.5 Polymer:Crosslinker ratio. **(A)** NPs prepared with 0.1% low molecular weight chitosan at 1:0.5 ratio; **(B)** NPs prepared with 0.1% medium molecular weight chitosan at 1:0.5 ratio.

The experiments were performed simultaneously to optimize reaction time and filtration. First, the previously described procedure was repeated using low molecular weight chitosan at different intervals. 0,05 wt% STPP was added to 0,1 wt% low molecular weight chitosan solution and continued on a magnetic stirrer at RT, 1000 rpm for 15, 30, 60, and 120 min, respectively. After the reaction, it was decided to continue with 30 minutes and longer since no difference was observed between 15-minute and 30-minute samples. Samples prepared with 120 minutes reaction time could not be measured with DLS due to precipitation.

Subsequently, all prepared nanoparticles were filtered with 0,45 µm Nylon and 0,22 µm Polyethersulfone (PES) filters, and the size was measured again with the DLS instrument. The graphs in Figure 4.3, showing the size measurements taken immediately after 30 and 60 minutes of reaction without filtering, indicate that the nanoparticle size decreased with time for both groups (1:1 and 1:0.5) and the %PDI value, i.e., the polydispersity value, also decreased. According to the comparison of these data with the post-filtration samples in Tables 4.1 and 4.2, it was observed that the samples with the smallest size and %PDI value were obtained in the samples filtered twice after 60 minutes reaction time in the samples prepared 1:1, while in the

samples prepared 1:0.5, it was observed that the nanoparticles with 120 minutes reaction time under the same conditions had the desired size and %PDI value. In both groups, micron-sized particles were observed in the samples passed through the third filter (the second 0,22 µm PES filter) after the first 2 filtrations, which are considered to be formed by aggregates due to pressure.

As a result, when the time-dependent size data of the nanoparticles prepared at both ratios were evaluated, it was observed that the targeted size nanoparticles with the highest density and lowest %PDI value were achieved with a reaction time of 60 minutes. Therefore, it was decided that the reaction time required for the subsequent optimization steps should be 60 minutes.

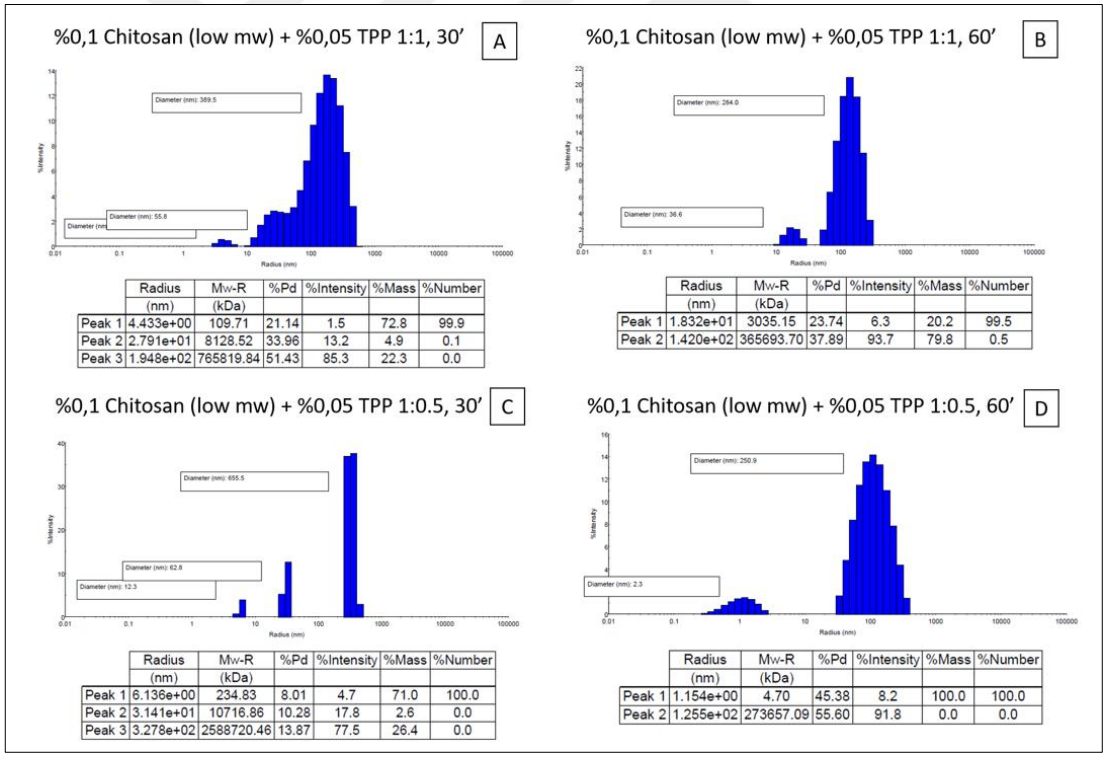

	Radius (nm)	Mw-R (kDa)	%Pd	%Intensity	%Mass	%Number
Peak 1	4.433e+00	109.71	21.14	1.5	72.8	99.9
Peak 2	2.791e+01	8128.52	33.96	13.2	4.9	0.1
Peak 3	1.948e+02	765819.84	51.43	85.3	22.3	0.0

	Radius (nm)	Mw-R (kDa)	%Pd	%Intensity	%Mass	%Number
Peak 1	1.832e+01	3035.15	23.74	6.3	20.2	99.5
Peak 2	1.420e+02	365693.70	37.89	93.7	79.8	0.5

	Radius (nm)	Mw-R (kDa)	%Pd	%Intensity	%Mass	%Number
Peak 1	6.136e+00	234.83	8.01	4.7	71.0	100.0
Peak 2	3.141e+01	10716.86	10.28	17.8	2.6	0.0
Peak 3	3.278e+02	2588720.46	13.87	77.5	26.4	0.0

	Radius (nm)	Mw-R (kDa)	%Pd	%Intensity	%Mass	%Number
Peak 1	1.154e+00	4.70	45.38	8.2	100.0	100.0
Peak 2	1.255e+02	273657.09	55.60	91.8	0.0	0.0

Figure 4.3. Effect of the reaction time to the NP size. Comparison of nanoparticles prepared with low molecular weight polymer with 1:0.5 and 1:1 [C]:[T] ratios at different time intervals. (A) NP prepared with 1:1 ratio of 0.1% Low molecular weight chitosan and 0,05% STPP in 30 min; (B) NP prepared with 1:1 ratio of 0,1% Low molecular weight chitosan and 0.05% STPP in 60 min; (C) NP prepared with 1:0.5 ratio of 0,1% Low molecular weight chitosan and 0,05% STPP in 30 min; (D)

NP prepared with 1:0.5 ratio of 0,1% Low molecular weight chitosan and 0,05% STPP in 60 min.

Table 4.1. Effect of the reaction time and filtration to the NP size. Comparison of nanoparticles prepared with low molecular weight polymer with 1:0.5 [C]:[T] ratios at different time intervals and filtered using two different filters.

1:0.5, 30’				1:0.5, 60’				1:0.5, 120’			
Filter	**Radius (nm)**	**PDI (%)**	**Intensity (%)**	**Filter**	**Radius(nm)**	**PDI (%)**	**Intensity (%)**	**Filter**	**Radius(nm)**	**PDI (%)**	**Intensity (%)**
Before filter	655.5	13.87	77.5	**Before filter**	274	20.35	34.2	**Before filter**	*could not be measured because of aggregation		
1x Nylon (0,45 µm)	343.7	54.26	62.7	**1x Nylon (0,45 µm)**	182.6	82.95	100	**1x Nylon (0,45 µm)**	178.9	33.11	98
1x Nylon (0, 45 µm) + 1x PES (0,22 µm)	115.8	97.99	100	**1x Nylon (0, 45 µm) + 1x PES (0,22 µm)**	193.4	69.85	100	**1x Nylon (0, 45 µm) + 1x PES (0,22 µm)**	147.5	19.14	100
1x Nylon (0,45 µm) + 2x PES (0,22 µm)	415.6	46.38	89.9	**1x Nylon (0,45 µm) + 2x PES (0,22 µm)**	3115.5	284.05	100	**1x Nylon (0,45 µm) + 2x PES (0,22 µm)**	170.5	39.43	100

Table 4.2. Effect of the reaction time and filtration to the NP size. Comparison of nanoparticles prepared with low molecular weight polymer with 1:1 [C]:[T] ratios at different time intervals and filtered using two different filters.

1:1, 30’				1:1, 60’				1:1, 120’			
Filter	**Radius (nm)**	**PDI (%)**	**Intensity (%)**	**Filter**	**Radius(nm)**	**PDI (%)**	**Intensity (%)**	**Filter**	**Radius (nm)**	**PDI (%)**	**Intensity (%)**
Before filter	389.5	51.43	85.3	**Before filter**	260.8	98.07	98.4	**Before filter**	*could not be measured because of aggregation		
1x Nylon (0,45 µm)	150	13.91	83.7	**1x Nylon (0,45 µm)**	145.1	53.78	99	**1x Nylon (0,45 µm)**	295.8	15.28	63.4
1x Nylon (0, 45 µm) + 1x PES (0,22 µm)	198.	32.95	94.5	**1x Nylon (0, 45 µm) + 1x PES (0,22 µm)**	133.1	87.55	95.1	**1x Nylon (0, 45 µm) + 1x PES (0,22 µm)**	243.2	78.67	94.5
1x Nylon (0,45 µm)	362.1	60.94	75.5	**1x Nylon (0,45 µm)**	2587.9	310.51	100	**1x Nylon (0,45 µm)**	203.3	67.23	92.5

+ 2x PES (0,22 µm)		**+ 2x PES (0,22 µm)**	**+ 2x PES (0,22 µm)**

In order to determine the effect of different types of filters on nanoparticle size, two different nanoparticle solutions containing 0.05 wt% low molecular weight chitosan and 0.05 wt% STPP with [C]:[T] ratios of 1:1 and 1:0.5 were prepared and reacted on a magnetic stirrer at room temperature for 60 minutes. After the reaction, the nanoparticles were filtered using Nylon (0,45 μm), PES (0,22 μm) and two different RC (Regenerated Cellulose; 0,45 and 0,22 μm) syringe filters.

As shown in Table 4.3, the closest value to the targeted size was obtained when the RC filter was used compared to other filters. However, it was concluded that the use of the RC filter was not comfortable due to the fact that the filter clogged very quickly during filtering and the loss of material was also high, and it was eliminated. In addition, it was decided to filter the prepared nanoparticles first through a 0,45 μm filter and then through a 0,22 μm filter, since it was observed that the filters were clogged when these filters were used twice in a row while using 0,45 μm filters during the experiments. In the following experiments, the nanoparticles were first passed through a 0,45 μm Nylon filter and then through a PES filter 5 more times and their sizes were controlled at each step. For both 1:1 and 1:0.5, it was decided to filter the nanoparticles 1 time through 0,45 μm Nylon and 1 time through 0,22 μm PES filters for the next experiments due to the minimum material loss and obtaining the optimal size.

Table 4.3. Effect of the different filters to the NP size.Comparison of nanoparticles prepared with 1:1 and 1:0.5 [C]:[T] ratios containing 0.05% STPP, 0.05% STPP, 0.05% chitosan, 60 min and filtered with different filters.

1:1, 60'				1:0.5, 60'			
Filter	**Radius (nm)**	**PDI (%)**	**Intensity (%)**	**Filter**	**Radius (nm)**	**PDI (%)**	**Intensity (%)**
Before filter	240.7	38.30	98.9	**Before filter**	222.2	35.09	81.6
1x Nylon (0,45 µm)	311.6	16.64	100	**1x Nylon (0,45 µm)**	189.2	11.67	98.5
2x Nylon (0,45 µm)	214.7	30.06	98.2	**2x Nylon (0,45 µm)**	209.4	33.15	98.5
2x Nylon (0, 45 µm) + 1x PES (0,22 µm)	187.3	12.96	97.5	**2x Nylon (0, 45 µm) + 1x PES (0,22 µm)**	221.5	35.90	98.2
2x Nylon (0,45 µm) + 2x PES (0,22 µm)	209.4	32.59	100	**2x Nylon (0,45 µm) + 2x PES (0,22 µm)**	181.2	23.44	92.9
2x Nylon (0,45 µm) + 5x PES (0,22 µm)	187.8	34.38	100	**2x Nylon (0,45 µm) + 5x PES (0,22 µm)**	167.3	44.08	92.4
1x RC (0,45 µm)	224.8	30.97	100	**1x RC (0,45 µm)**	235.3	15.13	98.7
2x RC (0,45 µm)	184.6	16.45	100	**2x RC (0,45 µm)**	159.9	11.02	100
2x RC (0,45 µm) + 1x RC (0,22 µm)	210.4	16.19	98.8	**2x RC (0,45 µm) + 1x RC (0,22 µm)**	210.4	38.82	100
2x RC (0,45 µm) + 2x RC (0,22 µm)	199.3	23.96	100	**2x RC (0,45 µm) + 2x RC (0,22 µm)**	210.8	13.1	99.6

After deciding the optimum reaction time and filtration process to obtain nanoparticles with high density and low PDI value, the effect of the wt% of the polymer solution on the nanoparticle size was investigated at 1:1 and 1:0.5 [C]:[T] ratios by volume. In this step, low molecular weight chitosan polymer solutions of 0,1 wt% and 0,05 wt% were prepared maintaining the wt% of crosslinker constant (0,05 wt% STPP). The crosslinker and polymer solutions were prepared as 1:1 and 1:0.5 in two groups and placed on a magnetic stirrer at 1000 rpm for 60 minutes. The size of the obtained nanoparticles was measured by DLS after filtering once with Nylon and PES filters, respectively, and it was observed that the samples prepared at 1:1 in both polymer concentrations had lower size and PDI value (Figure 4.4 & 4.5). Especially

in the group with 1:1 ratio and 0.1 wt% of polymer, nanoparticles had the closest value to the target value (132. 7 nm) and the nanoparticles with the lowest PDI value were prepared and therefore, it was decided to use 0.1 wt% of polymer in future studies (Figure 4.5A).

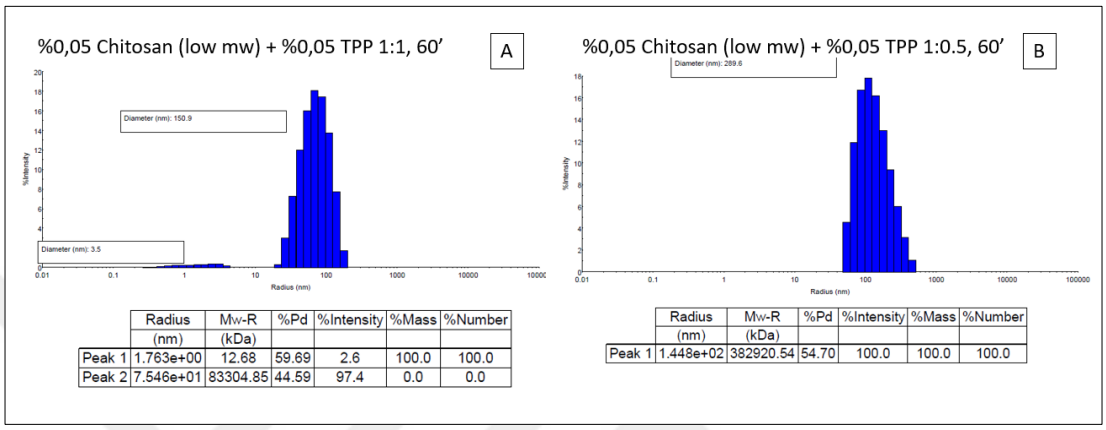

	Radius (nm)	Mw-R (kDa)	%Pd	%Intensity	%Mass	%Number
Peak 1	1.763e+00	12.68	59.69	2.6	100.0	100.0
Peak 2	7.546e+01	83304.85	44.59	97.4	0.0	0.0

	Radius (nm)	Mw-R (kDa)	%Pd	%Intensity	%Mass	%Number
Peak 1	1.448e+02	382920.54	54.70	100.0	100.0	100.0

Figure 4.4. Effect of the polymer concentration to the NP size. Comparison of nanoparticles prepared with 0,05 wt% STPP and 0,05 wt% polymer at 1:0.5 and 1:1 [C]:[T] ratios for 60 min. (A) NP prepared with 0,05 wt% low molecular weight chitosan at 1:1 ratio; (B) NP prepared with 0.05 wt% low molecular weight chitosan at 1:0.5 ratio.

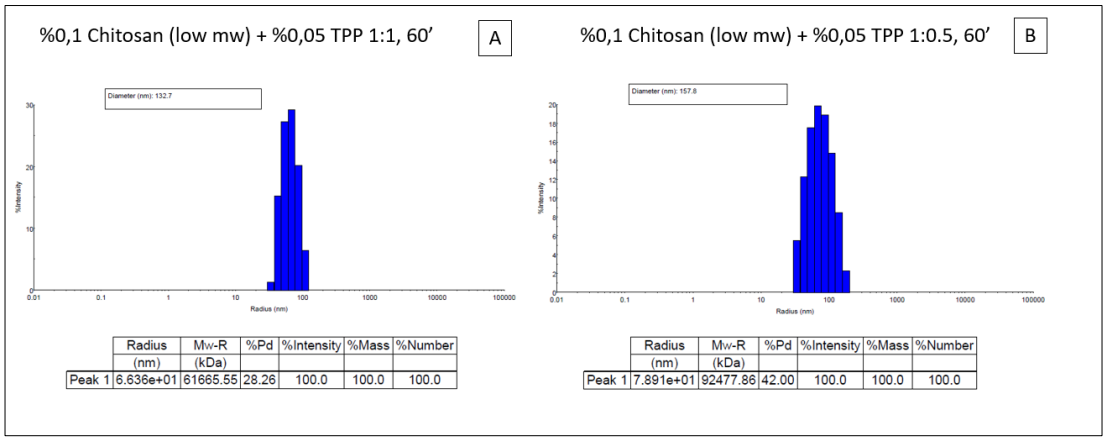

	Radius (nm)	Mw-R (kDa)	%Pd	%Intensity	%Mass	%Number
Peak 1	6.636e+01	61665.55	28.26	100.0	100.0	100.0

	Radius (nm)	Mw-R (kDa)	%Pd	%Intensity	%Mass	%Number
Peak 1	7.891e+01	92477.86	42.00	100.0	100.0	100.0

Figure 4.5. Effect of the polymer concentration to the NP size. Comparison of nanoparticles prepared with 0,05 wt% STPP and 0,1 wt% polymer at 1:0.5 and 1:1 [C]:[T] ratios for 60 min. (A) NP prepared with 0,1 wt% low molecular weight chitosan at 1:1 ratio; (B) NP prepared with 0.1 wt% low molecular weight chitosan at 1:0.5 ratio.

In order to determine the effect of the wt% of the crosslinker on the nanoparticle size, the wt% of the crosslinker, which was previously tested at 0,05 wt% and 0,1 wt%, was reduced to 0,01 wt%. As shown in the DLS graph in Figure 6-A, it is clearly seen that the nanoparticle size prepared with 0,01% STPP has a much lower size and lower PDI value compared to the nanoparticle size prepared using 0.05% STPP (Figure 4.6A) under the same conditions. At the same time, when all the results obtained are considered, it can be seen that the PDI values of the nanoparticles prepared with a [C]:[T] ratio of 1:1 are lower than those prepared with 1:0.5, indicating that the size distribution of the nanoparticles is more homogeneous.

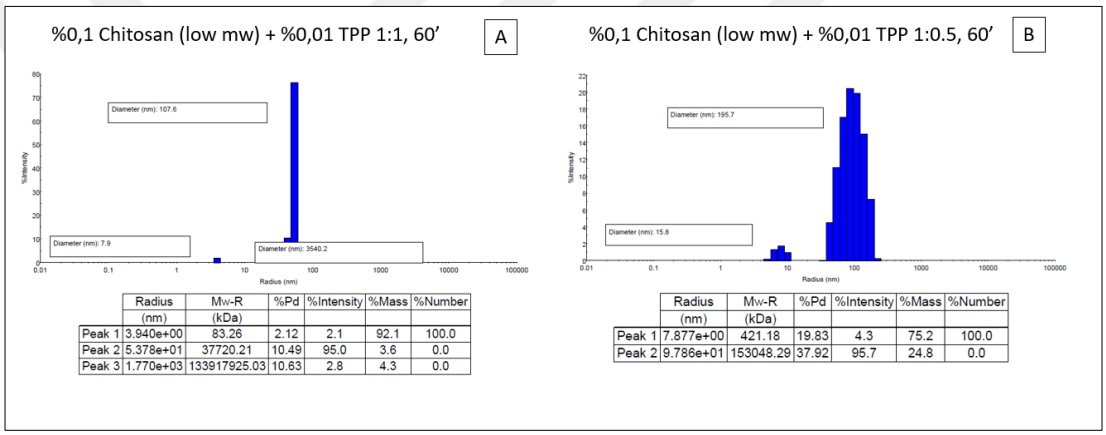

	Radius (nm)	Mw-R (kDa)	%Pd	%Intensity	%Mass	%Number
Peak 1	3.940e+00	83.26	2.12	2.1	92.1	100.0
Peak 2	5.378e+01	37720.21	10.49	95.0	3.6	0.0
Peak 3	1.770e+03	13391925.03	10.63	2.8	4.3	0.0

	Radius (nm)	Mw-R (kDa)	%Pd	%Intensity	%Mass	%Number
Peak 1	7.877e+00	421.18	19.83	4.3	75.2	100.0
Peak 2	9.786e+01	153048.29	37.92	95.7	24.8	0.0

Figure 4.6. Effect of the crosslinking concentration to the NP size. Comparison of nanoparticles prepared with 0,1 wt% polymer and 0,01 wt% STPP at 1:0.5 and 1:1 [C]:[T] ratios for 60 min. (A) NP prepared with 0,01 wt% STPP at 1:1 ratio; (B) NP prepared with 0,01 wt.% STPP at 1:0.5 ratio.

Given all the results obtained, it was decided to proceed to further studies with nanoparticles with a diameter of 107.6 nm, a PDI value of 10,49%, and a density as high as 95%, prepared by filtering with 1 time Nylon and 1 time PES filter after 60 minutes, reaction at RT using 0.1% low molecular weight Chitosan, and 0.01% STPP in a 1:1 ratio.

After all optimizations, the prepared Ch-NPs were characterized physically, chemically and morphologically. In addition to the DLS size measurement used in each

step of the optimisations, Zeta potential for surface charge measurement, FTIR and ^{1}H-NMR for functional group analysis and chemical structure analysis respectively, SEM and TEM analyses for morphological analysis were performed.

The prepared nanoparticles are expected to have a positive charge due to the free (deacetylated) amine (-NH_2) groups on the side branches of the chitosan polymer. The obtained Ch-NPs were diluted 1:10 by volume with 10 mM NaCl solution and surface charge measurements (three repeated measurements) were performedwith LitesizerTM 500 (Anton-Paar) instrument. As shown in Figure 4.7, they were found to be positively charged at +14.2 ±4,03 mV.

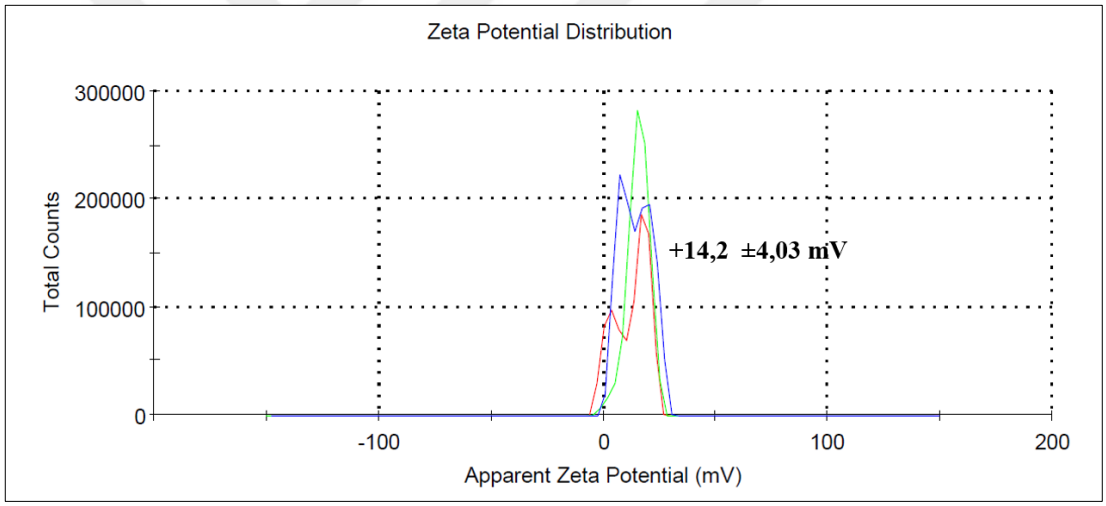

Figure 4.7. Zeta potential measurement of Ch-NPs.

In the scope of chemical structure characterization, the presence of polymer and crosslinker molecules in the structure of the Ch-NPs was demonstrated using the FT-IR Spectroscopy method, which allows the determination of functional groups. The nanoparticle solution was frozen at -20 ˚C, lyophilized, dried, and powdered for these analyses. As shown in the comparative FT-IR spectra in Figure 4.8, functional groups with free protons from chitosan polymer can be easily seen in the range of 3200-3300 cm^{-1} in the structure of the obtained nanoparticles. Furthermore, carbonyl peaks

belonging to the amide groups in the structure of chitosan are seen in the range of 1640-1550 cm^{-1} and 1400-1300 cm-1, respectively. Although the characteristic peaks referring to the phosphate bonds coming from the structure of the crosslinking molecule STPP are seen around 1100 cm^{-1} as expected, the peak at 862 cm^{-1}, which is mainly seen in the spectrum of nanoparticles, comes from the P-O-P group of the crosslinking molecule (127). Thus, it has been confirmed that the prepared nanoparticles are not only polymer aggregates but also nanostructures crosslinked with STPP molecules.

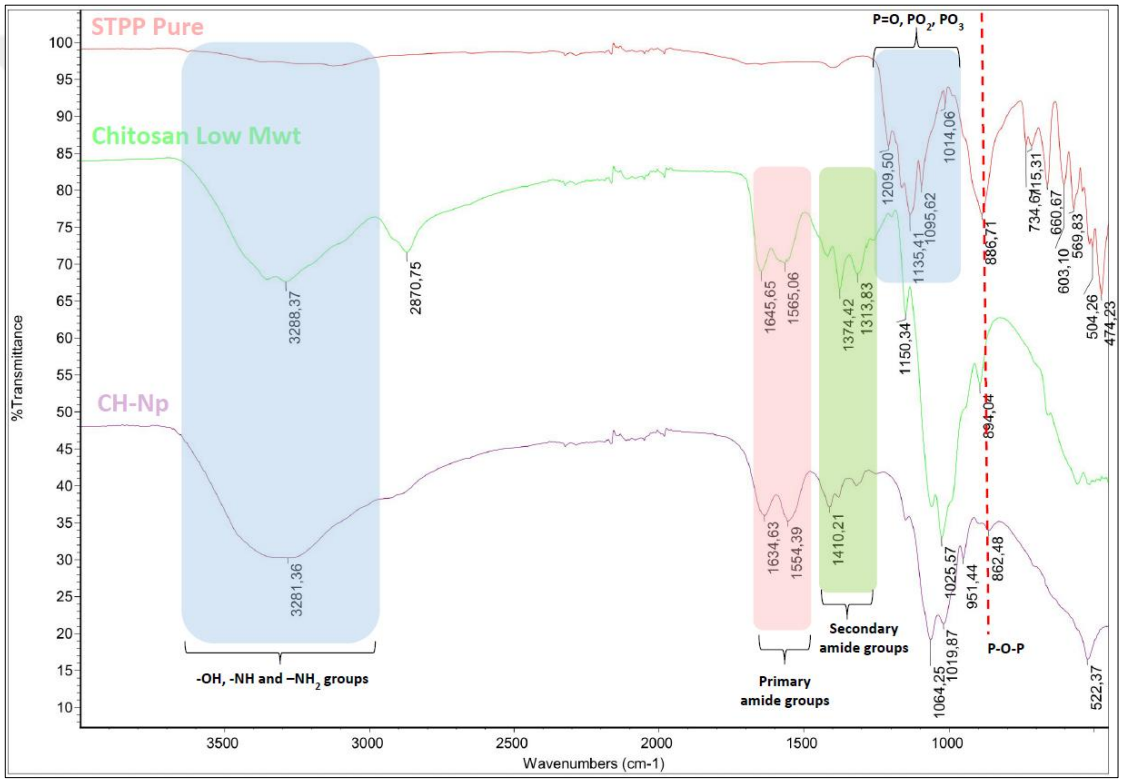

Figure 4.8. Comparative FT-IR spectra for chitosan nanoparticles (Ch-NPs).

Subsequently, NMR spectroscopy of the prepared nanoparticles was performed. The lyophilised and powdered nanoparticles were suspended in deuterated water (D_2O) in accordance with the literature, and ^{1}H-NMR spectra were acquired using 128 scans. Only major chitosan peaks were observed in the NMR spectrum due to both the physical nanofolding of the nanoparticles and the amount (Figure 4.9).

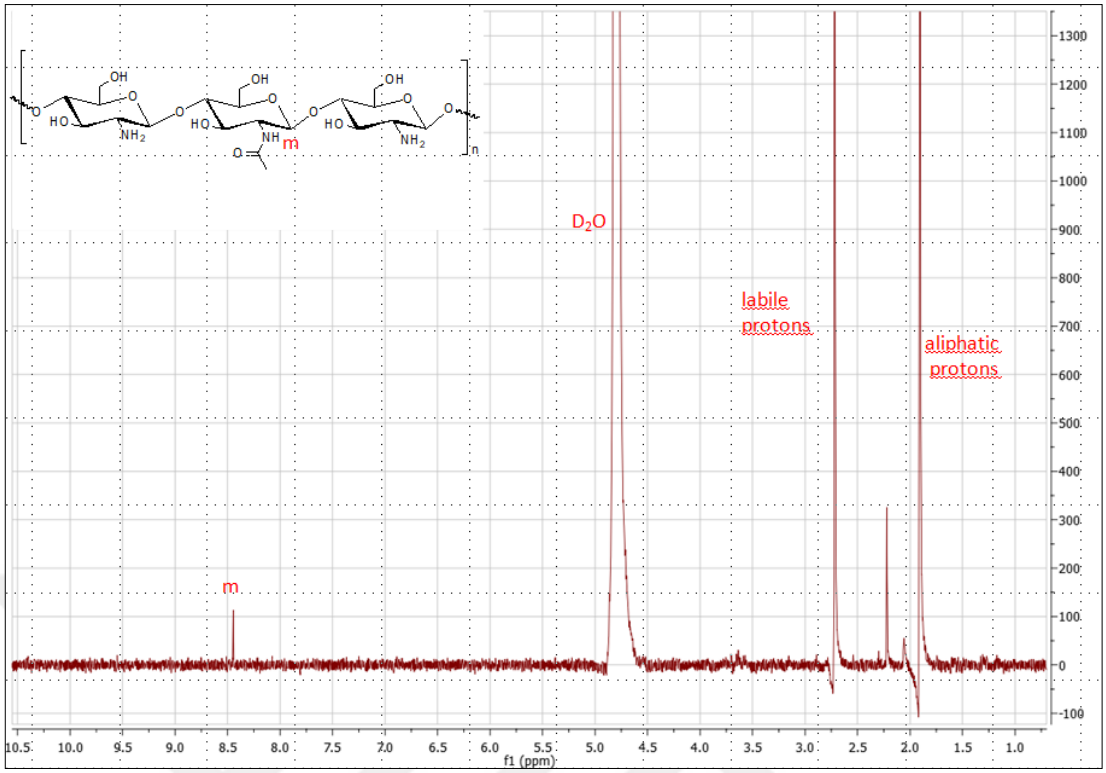

Figure 4.9. Proton NMR spectrum (in D_2O) for chitosan nanoparticle (Ch-NP).

The morphological analysis of the nanoparticles was performed both by SEM (Scanning Electron Microscopy) and TEM (Transmission Electron Microscopy). For TEM imaging, the grids supported by the instrument were used. For SEM imaging, analyses were performed by coating the nanoparticles placed on carbon tape with gold under vacuum. In the micrographs from both microscopes, it was observed that the nanoparticles had a round-shaped morphology and had a diameter of approximately 90-100 nm due to the high vacuum applied in the measurements (Fig. 4.10).

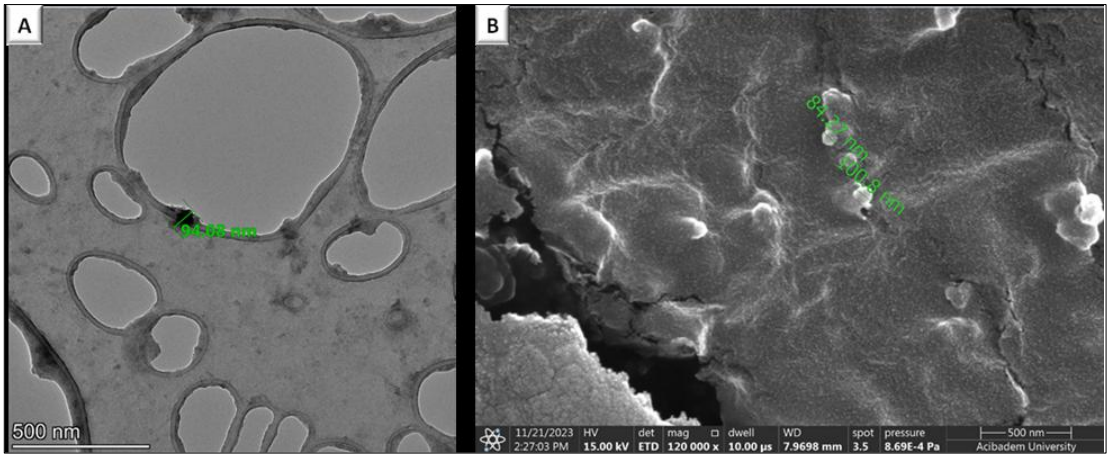

Figure 4.10. Morphological analysis results of Ch-NPs. (A) TEM microgpraph, (B) SEM micrograph.

The last nanoparticle characterisation step, the stability test, was performed by time-dependent DLS monitoring of the nanoparticle size. Nanoparticles prepared at the suitable size (107.6 nm) were diluted 1:2 by volume with 10 mM PBS buffer solution (pH:7.4) and acetate buffer solution (pH:5.5) and incubated at 37°C. The samples were taken at specific time points for 2 weeks and their size was measured by the DLS instrument.

The results demonstrated that the size of the nanoparticles increased to approximately 200 nm in the first 3-4 days in acidic medium, meaning that the nanoparticle swelled, but then remained almost constant. However, this indicates that the nanoparticles are stable in mild acidic medium. It is also observed that the swelling is higher in neutral medium and the nanoparticles exceed 300 nm in size from the first week (Figure 4.11). These two trends indicate that when the prepared chitosan-based nanoparticles are introduced into the bloodstream, they will rapidly increase in size and lose stability if they remain in circulation for a long time, which indicates that targeting of the nanoparticles is essential and they should be rapidly deposited at the target site. On the other hand, the stability of these nanoparticles in acidic environment strengthens the possibility that these nanoparticles, which rapidly reach the

inflammation site after targeting, can slowly swell and decompose, that is, remain stable for a long time and release the drug in a controlled and slow manner as expected.

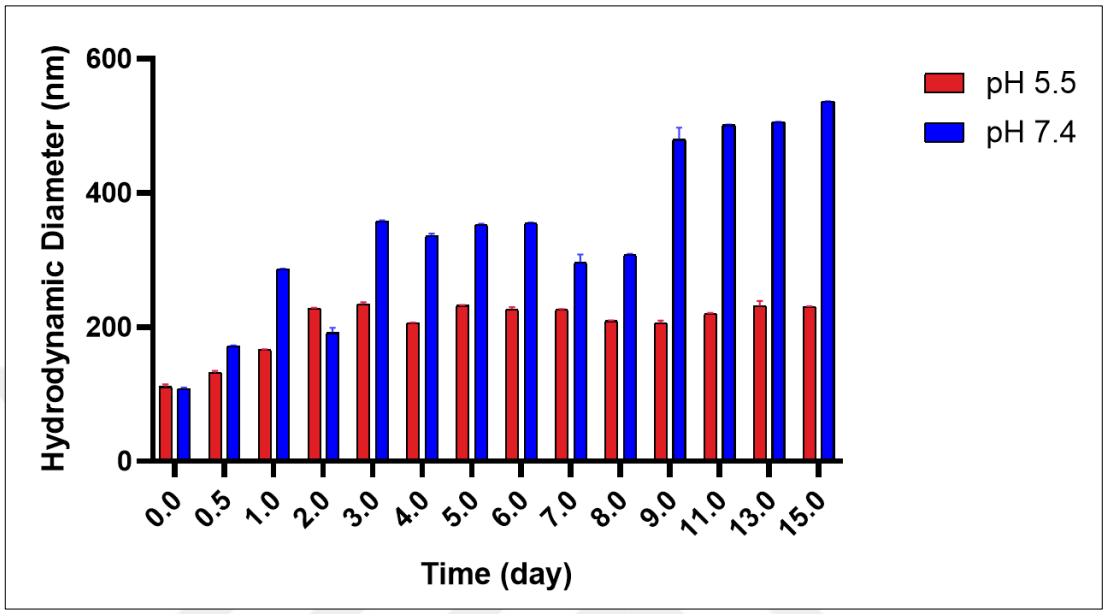

Figure 4.11. Time-dependent stability results of Ch-NPs at two different pH values.

4.1.2 Drug Loaded Polymer and Nanoparticle Preparation (LA-Ch-NPs)

4.1.2.1 Lipoic Acid Conjugated Chitosan Polymer Synthesis

The lipoic acid-conjugated chitosan polymer (α-LA-Ch) was synthesized in four main steps which were described in Section 3.2.2.1. The chemical structure of the material was characterized by FT-IR and ^{1}H-NMR spectroscopy, demonstrating that the amine groups remain free in the side branches and that the lipoic acid drug molecules are linked to the hydroxyl groups by ester bonds.

The characteristic peaks in the structure of α-LA-Ch belonging to both chitosan and the drug, and the ester bond formed between them are shown comparatively in the FT-IR spectrum in Figure 4.13. First of all, it can be seen that the broad band around

3200-3300 cm^{-1} belonging to the groups with 'labile' protons from the chemical structure of the chitosan polymer is also present in the drug-bound polymer. Moreover, amide bonds around 1650 and 1500 cm^{-1} can also be seen in the conjugate. On the other hand, the carboxylic acid carbonyl in the chemical structure of the lipoic acid molecule does not appear in the conjugate spectrum, indicating that no extra drug molecules remain in the medium and are not removed. The comparison is made directly with LA and not LA-Cl in this section because even if LA-Cl molecules remain in the final product, they will return to their original version, LA-carboxylic acid, with water. It can also be seen that the stretching peaks of the -SS- bond in the structure of the drug appear in the conjugate at 722 and 510 cm^{-1}. Therefore, this analysis successfully demonstrated that the final product, LA-CH drug-bonded polymer, actually contains both polymer and drug and that ester bonds can be formed.

Subsequently, 1-H-NMR spectroscopy was also performed for α-LA-Ch conjugate for chemical structure analysis and drug quantification. In the NMR spectrum obtained after the analysis in D_2O in line with the literature, it can be seen that the 'labile' protons belonging to the chitosan polymer appear around 1.32 ppm, and the aliphatic protons adjacent to the electrophilic groups appear as large singlet and multiplet around 3.70 ppm. It was confirmed from the literature that the singlet seen at 0.89 ppm belongs to the $-CH_3$ protons remaining in the structure of chitosan after deacetylation (128). On the other hand, aliphatic protons of the drug molecules appear around 2.5-1.5 ppm, but the proton marked with the letter 'a' in the structure of the drug can be seen at 5.33 ppm as expected as a disulfide neighbor. In addition, the ester peak at 4.22 ppm proves the ester bond between the polymer and the drug molecules, and the amount of drug bound to the polymer was calculated from the integration values of these peaks (1,127). The details of the calculation are as follows: The low molecular weight chitosan polymer with an average molecular weight of 120 kDa divided by the molecular weight of its monomer glucose molecules (180,2 $gmol^{-1}$) yields approximately 600 monomers. Considering that this polymer is 80% deacetylated, 120 monomers were calculated to be acetylated and the integration of the 'g' peak expressing these protons was calculated as 360. The integration of the corresponding ester peak is 366, representing 2 protons in the form of $-CH_2$. This value

is also consistent with the peak integration (183) expressing the ‘a’ proton in the structure of the drug molecule (Fig 4.12).

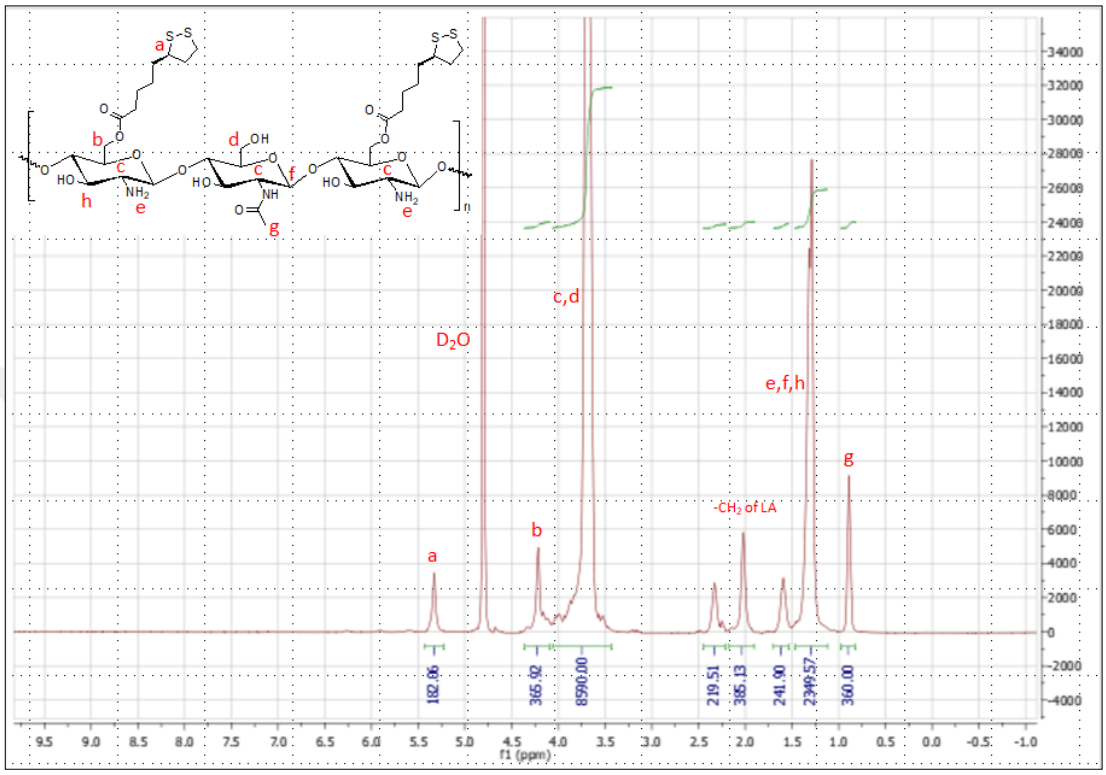

Figure 4.12. ^{1}H-NMR spectrum for lipoic acid conjugated chitosan polymer (α-LA-Ch).

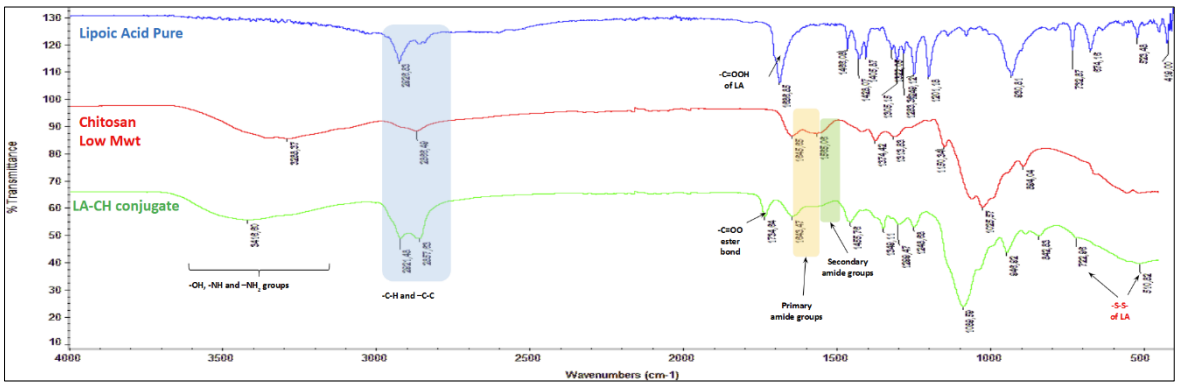

Figure 4.13. Comparative FT-IR spectra for the lipoic acid conjugated chitosan polymer (α-LA-Ch).

4.1.2.2 Preparation of LA-Ch-NPs

The previously optimized method was used to synthesize drug-loaded nanoparticles. Briefly, the drug-loaded chitosan polymer (LA-Ch) was dissolved in 0,01M acetic acid solution at 0,1 wt% (w/v), and 0,01% STPP (w/v) was added at 1:1 or 1:0.5 by volume at RT for 60 minutes and filtered through 0,45 µm Nylon and 0,22 µm PES filters, respectively. According to the results obtained after DLS measurement (Figure 4.14), similar to the Ch-NPs, the 1:1 by volume mixed version of the polymer and crosslinker solutions yielded nanoparticles with target size and low PDI value and demonstrated that the nanoparticle construction procedure optimized in section 3.2.1 was also valid for the LA-Ch-NPs.

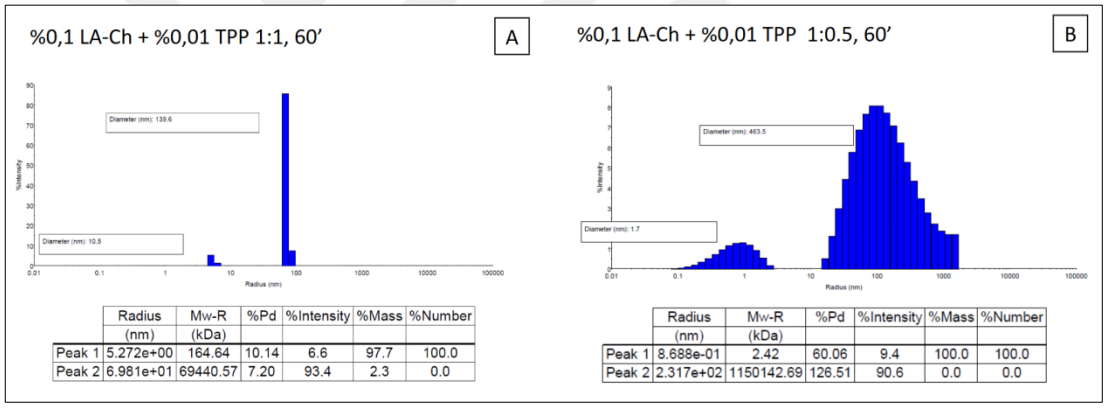

	Radius (nm)	Mw-R (kDa)	%Pd	%Intensity	%Mass	%Number
Peak 1	5.272e+00	164.64	10.14	6.6	97.7	100.0
Peak 2	6.981e+01	69440.57	7.20	93.4	2.3	0.0

	Radius (nm)	Mw-R (kDa)	%Pd	%Intensity	%Mass	%Number
Peak 1	8.688e-01	2.42	60.06	9.4	100.0	100.0
Peak 2	2.317e+02	1150142.69	126.51	90.6	0.0	0.0

Figure 4.14. Effect of the crosslinking concentration to the drug loaded nanoparticle size. Comparison of nanoparticles prepared with 0,1 wt% polymer and 0,01 wt% STPP at 1:0.5 and 1:1 [C]:[T] ratios for 60 min. (A) NP prepared with 0,01 wt% STPP at 1:1 ratio; (B) NP prepared with 0,01 wt.% STPP at 1:0.5 ratio.

Subsequently, a zeta potential measurement was conducted on the drug-loaded nanoparticles. Following three repeated measurements of the nanoparticle solution, diluted 1:10 by volume with 10 mM NaCl solution, it was demonstrated that the nanoparticles have an average surface charge of -10,0 ±6,40 mV. This is considered to be due to the presence of additional electronegative atoms (O and S) resulting from the incorporation of the drug on the surface of the nanoparticles. The reduced surface

charge compared to drug-free nanoparticles suggests that the drug has been integrated into the nanoparticle structure.

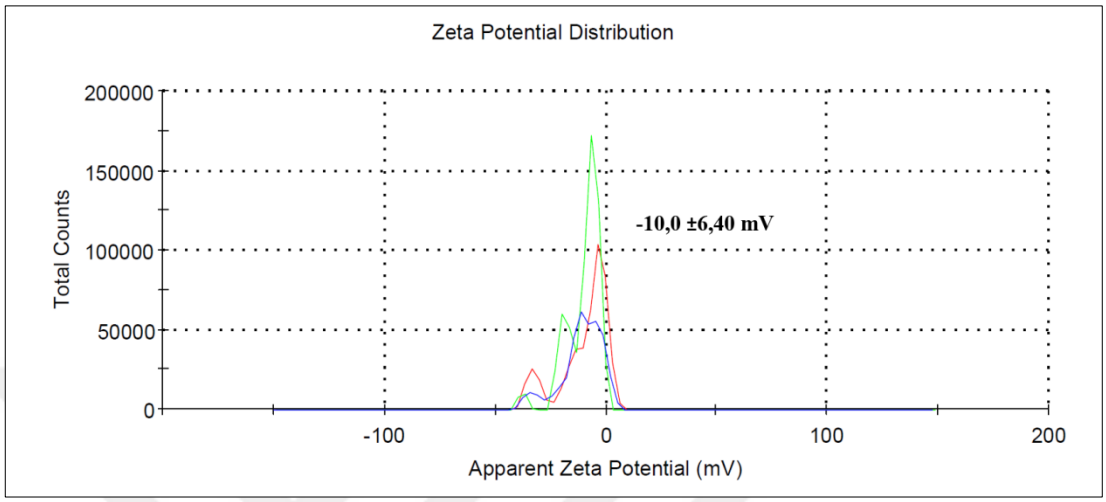

Figure 4.15. Zeta potential measurement of LA-Ch-NPs.

4.1.2.3 Determination of Drug Release Profiles from Drug Loaded Nanoparticles

To determine the amount of drug release profile of LA-Ch-NPs, the LC-MS/MS was used. According to the results shown in Figure 4.16, it was observed that LA-Ch-NPs synthesized to be sensitive to the acidic pH of the neuroinflammation medium showed almost no drug release at pH 7.4 (green line) mimicking the healthy body environment, whereas at pH 5.5 (red line) mimicking the inflammation medium, the NPs released the drug slowly and in a sustained manner for almost 2 weeks. At the same time, when esterase enzyme was added to the media (blue and black lines), NPs were observed to release the drug rapidly. Thus, this demonstrates that the ester bonds in the LA-Ch polymer used to synthesize NPs are sensitive to the esterase enzyme.

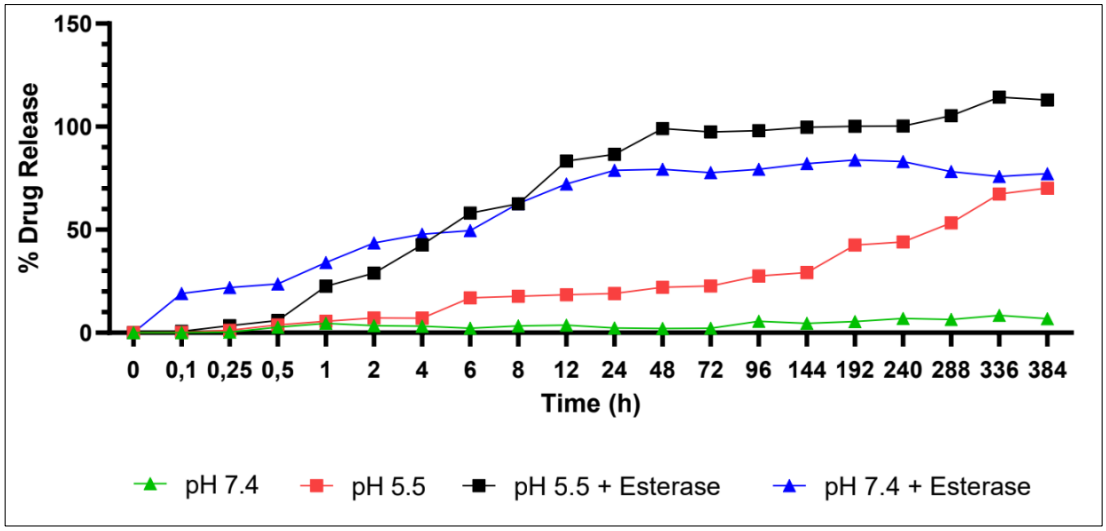

Figure 4.16. Time dependent drug-release profile of LA-Ch-NPs after incuation in pH 7.4 PBS, pH 5.5 AB, pH 5.5 AB + esterase, and pH 7.4 PBS + esterase for 30 days.

4.1.3 Preparation of the Flourescent Dye Conjugated Nanoparticles (Cy3-Ch-NPs)

Cy3 fluorescent dye was conjugated to the surface of Ch-NPs. Subsequently, Cy3 fluorescent dye bound nanoparticles (Cy3-Ch-NPs) were physically characterized (SEM and TEM). Furthermore, the amount of Cy3 fluorescent dye bound to the nanoparticle surface was quantitatively measured by NanoDrop and Varioskan instruments.According to the data in Table 4.4 and Figure 4.17, it can be seen that the size of the nanoparticles centrifuged using Amicon filter decreased with the conjugation of the dye, but the PDI value remained almost the same.

Table 4.4. Size details for imaging agent conjugated nanoparticle (Cy3-Ch-NP). Effect of dye conjugation on the size of nanoparticles containing 0.1% chitosan, 0.01% STPP, prepared with 1:1 [C]:[T] ratio and passed through 1 time Nylon and 1 time PES filter for 60 minutes.

Nanoparticle	Radius (nm)	PDI (%)	Intensity (%)
Ch-NP	107.6	10.49	95
Cy3-Ch-NP	155.4	14.83	97

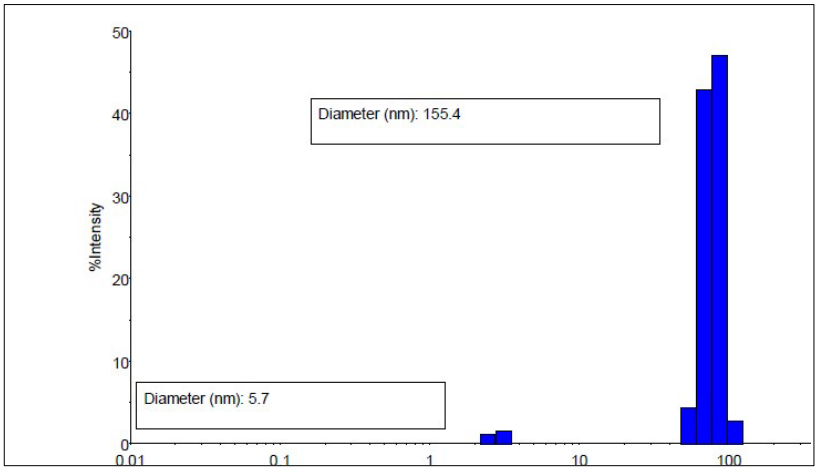

Figure 4.17. Cy3 conjugated NP (Cy3-Ch-NP) ultra-filtered using Amicon filters with Mwt cut-off: 100 kDa for 3 min at 2500 rpm, centrifuged 3 times with ddH_2O.

Two different instruments were used in order to calculate how much dye was on the prepared Cy3-Ch-NPs. The first one is the NanoDrop spectrophotometer, which is based on absorbance value measurement; the other one is Varioskan, which uses the fluorescence property of the molecule. The Cy3 dye has an emission wavelength of 570 nm and an excitation wavelength of 555 nm. Standard samples for both instruments were prepared by making 50% (i.e. 1:1) dilutions with PBS (10 mM, pH: 7.4) from the prepared stock dye solution. (Figure 8.2 & 8.3 in the Appendices). The standard curves obtained after the measurements of the prepared calibration samples at appropriate wavelengths in these two different instruments are given in the appendices. According to these curves with high R^2 values, the purified dye-conjugated nanoparticles were measured and according to the results obtained, 86,4% of the 15 µg of dye molecules participating in the reaction were successfully conjugated to the nanoparticles via Varioskan measurement and 89.5% via Nanodrop measurement.

The surface charge measurement (zeta potential) of the prepared Cy3-Ch-NPs was performed with the LitesizerTM 500 device. In this analysis, similar to the others, the nanoparticle solution was diluted 1:10 by volume with 10 mM NaCl, the electrolyte solution, and the measurements were taken in triplicate. According to the analysis, the

surface charge of Cy3-Ch-NPs was found -31,1 ±6,14 mV (Fig. 4.18). This negative value proves that this dye molecule binds to the amine groups on the surface of the nanoparticle.

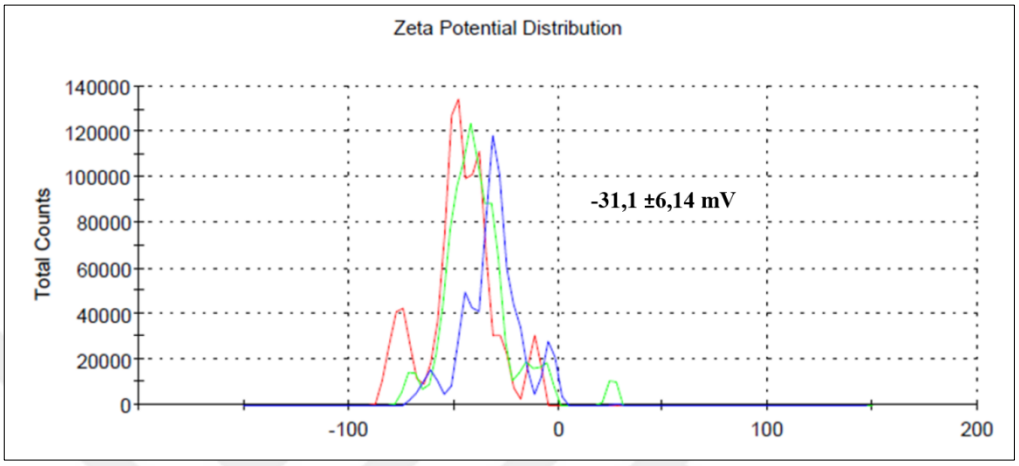

Figure 4.18. Zeta potential measurement of Cy3-Ch-NPs.

Moreover, the SEM and TEM analyses demonstrated that the nanoparticles retained their spherical morphology even after the conjugation of dye molecules. As shown in Figure 4.19, although the nanoparticles exhibited a round shape, they had a smaller size compared to the DLS result, which was expected due to the high vacuum conditions during the analyses.

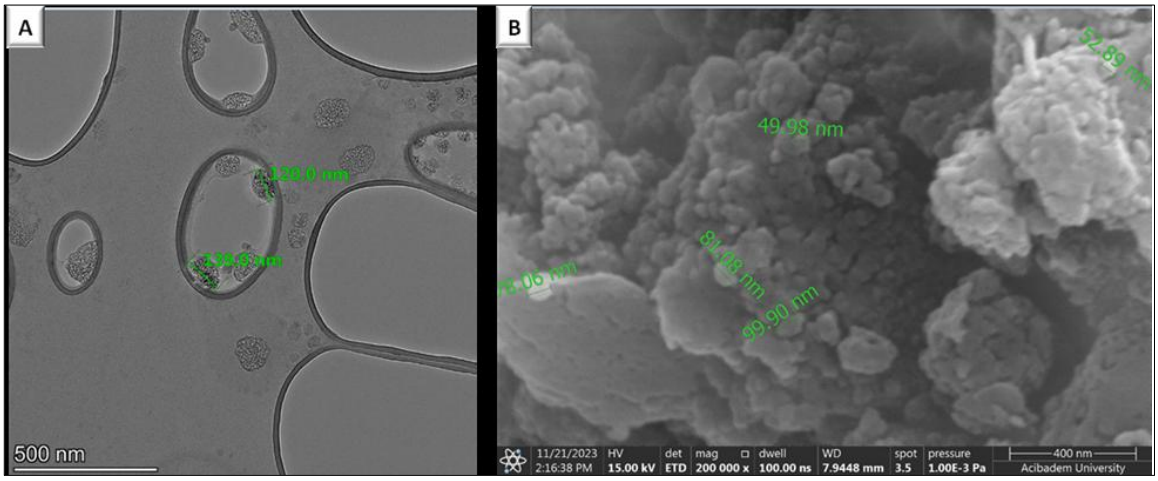

Figure 4.19. Morphological analysis results of Cy3-Ch-NPs. (A) TEM microgpraph, (B) SEM micrograph.

4.1.4 Preparation of Targeted Nanoparticles

4.1.4.1 Synthesis and Characterization of T7 Peptide

The HAIYPRH (T7) peptide was synthesized using the solid phase peptide synthesis method mentioned in the previous sections and then characterized by LC-MS/MS, HPLC, and ^{1}H-NMR.

1 mg of the obtained peptide was dissolved in 500 µL acetonitrile (ACN) and 500 µL distilled water and HPLC analysis was performes to confirm the purity. Analysis with mobile phase (50% ACN & 50% ddH_2O) pass through at a rate of 0,5 mg/mL on a C18 stationary phase column showed that the peptide obtained was 83.6% pure (Figure 4.20).

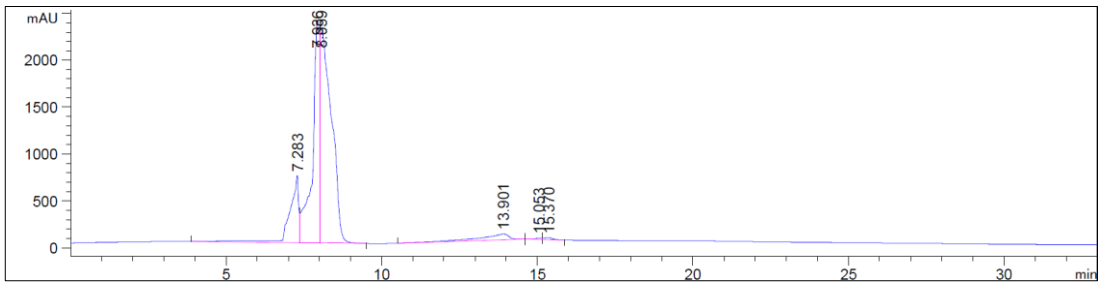

Figure 4.20. HPLC chromotogram of T7 peptide.

Moreover, the LC-MS/MS analysis of 20 µL of the same sample was performed by mass analysis considering the theoretical molecular weight and degree of ionisation of the peptide. The spectrum shown in Figure 4.21 was obtained as a result of the analysis on a C18 column, and 0,05% (by volume) Formic acid (FA) was added to the

same mobile phase mixture. Thus, ionisation of the peptide molecules was detected. The analysis was performed using MS2Scan scanning method for both negative and positive region and it can be seen that the signals on the y-axis are around 104-105 and have high intensity. When the chemical structure of T7 peptide is analysed, it is seen that 1 arginine amino acid is already positively charged. However, it is also seen that there are 1 tyrosine and 2 histidine amino acids which can be protone or deprotone according to the pH value of the environment. Considering that peaks were detected according to m/z values in LC-MS/MS analysis, it can be easily seen that there are peaks belonging to 3, 4 and 5 charged ion versions in both negative and positive regions. Additionally, peaks corresponding to the sodium (Na^+) retained versions of the formed peptide ions were also observed in the spectrum. Based on this result, it is confirmed that the pure material obtained belongs to the T7 peptide structure.

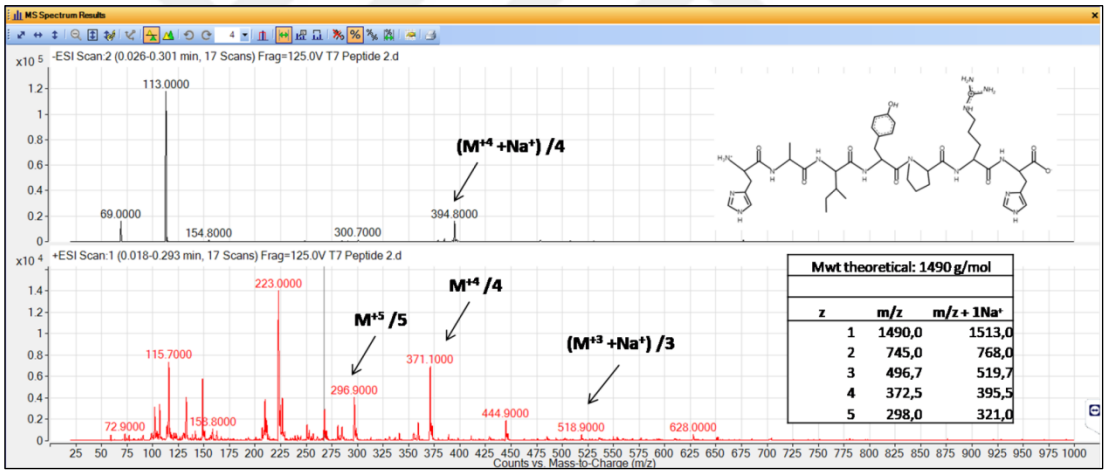

Figure 4.21. LC-MS/MS chromatograms of T7 peptide.

^{1}H-NMR and FT-IR spectroscopy results of the T7 peptide are shown in Figures 4.22 and 4.23. Due to the solubility of the T7 peptide, proton NMR in DMSO-d_6 showed that aromatic and labile protons from the chemical structure of the peptide appeared in the range of 7-9 ppm. On the other hand, peaks belonging to -CH_2 on the amide carbonyl side of the peptide can be seen at 4.16 ppm. In addition, the characteristic functional groups belonging to the chemical structure of the T7 peptide are also observed in the FT-IR spectrum. The primary and secondary amide carbonyl

stretching bonds are seen at 1649 and 1538 cm^{-1}, respectively; the peaks belonging to -C-N bonds seen around 1200 cm^{-1}, and the fingerprint aromatic bending peaks seen in the range 836-720 cm^{-1} prove that a peptide sequence with the correct chemical structure has been obtained.

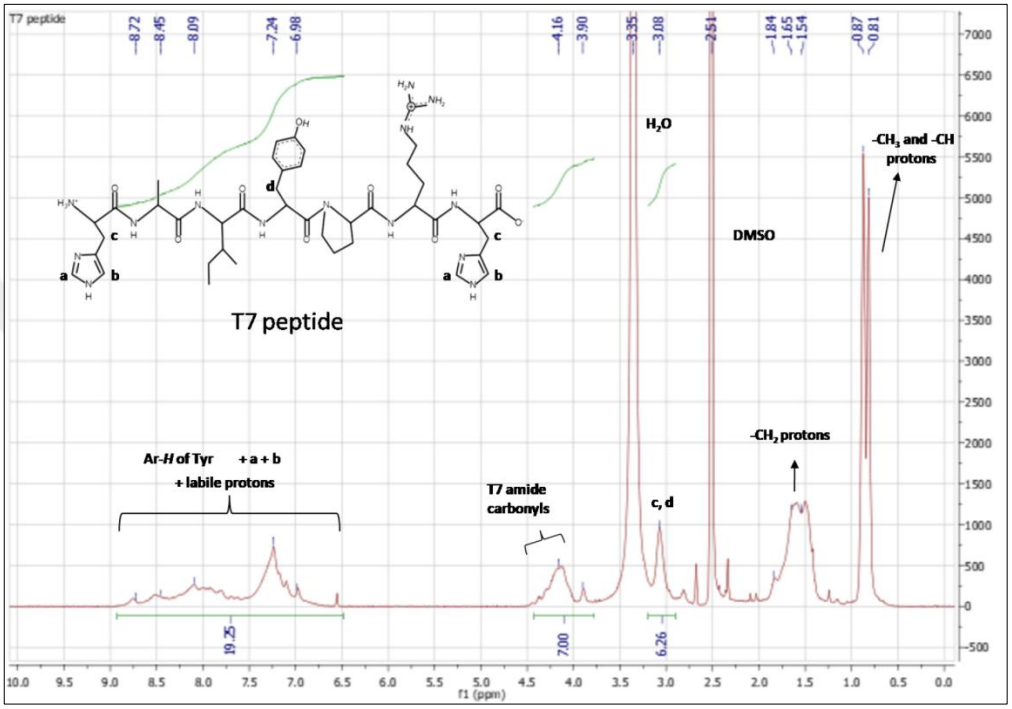

Figure 4.22. ^{1}H-NMR spectrum for T7 peptide (in DMSO-d_6).

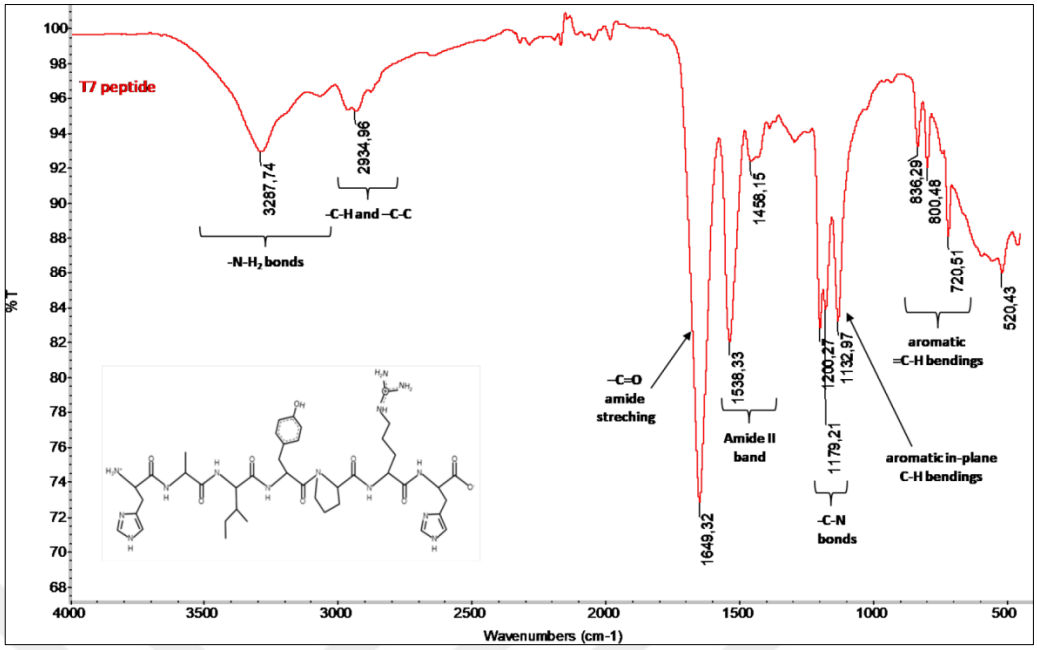

Figure 4.23. FT-IR spectrum of the T7 peptide.

4.1.4.2 Synthesis and Characterization of PEG Conjugated T7 Polymer

In order to bind the synthesized T7 peptide on the nanoparticle, firstly, the PEG chain to be placed between these peptide molecules and the nanoparticle must be attached to the peptide. Therefore, a hetero-functionalized PEG chain (Mwt: 2000 $gmol^{-1}$) with a free primary amine ($-NH_2$) group at one end and a free thiol (-SH) group at the other end was used (129). The ultimate goal was to add the T7 peptide to the aminated end of this PEG chain and an NHS-activated carboxylic acid group containing a disulfide group to the other thiolated end. The NHS ester end of this T7-PEG conjugate was aimed to bind to the free amine groups on the surface of the Ch-NPs by forming amide bonds. Thus, the T7 peptide at the other end of this conjugate bound to the surface of the nanoparticles is designed to remain on the surface (towards the outer aqueous environment) and be the first component to communicate with the barrier to pass the total nanoparticle system through the blood-brain barrier (BBB).

In addition, the disulfide (S-S) bond in the structure of this synthesized conjugate was planned to be located at the end of the PEG chain that will bind to the nanoparticle so that when the total nanoparticle enters the brain tissue and reaches to the inflammation site, this PEGylated peptide conjugate will be cleaved from the surface of the nanoparticles by disulfide exchange reaction, releasing the drug-loaded nanoparticle. Hence, obtaining this redox-sensitive peptide conjugate is considered as one of the most important and meaningful objectives of this thesis project. The nanoparticles in this project are referred to as "peelable" as it is expected that the T7-PEG conjugate on their surface can detach in an inflammatory environment, enabling targeted release after crossing into the brain.

The synthesis steps of the T7-PEG-$_{S-S}$-NHS descirbed in the Figure 3.4. In the first step of synthesizing T7-PEG-$_{S-S}$-NHS polymer, the T7-PEG-PDS obtained as 52 mg, corresponding to an 81,2% yield (theoretical yield: 62,8 mg). In the last step, after drying the purified solid conjugate (T7-PEG-ss-NHS, Mwt = 3096,2 g/mol) in a desiccator, the obtained amount was measured as 46,7 mg, corresponding to an 80,4% yield.

To characterize the obtained peptide conjugated polymer, firstly, purity control analysis was performed by HPLC for the heterofunctional polymer Amine-PEG-Thiol used as a starting material (4.24). The analysis shows that this conjugate, which peaks at a low retention time due to its hydrophilic structure, has a purity of 99.3%. The presence of characteristic peaks for the chemical structure can also be seen in the FT-IR spectrum in Figure 4.25. The presence of the peak at 1106 cm^{-1} representing the -C-O bonds of PEG, as well as the -S-H stretching (2650 cm^{-1}) and -C-SH bending (841 cm^{-1}) peaks from the thiol group and the -N-H bending at 1627 cm^{-1} and -C-N stretching peaks at 1279 cm^{-1} from the amine group indicate that we used the heterofunctional polymer with the correct structure.

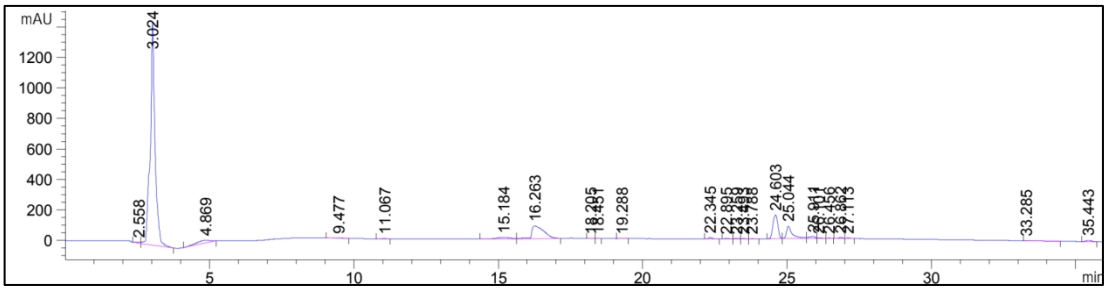

Figure 4.24. HPLC chromotogram of the Amine-PEG-Thiol conjugate.

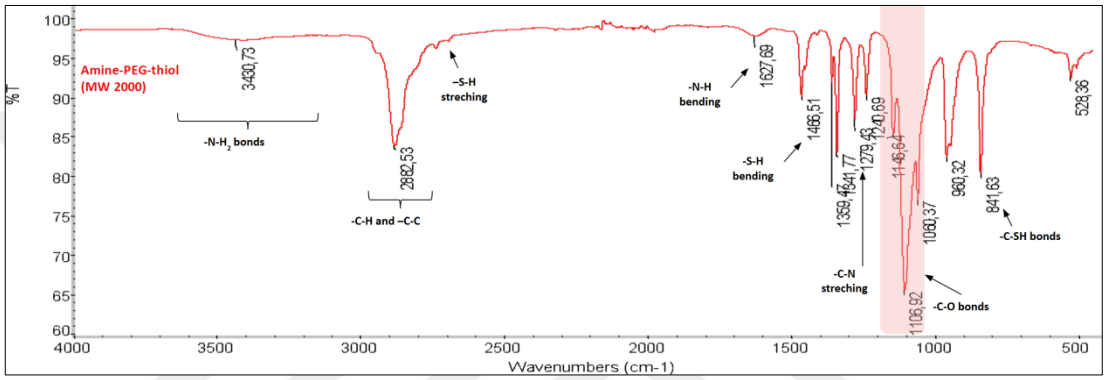

Figure 4.25. FT-IR spectrum of the Amine-PEG-Thiol conjugate.

After the chemical structure characterization of the starting material, the purity of the synthesized T7-PEG-ss-NHS conjugate was also controlled using HPLC. Likewise, this conjugate, which has a hydrophilic structure due to the PEG chain, was observed to leave the column at low retention time and was calculated to be 95,8% pure (Fig. 4.26).

Moreover, the chemical structure of this conjugate was investigated by both 1H-NMR and FT-IR spectroscopy methods. There are mainly 3 components in the structure of the conjugate: T7 peptide, PEG polymer, and NHS ester group. From the FT-IR spectrum in Figure 4.27, it is noteworthy that the -C-O bonds from the PEG structure are also seen at 1106 cm^{-1}, indicating that we have a PEG-based material. On the other hand, labile protons (-N-H) from the T7 peptide structure appear at 3328 cm^{-1}, primary amide carbonyl bonds at 1657 cm^{-1}, secondary amide carbonyl bonds at

1561-1343 cm-1 and bending peaks of aromatic groups at 840-765 cm^{-1}. The presence of the stretching peaks of the NHS ester group at the other end of the conjugate at 1758 (symmetric) and 1711 (asymmetric) cm-1 proves the presence of the NHS ring. In addition, the -C-N-C- bond of this ring is also indicated by the peak at 1200.99 cm^{-1}(130). Finally, the presence of the -S-S- bond on the NHS side can also be understood by the stretching peaks of the -C-S bond at 719 cm^{-1} and the -S-S disulfide bond at 655 cm^{-1}. These peaks reveal the conjugate preparation with the desired functional groups and components.

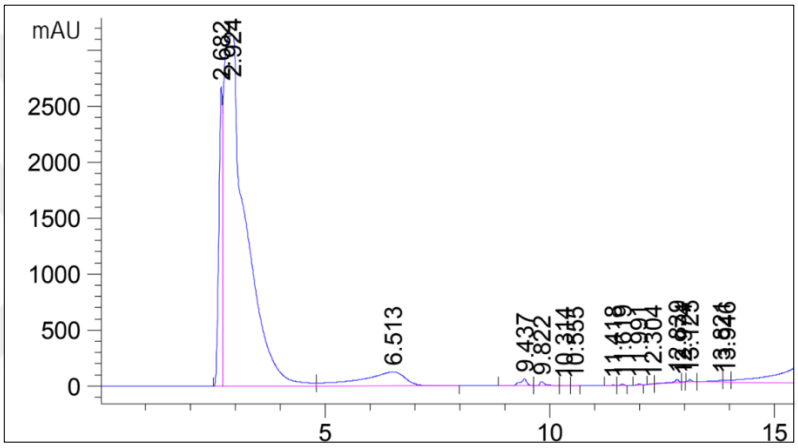

Figure 4.26. HPLC chromotogram of the T7-PEG-ss-NHS.

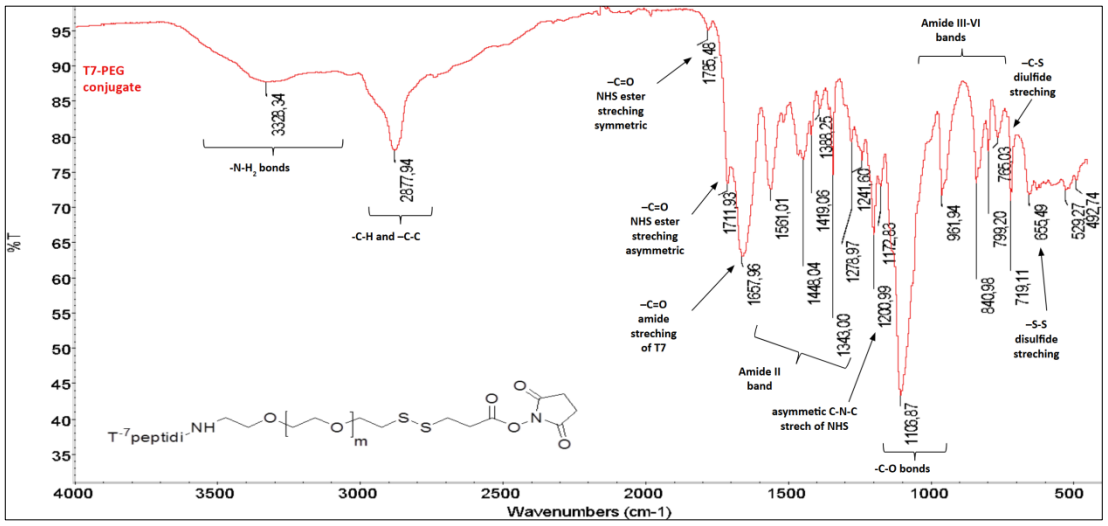

Figure 4.27. FT-IR spectrum of the T7-PEG-ss-NHS.

The ^{1}H-NMR spectrum of the synthesized T7-PEG-ss-NHS conjugate in deuterated chloroform ($CDCl_3$) in Figure 41 demonstrates the presence of both peptide, polymer, and NHS group in the structure. It is observed that aromatic and labile protons from the structure of the T7 peptide appear in the range of 7.5-8.8 ppm. Although there are overlap peaks, it is possible to see aromatic tyrosine (8.11-8.02 ppm) and histidine double bonds (8.83 and 7.68 ppm) in the structure of the peptide. The amide carbonyl -CH_2 peaks between 4.00 and 3.79 also come from the T7 structure. The broad peak at 3.66 ppm indicates -O-CH_2 protons in the PEG structure.

On the other hand, the presence of the NHS group is evident from the peak of NHS-ester -CH_2 protons at 4.08 ppm and the peak of -C=OCH_2 protons in its ring at 2.97 ppm. Furthermore, the integral values of the peaks belonging to the T7 peptide and the NHS group indicate that they are one in the conjugate structure. Finally, the triplet seen at 3.45 ppm comes from the -CH_2 protons next to the S-S disulfide bond, confirming the presence of this group in the structure.

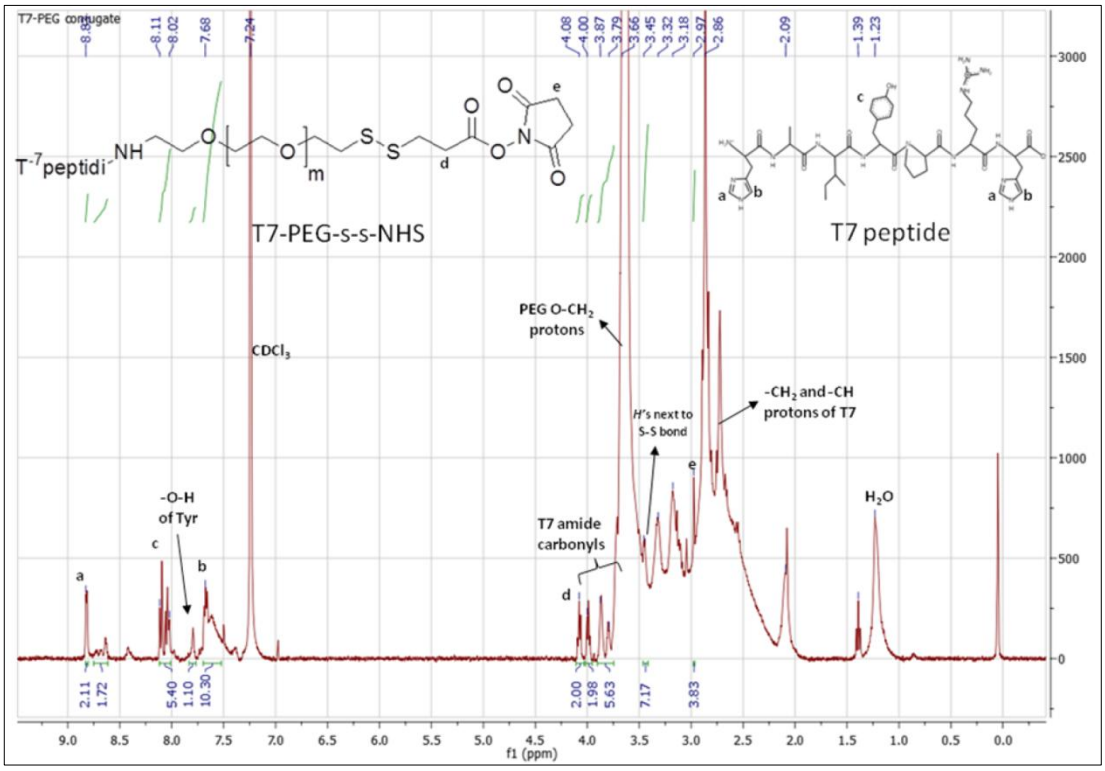

Figure 4.28. ^{1}H-NMR spectrum for T7-PEG-ss-NHS (in $CDCl_3$).

4.1.4.3 Preparation of Flourescent Labeled Microglia Targeted Nanoparticles (Cy3-CD11b-Ch-NPs)

Cy3-CD11b-Ch-NPs, which were obtained by conjugating CD11b antibody to the surface of nanoparticles in a ratio of [Antibody]:[EDCI/NHS] 1:10, were purified by centrifugation 17 times against distilled water (ddH2O) for 3 minutes at 2500 rpm using Amicon ultracentrifuge filters (Mwt cut-off: 100 kDa) to remove unbound molecules after synthesis. Afterwards, it was kept in a sonicator for 10 minutes and DLS measurement of the obtained solution was taken. Additionally, the solution was filtered again using a 0,22 µm PES syringe filter to get rid of oversized aggregates and then DLS measurement was taken again (Fig. 4.29). According to the DLS result obtained, it was observed that both the PDI value and the size of the nanoparticles filtered through the PES filter again after centrifugation using the Amicon filter decreased and were obtained in the desired range (155.6 nm).

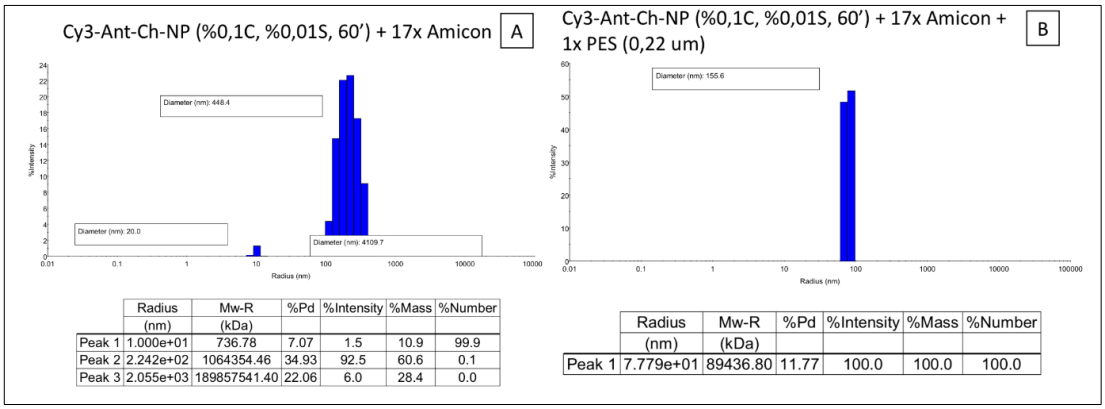

	Radius (nm)	Mw-R (kDa)	%Pd	%Intensity	%Mass	%Number
Peak 1	1.000e+01	736.78	7.07	1.5	10.9	99.9
Peak 2	2.242e+02	1064354.46	34.93	92.5	60.6	0.1
Peak 3	2.055e+03	189857541.40	22.06	6.0	28.4	0.0

	Radius (nm)	Mw-R (kDa)	%Pd	%Intensity	%Mass	%Number
Peak 1	7.779e+01	89436.80	11.77	100.0	100.0	100.0

Figure 4.29. Effect of filtration on the preparation of flourescent labeled microglia targeted nanoparticles (Cy3-CD11b-Ch-NPs). (A) Cy3-CD11b-Ch-NPsultrafiltered by centrifugation with ddH2O 17 times using Amicon filters (Mwt cut-off: 100 kDa) for 3 min at 2500 rpm. (B) Cy3-CD11b-Ch-NPsultrafiltrated by centrifugation with ddH2O 17 times using Amicon filters (Mwt cut-off: 100 kDa) for 3 min at 2500 rpm followed by filtration through a PES (0,22 µm) syringe filter.

Following the size measurement, surface charge measurements of the antibody conjugated nanoparticles obtained in the appropriate size range were also performed, and the result obtained is given in Figure 4.30. Section 4.1.3 measured the surface charge of Cy3-Ch-NPs as -31,1 mV. After the CD11b antibody molecules were attached to the surface of these nanoparticles, the surface charge of the Cy3-CD11b-Ch-NPs obtained increased to 19,6 ±5,12 mV. This zeta potential measurement, representing the surface charge, indicates that the antibody protein was successfully attached to the surface of the nanoparticles.

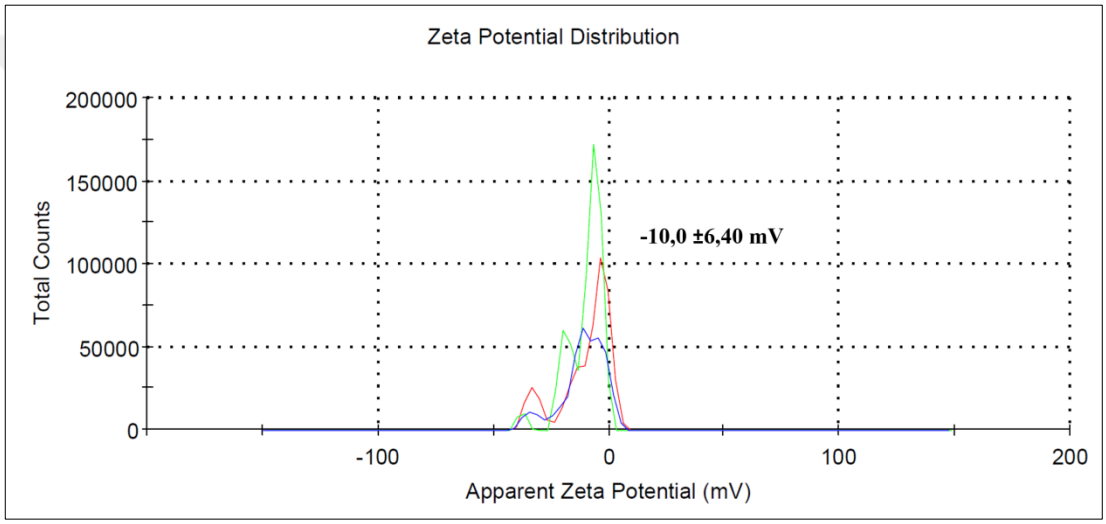

Figure 4.30. Zeta potential measurement of Cy3-Ant-Ch-NPs.

The morphological structure of the nanoparticles was characterized using SEM and TEM microscopes. As seen in Figure 4.31, after antibody molecules were attached to the surface of the nanoparticles, they maintained their spherical shape and size range consistent with the DLS result.

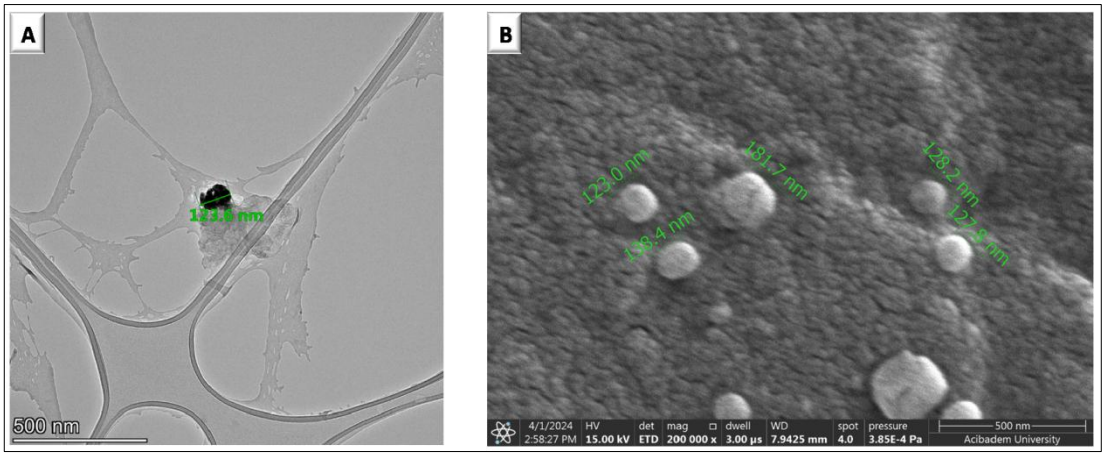

Figure 4.31. Morphological analysis results of Cy3-CD11b-Ch-NPs. (A) TEM microgpraph, (B) SEM micrograph.

The BCA protein quantification method was used to calculate the amount of antibody attached to the surface of Cy3-CD11b-Ch-NPs. Standards in the range of 2-50 µg/mL were prepared according to the kit's own procedure and a standard calibration curve was obtained (Calibration curve is given in the Appendix).

For the measurement of the samples, BCA solution was added to the samples as indicated in the kit, incubated at 37°C for 30 minutes and then measured at 562 nm on a plate reader. Using the prepared calibration curve, the antibody bound nanoparticles were measured and the antibody concentration in the Cy3-CD11b-Ch-NP solution was calculated to be 175 ng/mL. In total, 4mL of this solution contained 700 ng of antibody, which was calculated to be 14% of the 50 µg of antibody initially added to the medium. It can be understood that the yield achieved was relatively low due to the large antibody structure and the small amount of antibody used at the beginning of the reaction compared to the amine groups in chitosan, but since PEGylated T7 peptide will be attached to these nanoparticles in the next steps, excessive antibody binding was avoided, and the yield achieved was determined to be sufficient.

4.1.4.4 Preparation of Brain and Microglia Targeted (Dual Targeted) Nanoparticles (CD11b-T7- LA-Ch-NPs)

The dual-targeted nanoparticles, which were obtained by first T7-PEG-ss-NHS conjugated to pre-prepared LA-Ch-NPs, and subsequently, CD11b antibody attached to T7 conjugated nanoparticles (CD11b-T7- LA-Ch-NPs) prepared to obtain dual targeted nanoparticles, as given in Section 3.2.4.4.

Following the synthesis, obtained CD11b-T7- LA-Ch-NPs were ultrafiltered 3 times against ddH2O using an Amicon ultracentrifuge filter to remove excessive amounts of solvent and unbound molecules. After centrifugation, nanoparticles were again filtered using a 0,22 µm PES filter to eliminate large aggregates, and DLS measurement of the obtained solution was taken. According to the DLS result, nanoparticles with a target size and low PDI value (152.0, and 11.89%, respectively) were successfully synthesized.

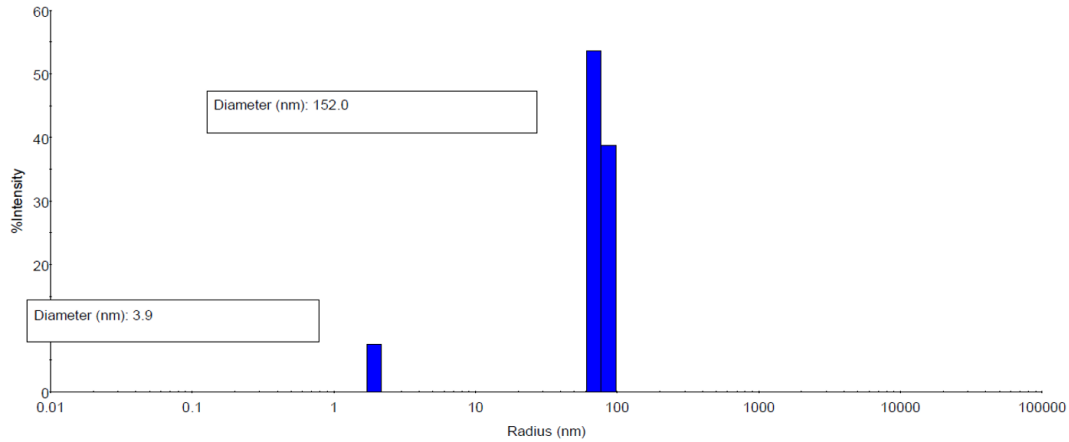

	Radius (nm)	Mw-R (kDa)	%Pd	%Intensity	%Mass	%Number
Peak 1	1.936e+00	15.79	0.00	7.6	99.9	100.0
Peak 2	7.600e+01	84705.55	11.89	92.4	0.1	0.0

Figure 4.32. Dual-targeted nanoparticles CD11b-T7- LA-Ch-NPs ultra-filtered using Amicon filters with Mwt cut-off: 100 kDa at 2500 rpm, centrifuged 3 times with ddH_2O.

Following the size measurement, surface charge measurements of dual-targeted nanoparticles obtained in the appropriate size were also performed, and the result obtained is given in Figure 4.33. In comparison to the other nanoparticles, the surface charge of the CD11b-T7- LA-Ch-NPs obtained decreased to -27,7 ±6,96 mV. This zeta potential measurement, which represents the surface charge, indicates that all the modification elements (drug encapsulation, T7 peptide and anti-CD11b antibody conjugation) were successfully attached to the surface of the nanoparticles.

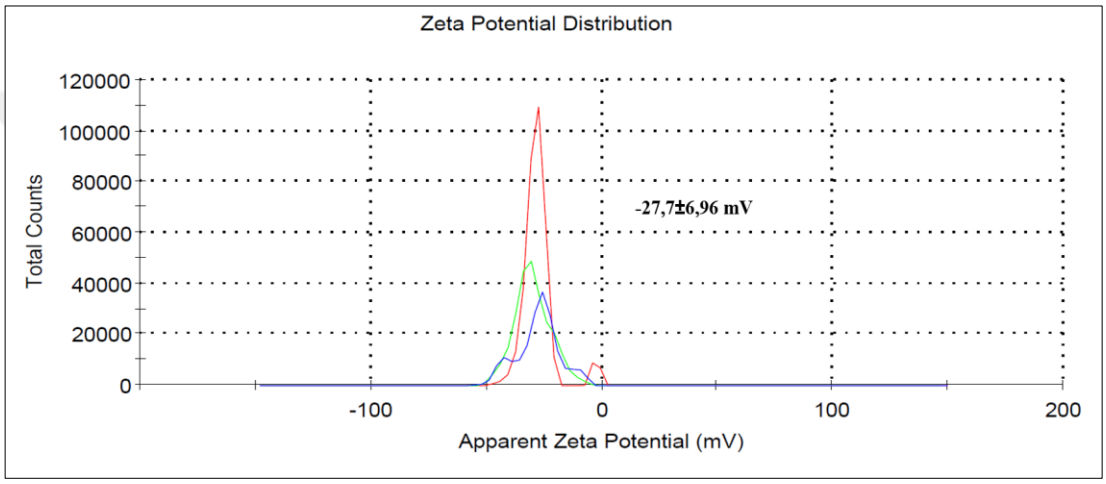

Figure 4.33. Zeta potential measurement of CD11b-T7- LA-Ch-NPs.

In order to demonstrate the "peelability" of the T7-PEG peptide conjugate, a "peelability" experiment was performed with T7-PEG conjugated nanoparticles as detailed in Section 3.2.4.4. According to the results of this 60-minute experiment in which Ch-NPs were used as a control group, as shown in the graph in Figure 4.34, when the size of the nanoparticles reacted at a concentration of 0.2 mM was examined, it was observed that the T7-PEG-S-S-NHS in the shell was “peeled-off” at 30 and 50 minutes and the nanoparticles reached the size of their unmodified state.

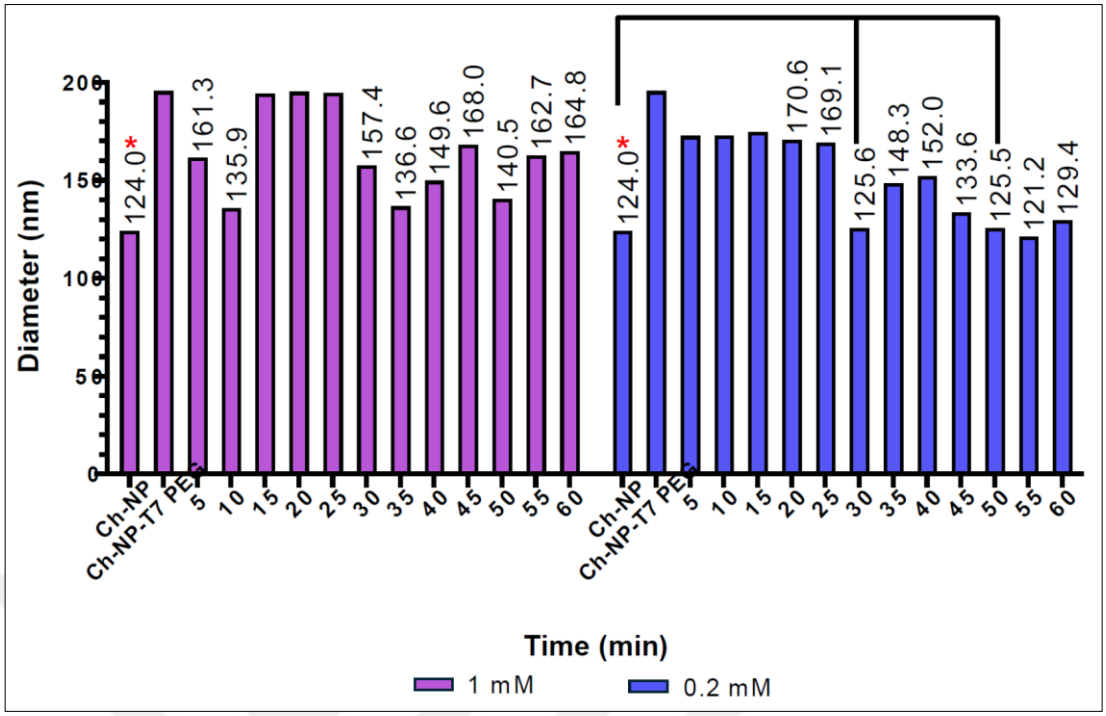

Figure 4.34. Time-dependent peel-off test results of T7-PEG conjugated nanoparticles with Glutathione-SH.

4.2 In Vitro Experiments

4.2.1 In Vitro Cytotoxicity Assay (CCK-8)

In vitro cytotoxicty evaluation of the prepared empty and drug-loaded nanoparticles (Ch-NPs and LA-Ch-NPs) and peptide-conjugate and free drug molecules (LA and T7-PEG-ss-NHS) were performed using the CCK-8 assay kit for the Mouse microglial EOC-20 (*ATCC CRL-2469*) and Mouse skin fibroblast L929 (*ATCC CCL-1*) cell lines.

Figure 4.35 demonstrates that empty chitosan nanoparticles (Ch-NPs) formed by physical cross-linking of chitosan chains with STPP crosslinker showed no cytotoxicity at all.

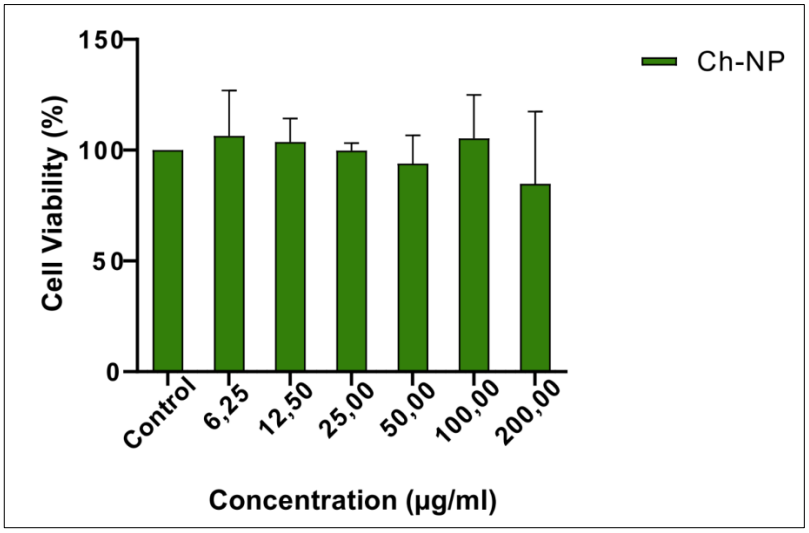

Figure 4.35. Cytotoxicity based on cell viability vs. dose graph for Ch-NPs, n = 3.

On the other hand, the T7-PEG conjugate synthesized to attach to the nanoparticles showed cytotoxicity depending on the dose. While the cell viability was around 100% between 6,25 µg/mL and 25 µg/mL,more than 25 µg/mL of the conjugate decreased cell viability in a dose-dependent manner, as shown in Figure 4.36.

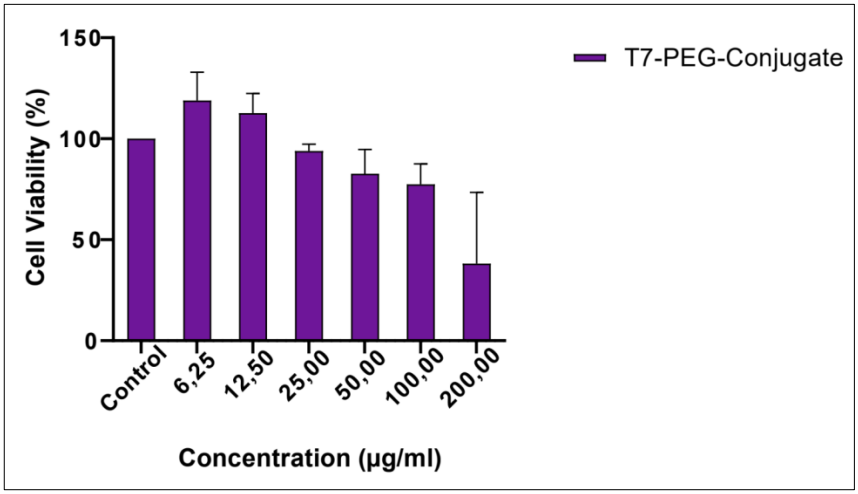

Figure 4.36. Cytotoxicity based on cell viability vs. dose graph for T7-PEG-ss-NHS, n = 3.

Moreover, as shown in the graph in Figure 4.37, free drug molecules did not exhibit toxic effects, which is also supported by studies in the literature (131). In

contrast, drug-loaded nanoparticles, synthesized through optimization based on previously obtained results, demonstrated dose-dependent toxicity on microglial cells. In this context, no toxic effects were observed at concentrations of 175 µM and below, whereas the highest applied dose of 350 µM resulted in a significant decrease in cell viability (132).

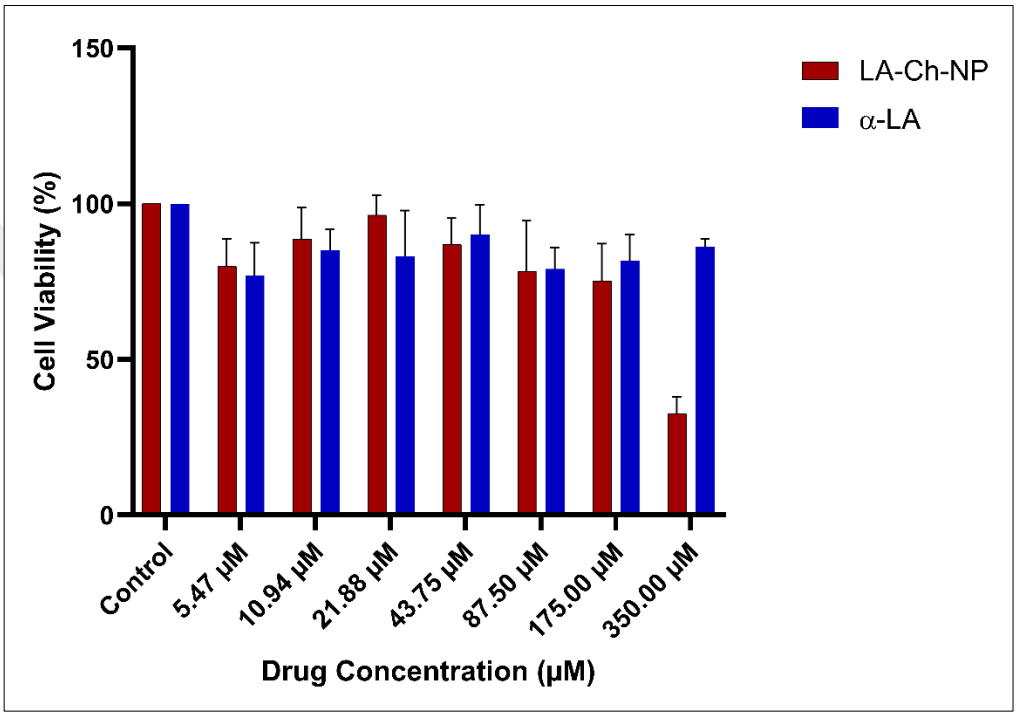

Figure 4.37. Cytotoxicity based on cell viability vs. drug concentration (µM) graph for LA-Ch-NPs and α-Lipoic Acid, n = 3.

5. DISCUSSION

In cases such as accidents and strokes, the activation of protective microglia and astrocytes which protect neurons and ensure their myelination due to inflammation that may occur in the brain tissue and subsequent nerve cell death are very common and rapid conditions (100,103). In order to reduce the severity of this condition and to prevent permanent damage to brain tissue, rapid delivery and effective penetration of anti-inflammatory/anti-oxidant drugs into brain tissue is critical. Due to the highly selective blood-brain barrier (BBB), the penetration of small drug molecules into the brain and their accumulation in damaged tissue is very limited (101,133). This thesis focuses on the development of a dual-targeted and peelable drug delivery system that can enable active drug molecules to cross this barrier to recover damaged nerve cells. The nanoparticles designed in this project contain T7 peptide to facilitate the passage thrugh the BBB and anti-CD11b antibody targeted to active macroglia. It is designed to release anti-oxidant drug (α-lipoic acid) molecules that also shows anti-inflammatory effect in order to act against neuro-inflammation.

First of all, a variety of nanoparticle formulations were prepared by changing the molecular weight and/or concentration of the polymer, polymer/crosslinker [C]:[T] ratio, solvent amount, reaction time, and filtering method parameters in order to find an optimum procedure for the synthesis of nanoparticles as given in Section 4.1.1.

For the optimization of the polymer molecular weight, the results demonstrate that low molecular weight chitosan (50-190 kDa) produced smaller and more homogeneous nanoparticles compared to medium molecular weight chitosan (200-310 kDa). The increased size and PDI of nanoparticles synthesized with medium molecular weight chitosan can be attributed to insufficient crosslinking, leading to polymer chain folding and aggregation, which aligns with previous reports in the literature indicating that molecular weight strongly influences nanoparticle size and stability (134).

Following the optimization of molecular weight, the effect of the reaction time and filtration process were investigated. Reaction time optimization shows that 60 minutes was the ideal duration to achieve nanoparticles with a stable size and low PDI. While 15-minute and 30-minute reactions yielded nanoparticles of similar characteristics, longer reaction times, particularly 120 minutes, resulted in particle aggregation and precipitation, rendering them unsuitable for further applications (Fig. 4.3). Filtration with 0.45 μm Nylon and 0.22 μm PES filters was necessary to remove oversized aggregates and achieve more uniform nanoparticles in the solution (Table 4.1 & 4.2). However, excessive filtration steps beyond two rounds led to micron-sized particle formation, probably due to mechanical stress-induced aggregation.

The influence of polymer and crosslinker concentrations on nanoparticle formation was also studied. The results showed that nanoparticles prepared with a 1:1 polymer-to-crosslinker ([C]:[T]) ratio had a more homogeneous size distribution and lower PDI than those with a 1:0.5 ratio (Fig. 4.6). Furthermore, reducing the STPP concentration to 0.01 wt% resulted in nanoparticles with smaller sizes and lower PDI values compared to 0.05 wt% and 0.1 wt% STPP formulations, suggesting that lower crosslinker concentrations promote tighter network formation without excessive aggregation.

Considering all the results obtained, an optimized procedure for the main NP structure was determined as follows: Reaction at RT for 60 min using 0.1% low molecular weight Chitosan and 0.01% STPP in a 1:1 ratio followed by filtration with 1 time (0.45 μm) Nylon and 1 time (0.22 μm) PES filter. The hydrodynamic diameter of empty Ch-NPs were found as 107.6 nm.

The stability of the Ch-NPs was also investigated, and the results demonstrated that Ch-NPs exhibited a size increase to approximately 200 nm in the first 3-4 days in an acidic medium, indicating that the nanoparticle swelled but remained almost intact. It was also observed that the swelling is higher in a neutral medium, and the

nanoparticles exceed 300 nm in size from the first week. These two trends indicate that when the prepared chitosan-based nanoparticles are introduced into the bloodstream, they have a high chance to rapidly increase in size and lose stability if they remain in circulation for a long time, which indicates that targeting the nanoparticles to spesific cells is essential to release the cargo at the desired region without lossing its stability.

After the optimization studies, morphological and chemical characterizations were conducted for the synthesized Ch-NPs. Comparative FT-IR and NMR spectra showed that the synthesized nanoparticles contained peaks belonging to both STPP and pure chitosan polymer, proving that the nanoparticles were successfully obtained (Fig. 4.8 & 4.9). It is shown that these nanoparticles, which are shown to have positive surface charge, are spherical polymeric structures in morphological analysis and show a steadier size profile especially in acidic environments, prepresenting the neuro-inflammation area.

In the literature, it is known that more advantageous drug delivery systems can be designed by utilizing the multivalence effect by attaching targeting groups to the surface of nanoparticles in which these small drug molecules are encapsulated and trapped instead of attaching targeting groups to the small molecule directly (135). In order to take advantage of this effect, a multivalency of chitosan polymer was utilized for conjugating more than one anti-oxidant drug molecule (α-Lipoic acid) to the side branches via ester bonds formed between the hydroxyl groups of chitosan and the carboxyl groups of LA (LA-Ch). FT-IR and NMR spcetra confirmed the successful incorporation of LA to the chitosan, as indicated by the presence of characteristic ester bond peaks (Fig. 4.12 & 4.13).

Obtained LA-Ch conjugate was used to synthesize drug-loaded nanoparticles. LA-Ch-NPs were synthesized as given in the Section 4.1.2.2. Regarding the DLS measurements, LA-Ch-NPs demonstrated comparable size and PDI% to Ch-NPs, ([Diameter nm]/[PDI%] : 139.6/10.14). Unlike Ch-NPs, aggregates formed after the

synthesis of drug-loaded nanoparticles were eliminated using Amicon ultracentrifuge tubes. The amount of drug that was loaded into LA-Ch-NPs were determined by LC-MS/MS anaysis, and a time dependent drug release study was performed, which revealed a controlled and sustained release in both physiological (pH 7.4) and acidic (pH 5.5) conditions. Notably, drug-loaded nanoparticles demonstrated a significantly slower and more continuous drug release in the inflammatory environment (pH 5.5) for up to nearly two weeks, while negligible release was observed in the neutral environment (pH 7.4). Furthermore, the black and blue lines in the graph (Fig. 4.16) demonstrate the sensitivity of ester bonds in the structure of the drug-conjugated polymer, as can be interpreted from the rapid release in media containing esterase enzyme.

Subsequently, selected Cy3 dye, a fluorescent dye in the infrared region (ex550/em570), was covalently attached to the surface of the nanoparticles to track the nanoparticles for *in vitro* studies, using primary amine groups on the surface of the Ch-NPs as described in Section 4.1.3. The amount of dye bound to the nanoparticles was calculated by Varioskan and Nanodrop instruments, for which the results are given in the Appendices. After the conjugation of the flourescent dye molecule, DLS analysis was carried out as in Figure 29. The hydrodynamic diameter of Cy3-Ch-NP was found as 155.4 nm.

Zeta potential analysis was performed for surface charge measurement for all synthesized base nanoparticles (Ch-NP, LA-Ch-NP, and Cy3-Ch-NP). The results revealed a positive surface charge (+14.2 ± 4.03 mV) for Ch-NPs attributed to the free amine groups of chitosan. This positive charge is required to enhance cellular uptake and interaction with negatively charged cell membranes (136). However, upon conjugation with lipoic acid (LA), the surface charge shifted to a negative value (-10.0 ± 6.40 mV), indicating successful drug incorporation and the presence of electronegative atoms in LA structure. Similarly, the conjugation of Cy3 fluorescent dye resulted in a more negative charge (-31.1 ± 6.14 mV) due to an additional carboxylic group of dye, confirming successful surface modification.

For targeted nanoparticle preparation, the first step in this thesis project involved selecting the T7 (HAIYPRH) peptide as the BBB-targeting moiety. This peptide exhibits a high affinity for the transferrin receptor (TfR), facilitating translocation across the blood-brain barrier via receptor-mediated endocytosis, a mechanism demonstrated in the literature to be effective for BBB penetration (137). To improve the suspension properties of the nanoparticles in aqueous media and eliminate nonspecific protein interactions, the T7 peptide was modified with a PEG polymer, synthesizing a T7-PEG-conjugated polymer.

First, T7 peptide was synthesized via solid phase peptide synthesis as described in the Section 3.2.4.1. Following the synthesis, obtaned peptide was characterized as given in Section 4.1.4.1 by LC-MS/MS, HPLC, FT-IR and ^{1}H-NMR spectroscopies. The T7 peptide was conjugated to a hetero-functional PEG linker containing both amine (-NH_2) and thiol (-SH) groups. The conjugation strategy involved first reacting the primary amine of PEG with the carboxyl group of the T7 peptide via NHS-EDCI chemistry, forming a stable amide bond. The thiol-terminated end of the PEG linker was subsequently modified with an NHS-activated disulfide-containing group, facilitating attachment to chitosan nanoparticles via thiol-disulfide exchang reaction. The successful formation of the T7-PEG-$_{S\text{-}S}$-NHS conjugate was confirmed through HPLC, FT-IR, and ^{1}H-NMR analyses, which verified the presence of key functional groups from the peptide, PEG, and NHS ester moieties. The FT-IR spectrum displayed characteristic peaks corresponding to PEG (-C-O at 1106 cm^{-1}), amide bonds (-C=O at 1657 cm^{-1}), and disulfide (-S-S- at 655 cm^{-1}), confirming successful synthesis. ^{1}H-NMR further revealed the expected signals for the peptide's aromatic protons, the PEG's methylene protons, and the NHS ester group.

In order to demonstrate the "peelability" of the T7-PEG peptide conjugate, a "peelability" experiment was performed by incubating Ch-NPs prepared with T7-PEG conjugate (T7-Ch-NPs) with glutathione-SH (reduced-GSH) under acidic conditions. The prepared T7-Ch-NPs were diluted in water to concentrations of 0.2 mM and 1 mM, and 1 mL of the prepared reduced GSH (rGSH) solution was added to 1 mL of

T7-Ch-NPs and reacted for 60 minutes. DLS measurements of the nanoparticles were taken at 5-minute intervals. As a result of this 60-minute experiment in which the blank nanoparticle without T7-PEG-S-S-NHS attached to its surface and the synthesized T7-PEG conjugated nanoparticles were used as a control group, when the sizes of the nanoparticles reacted at a concentration of 0.2 mM were evaluated, as shown in the graph in Figure 47, it was observed that the T7-PEG-S-S-NHS in the shell part peeled at the 30^{th} and 50^{th} minutes. The nanoparticles reached the size of their unmodified state, proving the "peelability" of the nanoparticles in the inflammatory environment.

In order to precisely deliver the obtained drug-loaded nanoparticles to the target microglia cells in the inflamed area, anti-CD11b-antibody, which can bind selectively and with high affinity to the CD11b receptor expressed specifically for that cell on the outer walls of activated microglia cells, the number of which increases in the inflammation environment caused by spinal cord injuries, was selected as a microglia targeting group (138). Thus, the chance of selectively targeting the drug was increased by directing the drug-loaded chitosan nanoparticles to the target cell (active microglia). The anti-DC11b-antibody, whose free carboxylic acid functional groups were activated by NHS ester, the conjugation process was facilitated using EDC/NHS chemistry at an optimized [Antibody]:[EDC/NHS] ratio of 1:10, and Cy3-Ch-NPs covalently bound to the surface of the nanoparticles via amide bonds formed as mention in the Section 4.1.4.3. DLS measurements confirmed that the additional filtration step reduced both the size and PDI of the nanoparticles, yielding a final particle size of approximately 155.6 nm. Zeta potential analysis showed a charge shift from -31.1 mV (Cy3-Ch-NPs) to +19.6 mV after antibody conjugation, indicating successful surface modification. SEM and TEM imaging further demonstrated that the antibody-conjugated nanoparticles maintained their spherical morphology. BCA protein quantification revealed that 14% of the 50 μg of antibody introduced into the nanoparticle solution was successfully bound. This binding efficiency was considered adequate for effective microglia targeting while preserving nanoparticle stability.

The cytotoxicty evaluation of the prepared empty and drug-loaded nanoparticles (Ch-NPs and LA-Ch-NPs) and peptide-conjugate and free drug molecules (LA and T7-PEG-ss-NHS) were performed using the CCK-8 assay kit for the Mouse microglial EOC-20 (*ATCC CRL-2469*) and Mouse skin fibroblast L929 (*ATCC CCL-1*) cell lines. Cytotoxicity data were represented as mean ± SD and analysis with two-way ANOVA by performing 3 replicates(n=3) viaGraphpad Prism, and p values of each graph were evaluated statistically significant ($p < 0.0001$).

The results indicate that chitosan nanoparticles (Ch-NPs), which were formed by physically cross-linking chitosan chains with the STPP cross-linker and subsequently purified and size-optimized, did not exhibit toxic effects, regardless of the amount (Fig. 4.35). In contrast, the PEG-based conjugate containing the T7 peptide, which was synthesized and purified for attaching to the surface, demonstrated dose-dependent cytotoxicity. This finding highlights the importance of optimizing the amount of peptide bound to the nanoparticle. As shown in Figure 4.36, the conjugate reduced cell viability at doses exceeding 25 μg/mL in a dose-dependent manner. Additionally, the results revealed that free drug molecules did not induce toxic effects, aligning with the findings in the literature (139). The synthesized drug-containing nanoparticles exhibited dose-dependent toxicity on microglia cells. Specifically, no toxic effects were observed at concentrations of 175 μM and below; however, a significant reduction in cell viability was noted at the highest applied dose of 350 μM (Fig. 4.37).

As a result of all the studies carried out in this thesis project, a 152 nm nanoparticle that has a high potential to enable the targeting of anti-inflammatory and antioxidant drug active ingredient to the brain for the treatment of brain damage due to neuroinflammation, surrounded by a peelable polymeric shell only in the inflammation area. Then these NPs are expected to accumulate in active microglia. Dual-targeted, controlled and continuous drug release will provide the reduction in side effects for healthy tissues (140).

6. CONCLUSION

In conclusion, the studies carried out in this thesis project focuses on the optimization and characterization of chitosan-based nanoparticles for BBB and microglia-targeted drug delivery. The results, supported in the light of the knowledge in the literature, emphasize the importance of molecular weight selection, reaction time, crosslinker concentration, filtration techniques and targeting group choice in obtaining nanoparticles with desired physicochemical and bioactive properties. Furthermore, targeted functionalization strategies involving T7 peptide and anti-CD11b antibody offer promising potential to enhance nanoparticle transport across the BBB and target the site of neuroinflammation. In this context, the platform presented in the thesis project is a unique design with an unprecedented design in the literature regarding polymer-drug combination and targeting neuroinflammation in the brain with dual targeting groups, which act sequentially due to the peel-off design of nanoparticles. Future studies will be continued with a focus on *in vivo* evaluations to assess the efficacy of these nanoparticles in neurological disease models.

7. REFERENCES

1. Wang J, Xia Q. Alpha-lipoic acid-loaded nanostructured lipid carrier: sustained release and biocompatibility to HaCaT cells in vitro. Drug Deliv [Internet]. 2014 [cited 2024 Dec 16];21(5):328–41. Available from: https://www.tandfonline.com/doi/abs/10.3109/10717544.2013.846435

2. U.S. Food and Drug Administration. (n.d.). https://www.fda.gov/drugs/drug-approvals-and-databases/drugsfda-glossary-terms. 2017. U.S. Food and Drug Administration. (n.d.). Drugs@FDA glossary of terms. FDA.

3. Tibbitt MW, Dahlman JE, Langer R. Emerging Frontiers in Drug Delivery. Vol. 138, Journal of the American Chemical Society. American Chemical Society; 2016. p. 704–17.

4. Sultana A, Zare M, Thomas V, Kumar TSS, Ramakrishna S. Nano-based drug delivery systems: Conventional drug delivery routes, recent developments and future prospects. Vol. 15, Medicine in Drug Discovery. Elsevier B.V.; 2022.

5. Jain KK. Current status and future prospects of drug delivery systems. In: Methods in Molecular Biology. Humana Press Inc.; 2014. p. 1–56.

6. Hashida M. Advocation and advancements of EPR effect theory in drug delivery science: A commentary. Vol. 346, Journal of Controlled Release. Elsevier B.V.; 2022. p. 355–7.

7. Fahmy MD, Jazayeri HE, Razavi M, Hashemi M, Omidi M, Farahani M, et al. Biomedical Applications of Intelligent Nanomaterials. 2017.

8. Park H, Otte A, Park K. Evolution of drug delivery systems: From 1950 to 2020 and beyond. Journal of Controlled Release. 2022 Feb 1;342:53–65.

9. Yun YH, Lee BK, Park K. Controlled Drug Delivery: Historical perspective for the next generation. Journal of Controlled Release. 2015 Dec 10;219:2–7.

10. Sung YK, Kim SW. Recent advances in polymeric drug delivery systems. Vol. 24, Biomaterials Research. BioMed Central Ltd; 2020.

11. Mainardes RM, Silva LP. Drug Delivery Systems: Past, Present, and Future. Vol. 5, Current Drug Targets. 2004.

12. Lager RS, Peppas NA. Present and future applications of biomaterials in controlled drug delivery systems. Biomaterials. 1981.

13. Pattni BS, Torchilin VP. Targeted Drug Delivery Systems: Strategies and Challenges. In 2015. p. 3–38.

14. Rehman N, Pandey A. Nano-Based Drug Delivery System. In: Engineered Nanoparticles as Drug Delivery Systems. Boca Raton: CRC Press; 2022. p. 3–9.

15. Tewabe A, Abate A, Tamrie M, Seyfu A, Siraj EA. Targeted drug delivery — from magic bullet to nanomedicine: Principles, challenges, and future perspectives. Vol. 14, Journal of Multidisciplinary Healthcare. Dove Medical Press Ltd; 2021. p. 1711–24.

16. Yu MK, Park J, Jon S. Targeting strategies for multifunctional nanoparticles in cancer imaging and therapy. Vol. 2, Theranostics. 2012. p. 3–44.

17. Jasim A, Abdelghany S, Greish K. Current Update on the Role of Enhanced Permeability and Retention Effect in Cancer Nanomedicine. Nanotechnology-Based Approaches for Targeting and Delivery of Drugs and Genes. 2017 Jan 1;62–109.

18. Matsumoto Y, Nichols JW, Toh K, Nomoto T, Cabral H, Miura Y, et al. Vascular bursts enhance permeability of tumour blood vessels and improve nanoparticle delivery. Nature Nanotechnology 2016 11:6 [Internet]. 2016 Feb 15 [cited 2024 Dec 8];11(6):533–8. Available from: https://www.nature.com/articles/nnano.2015.342

19. Liu Y, Hui Y, Ran R, Yang GZ, Wibowo D, Wang HF, et al. Synergetic Combinations of Dual-Targeting Ligands for Enhanced In Vitro and In Vivo Tumor Targeting. Adv Healthc Mater. 2018 Aug 8;7(15).

20. Wang J, Wang H, Li J, Liu Z, Xie H, Wei X, et al. IRGD-Decorated Polymeric Nanoparticles for the Efficient Delivery of Vandetanib to Hepatocellular Carcinoma: Preparation and in Vitro and in Vivo Evaluation. ACS Appl Mater Interfaces. 2016 Aug 3;8(30):19228–37.

21. Yoo J, Park C, Yi G, Lee D, Koo H. Active targeting strategies using biological ligands for nanoparticle drug delivery systems. Cancers (Basel). 2019 May 1;11(5).

22. Nimjee SM, White RR, Becker RC, Sullenger BA. Aptamers as Therapeutics. Annu Rev Pharmacol Toxicol [Internet]. 2017 Jan 6 [cited 2024 Dec 20];57(Volume 57, 2017):61–79. Available from: https://www.annualreviews.org/content/journals/10.1146/annurev-pharmtox-010716-104558

23. Li L, Xu S, Yan H, Li X, Yazd HS, Li X, et al. Nucleic Acid Aptamers for Molecular Diagnostics and Therapeutics: Advances and Perspectives. Angewandte Chemie International Edition [Internet]. 2021 Feb 1 [cited 2024 Dec 20];60(5):2221–31. Available from: https://onlinelibrary.wiley.com/doi/full/10.1002/anie.202003563

24. Lin HC, Li WT, Madanayake TW, Tao C, Niu Q, Yan SQ, et al. Aptamer-guided upconversion nanoplatform for targeted drug delivery and near-infrared light-triggered photodynamic therapy. https://doi.org/101177/0885328219882152 [Internet]. 2019 Oct 17 [cited 2024 Dec 20];34(6):875–88. Available from: https://journals.sagepub.com/doi/10.1177/0885328219882152

25. Wu Q, Wei X, Chen F, Huang M, Zhang S, Zhu L, et al. Aptamer-Assisted Blockade of the Immune Suppressor Sialic Acid-Binding Immunoglobulin-Like Lectin-15 for Cancer Immunotherapy. Angewandte Chemie [Internet]. 2023 Dec 21 [cited 2024 Dec 20];135(52):e202312609. Available from: https://onlinelibrary.wiley.com/doi/full/10.1002/ange.202312609

26. Kim DM, Kim M, Park H Bin, Kim KS, Kim DE. Anti-MUC1/CD44 Dual-Aptamer-Conjugated Liposomes for Cotargeting Breast Cancer Cells and Cancer Stem Cells. ACS Appl Bio Mater [Internet]. 2019 Oct 21 [cited 2024 Dec 20];2(10):4622–33. Available from: https://pubs.acs.org/doi/full/10.1021/acsabm.9b00705

27. Tan Y, Li Y, Qu YX, Su Y, Peng Y, Zhao Z, et al. Aptamer-Peptide Conjugates as Targeted Chemosensitizers for Breast Cancer Treatment. ACS Appl Mater Interfaces [Internet]. 2021 Mar 3 [cited 2024 Dec 20];13(8):9436–44. Available from: https://pubs.acs.org/doi/full/10.1021/acsami.0c18282

28. Li J, Wang Y, Zhu Y, Oupický D. Recent advances in delivery of drug–nucleic acid combinations for cancer treatment. Journal of Controlled Release. 2013 Dec 10;172(2):589–600.

29. Gomes-Da-Silva LC, Fonseca NA, Moura V, Pedroso De Lima MC, Simões S, Moreira JN. Lipid-based nanoparticles for siRNA delivery in cancer therapy: Paradigms and challenges. Acc Chem Res [Internet]. 2012 Jul 17 [cited 2024 Dec 20];45(7):1163–71. Available from: https://pubs.acs.org/doi/full/10.1021/ar300048p

30. Baker A, Lorch J, VanderWeele D, Zhang B. Smart Nanocarriers for the Targeted Delivery of Therapeutic Nucleic Acid for Cancer Immunotherapy. Pharmaceutics 2023, Vol 15, Page 1743 [Internet]. 2023 Jun 15 [cited 2024 Dec 20];15(6):1743. Available from: https://www.mdpi.com/1999-4923/15/6/1743/htm

31. Gao Y, Liu X, Chen N, Yang X, Tang F. Recent Advance of Liposome Nanoparticles for Nucleic Acid Therapy. Pharmaceutics 2023, Vol 15, Page 178 [Internet]. 2023 Jan 4 [cited 2024 Dec 20];15(1):178. Available from: https://www.mdpi.com/1999-4923/15/1/178/htm

32. Lu Z, Long Y, Cun X, Wang X, Li J, Mei L, et al. A size-shrinkable nanoparticle-based combined anti-tumor and anti-inflammatory strategy for enhanced cancer therapy.

Nanoscale [Internet]. 2018 May 31 [cited 2024 Dec 20];10(21):9957–70. Available from: https://pubs.rsc.org/en/content/articlehtml/2018/nr/c8nr01184b

33. Clark AJ, Davis ME. Increased brain uptake of targeted nanoparticles by adding an acid-cleavable linkage between transferrin and the nanoparticle core. Proc Natl Acad Sci U S A [Internet]. 2015 Oct 6 [cited 2024 Dec 20];112(40):12486–91. Available from: https://www.pnas.org/doi/abs/10.1073/pnas.1517048112

34. Feynman RP. Plenty of Room at the Bottom. In: APS Annual Meeting. Boston, MA, USA; 1959. p. 1–7.

35. Khan I, Saeed K, Khan I. Nanoparticles: Properties, applications and toxicities. Vol. 12, Arabian Journal of Chemistry. Elsevier B.V.; 2019. p. 908–31.

36. Sajid M, Płotka-Wasylka J. Nanoparticles: Synthesis, characteristics, and applications in analytical and other sciences. Vol. 154, Microchemical Journal. Elsevier Inc.; 2020.

37. Yetisgin AA, Cetinel S, Zuvin M, Kosar A, Kutlu O. Therapeutic nanoparticles and their targeted delivery applications. Vol. 25, Molecules. MDPI AG; 2020.

38. Selmani A, Kovačević D, Bohinc K. Nanoparticles: From synthesis to applications and beyond. Vol. 303, Advances in Colloid and Interface Science. Elsevier B.V.; 2022.

39. Sindhwani S, Chan WCW. Nanotechnology for modern medicine: next step towards clinical translation. Vol. 290, Journal of Internal Medicine. John Wiley and Sons Inc; 2021. p. 486–98.

40. Nikezić AVV, Bondžić AM, Vasić VM. Drug delivery systems based on nanoparticles and related nanostructures. Vol. 151, European Journal of Pharmaceutical Sciences. Elsevier B.V.; 2020.

41. Senapati S, Mahanta AK, Kumar S, Maiti P. Controlled drug delivery vehicles for cancer treatment and their performance. Signal Transduct Target Ther. 2018 Mar 16;3(1):7.

42. Mu W, Chu Q, Liu Y, Zhang N. A Review on Nano-Based Drug Delivery System for Cancer Chemoimmunotherapy. Vol. 12, Nano-Micro Letters. Springer; 2020.

43. Chen D, Liu X, Lu X, Tian J. Nanoparticle drug delivery systems for synergistic delivery of tumor therapy. Vol. 14, Frontiers in Pharmacology. Frontiers Media S.A.; 2023.

44. Mitchell MJ, Billingsley MM, Haley RM, Wechsler ME, Peppas NA, Langer R. Engineering precision nanoparticles for drug delivery. Vol. 20, Nature Reviews Drug Discovery. Nature Research; 2021. p. 101–24.

45. Patra JK, Das G, Fraceto LF, Campos EVR, Rodriguez-Torres MDP, Acosta-Torres LS, et al. Nano based drug delivery systems: Recent developments and future prospects. Vol. 16, Journal of Nanobiotechnology. BioMed Central Ltd; 2018.

46. Singh R, Lillard JW. Nanoparticle-based targeted drug delivery. Vol. 86, Experimental and Molecular Pathology. 2009. p. 215–23.

47. Dong Z, Shen Y, Zhao S, Wang X, Han M, Zhao N, et al. Influence of Hydrophobic Chains in Nanocarriers on Antitumor Efficacy of Docetaxel Nanoparticles. Mol Pharm [Internet]. 2020 Apr 6 [cited 2024 Dec 24];17(4):1205–14. Available from: https://pubs.acs.org/doi/abs/10.1021/acs.molpharmaceut.9b01228

48. Zhang Y, Teh C, Li M, Ang CY, Tan SY, Qu Q, et al. Acid-responsive polymeric doxorubicin prodrug nanoparticles encapsulating a near-infrared dye for combined photothermal-chemotherapy. Chemistry of Materials [Internet]. 2016 Oct 11 [cited 2024 Dec 24];28(19):7039–50. Available from: https://pubs.acs.org/doi/abs/10.1021/acs.chemmater.6b02896

49. Wu Y, Xiao Y, Huang Y, Xu Y, You D, Lu W, et al. Rod-Shaped Micelles Based on PHF-g-(PCL-PEG) with pH-Triggered Doxorubicin Release and Enhanced Cellular Uptake. Biomacromolecules [Internet]. 2019 Mar 11 [cited 2024 Dec 24];20(3):1167–77. Available from: https://pubs.acs.org/doi/abs/10.1021/acs.biomac.8b01430

50. Yang L, Sun H, Liu Y, Hou W, Yang Y, Cai R, et al. Self-Assembled Aptamer-Grafted Hyperbranched Polymer Nanocarrier for Targeted and Photoresponsive Drug Delivery. Angewandte Chemie [Internet]. 2018 Dec 21 [cited 2024 Dec 24];130(52):17294–8. Available from: https://onlinelibrary.wiley.com/doi/full/10.1002/ange.201809753

51. Elmowafy M, Shalaby K, Elkomy MH, Alsaidan OA, Gomaa HAM, Abdelgawad MA, et al. Polymeric Nanoparticles for Delivery of Natural Bioactive Agents: Recent Advances and Challenges. Vol. 15, Polymers. MDPI; 2023.

52. Sershen S, West J. Implantable, polymeric systems for modulated drug delivery. Adv Drug Deliv Rev. 2002;54(9):1225–35.

53. Boni R, Ali A, Shavandi A, Clarkson AN. Current and novel polymeric biomaterials for neural tissue engineering. Vol. 25, Journal of Biomedical Science. BioMed Central Ltd.; 2018.

54. El-Say KM, El-Sawy HS. Polymeric nanoparticles: Promising platform for drug delivery. Vol. 528, International Journal of Pharmaceutics. Elsevier B.V.; 2017. p. 675–91.

55. Baig N, Kammakakam I, Falath W, Kammakakam I. Nanomaterials: A review of synthesis methods, properties, recent progress, and challenges. Vol. 2, Materials Advances. Royal Society of Chemistry; 2021. p. 1821–71.

56. Beach MA, Nayanathara U, Gao Y, Zhang C, Xiong Y, Wang Y, et al. Polymeric Nanoparticles for Drug Delivery. Vol. 124, Chemical Reviews. American Chemical Society; 2024. p. 5505–616.

57. Thang NH, Chien TB, Cuong DX. Polymer-Based Hydrogels Applied in Drug Delivery: An Overview. Vol. 9, Gels. Multidisciplinary Digital Publishing Institute (MDPI); 2023.

58. Guo P, Martin CR, Zhao Y, Ge J, Zare RN. General method for producing organic nanoparticles using nanoporous membranes. Nano Lett [Internet]. 2010 Jun 9 [cited 2025 Jan 27];10(6):2202–6. Available from: https://pubs.acs.org/doi/abs/10.1021/nl101057d

59. Rodriguez-Córdova RJ, Hernández-Giottonini KY, Gutiérrez-Valenzuela CA, De la Vega J, Esquivel R, Zavala-Rivera P, et al. Preparation of PLGA Nanoparticles Loaded with Oxytetracycline Hydrochloride for its Possible Application Against Brucellosis Infection. Microscopy and Microanalysis [Internet]. 2018 Aug 1 [cited 2025 Jan 27];24(S1):1418–9. Available from: https://dx.doi.org/10.1017/S1431927618007572

60. Rinaudo M. Chitin and chitosan: Properties and applications. Prog Polym Sci. 2006 Jul 1;31(7):603–32.

61. Makadia HK, Siegel SJ. Poly Lactic-co-Glycolic Acid (PLGA) as biodegradable controlled drug delivery carrier. Polymers (Basel). 2011 Sep;3(3):1377–97.

62. Rodriguez-Córdova RJ, Hernández-Giottonini KY, Gutiérrez-Valenzuela CA, De la Vega J, Esquivel R, Zavala-Rivera P, et al. Preparation of PLGA Nanoparticles Loaded with Oxytetracycline Hydrochloride for its Possible Application Against Brucellosis Infection. Microscopy and Microanalysis. 2018 Aug;24(S1):1418–9.

63. Yang F, Cabe M, Nowak HA, Langert KA. Chitosan/poly(lactic-co-glycolic)acid Nanoparticle Formulations with Finely-Tuned Size Distributions for Enhanced Mucoadhesion. Pharmaceutics. 2022 Jan 1;14(1).

64. Vahab SA, K I A, M S, Kumar VS. Exploring chitosan nanoparticles for enhanced therapy in neurological disorders: a comprehensive review. Naunyn-Schmiedeberg's Archives of Pharmacology. Springer Science and Business Media Deutschland GmbH; 2024.

65. Rinaudo M, Pavlov G, Desbrières J. Solubilization of Chitosan in Strong Acid Medium. International Journal of Polymer Analysis and Characterization. 1999;5(3):267–76.

66. Aranaz I, Alcántara AR, Civera MC, Arias C, Elorza B, Caballero AH, et al. Chitosan: An overview of its properties and applications. Vol. 13, Polymers. MDPI; 2021.

67. Ahmed TA, Aljaeid BM. Preparation, characterization, and potential application of chitosan, chitosan derivatives, and chitosan metal nanoparticles in pharmaceutical drug delivery. Vol. 10, Drug Design, Development and Therapy. Dove Medical Press Ltd.; 2016. p. 483–507.

68. Bozuyuk U, Yasa O, Yasa IC, Ceylan H, Kizilel S, Sitti M. Light-Triggered Drug Release from 3D-Printed Magnetic Chitosan Microswimmers. ACS Nano. 2018 Sep 25;12(9):9617–25.

69. Hoang NH, Thanh T Le, Sangpueak R, Treekoon J, Saengchan C, Thepbandit W, et al. Chitosan Nanoparticles-Based Ionic Gelation Method: A Promising Candidate for Plant Disease Management. Vol. 14, Polymers. MDPI; 2022.

70. Nguyen TV, Nguyen TTH, Wang SL, Vo TPK, Nguyen AD. Preparation of chitosan nanoparticles by TPP ionic gelation combined with spray drying, and the antibacterial activity of chitosan nanoparticles and a chitosan nanoparticle–amoxicillin complex. Research on Chemical Intermediates. 2017 Jun 1;43(6):3527–37.

71. Yadav M, Kaushik B, Rao GK, Srivastava CM, Vaya D. Advances and challenges in the use of chitosan and its derivatives in biomedical fields: A review. Vol. 5, Carbohydrate Polymer Technologies and Applications. Elsevier Ltd; 2023.

72. Suk JS, Xu Q, Kim N, Hanes J, Ensign LM. PEGylation as a strategy for improving nanoparticle-based drug and gene delivery. Vol. 99, Advanced Drug Delivery Reviews. Elsevier B.V.; 2016. p. 28–51.

73. Liang M, Gao C, Wang Y, Gong W, Fu S, Cui L, et al. Enhanced blood–brain barrier penetration and glioma therapy mediated by T7 peptide-modified low-density lipoprotein particles. Drug Deliv. 2018;25(1):1652–63.

74. Akojwar N, Mishra A, Mishra P, Tekade M, Mule SR, Tekade RK. PEGylation of Therapeutic Proteins and Peptides. In: PEGylated Nanocarriers in Medicine and Pharmacy. Singapore: Springer Nature Singapore; 2025. p. 317–43.

75. Choi B, Soh M, Manandhar Y, Kim D, Han SI, Baik S, et al. Highly selective microglial uptake of ceria-zirconia nanoparticles for enhanced analgesic treatment of neuropathic pain. Nanoscale. 2019 Nov 7;11(41):19437–47.

76. Zhao N, Francis NL, Calvelli HR, Moghe P V. Microglia-targeting nanotherapeutics for neurodegenerative diseases. Vol. 4, APL Bioengineering. American Institute of Physics Inc.; 2020.

77. Al Gailani M, Liu M, Wen J. Ligands for oral delivery of peptides across the blood-brain-barrier. Acta Materia Medica. 2022;1(1):106–23.

78. Lee BS, Yuan X, Xu Q, McLafferty FS, Petersen BA, Collette JC, et al. Stimuli-responsive antioxidant nanoprodrugs of NSAIDs. Int J Pharm. 2009 May 8;372(1–2):112–24.

79. Xue Y, Bai H, Peng B, Fang B, Baell J, Li L, et al. Stimulus-cleavable chemistry in the field of controlled drug delivery. Vol. 50, Chemical Society Reviews. Royal Society of Chemistry; 2021. p. 4872–931.

80. Ulbrich K, Holá K, Šubr V, Bakandritsos A, Tuček J, Zbořil R. Targeted Drug Delivery with Polymers and Magnetic Nanoparticles: Covalent and Noncovalent Approaches, Release Control, and Clinical Studies. Vol. 116, Chemical Reviews. American Chemical Society; 2016. p. 5338–431.

81. Candelario-Jalil E, Dijkhuizen RM, Magnus T. Neuroinflammation, Stroke, Blood-Brain Barrier Dysfunction, and Imaging Modalities. Vol. 53, Stroke. Lippincott Williams and Wilkins; 2022. p. 1473–86.

82. Leng F, Hinz R, Gentleman S, Hampshire A, Dani M, Brooks DJ, et al. Neuroinflammation is independently associated with brain network dysfunction in Alzheimer's disease. Mol Psychiatry. 2023 Mar 1;28(3):1303–11.

83. Leng F, Hinz R, Gentleman S, Dani M, Brooks DJ, Edison P. Combined Neuroinflammation and Amyloid PET Markers in Predicting Disease Progression in Cognitively Impaired Subjects. Journal of Alzheimer's Disease. 2024 Jul 30;100(3):973–86.

84. Teoh NSN, Gyanwali B, Lai MKP, Chai YL, Chong JR, Chong EJY, et al. Association of Interleukin-6 and Interleukin-8 with Cognitive Decline in an Asian Memory Clinic Population. Journal of Alzheimer's Disease. 2023;92(2):445–55.

85. Kwon HS, Koh SH. Neuroinflammation in neurodegenerative disorders: the roles of microglia and astrocytes. Vol. 9, Translational Neurodegeneration. BioMed Central Ltd; 2020.

86. Kempuraj D, Thangavel R, Kempuraj DD, Ahmed ME, Selvakumar GP, Raikwar SP, et al. Neuroprotective effects of flavone luteolin in neuroinflammation and neurotrauma. Vol. 47, BioFactors. Blackwell Publishing Inc.; 2021. p. 190–7.

87. Chen X, Wu S, Chen C, Xie B, Fang Z, Hu W, et al. Omega-3 polyunsaturated fatty acid supplementation attenuates microglial-induced inflammation by inhibiting the

HMGB1/TLR4/NF-KB pathway following experimental traumatic brain injury. J Neuroinflammation. 2017 Jul 24;14(1).

88. Alawieh A, Chalhoub RM, Mallah K, Langley EF, York M, Broome H, et al. Complement drives synaptic degeneration and progressive cognitive decline in the chronic phase after traumatic brain injury. Journal of Neuroscience. 2021 Feb 24;41(8):1830–43.

89. Caplan HW, Prabhakara KS, Toledano Furman NE, Zorofchian S, Kumar A, Martin C, et al. Combination therapy with Treg and mesenchymal stromal cells enhances potency and attenuation of inflammation after traumatic brain injury compared to monotherapy. Stem Cells. 2021 Mar 1;39(3):358–70.

90. Corrigan F, Mander KA, Leonard A V., Vink R. Neurogenic inflammation after traumatic brain injury and its potentiation of classical inflammation. Vol. 13, Journal of Neuroinflammation. BioMed Central Ltd.; 2016.

91. Stuckey SM, Ong LK, Collins-praino LE, Turner RJ. Neuroinflammation as a key driver of secondary neurodegeneration following stroke? Vol. 22, International Journal of Molecular Sciences. MDPI; 2021.

92. Candelario-Jalil E, Dijkhuizen RM, Magnus T. Neuroinflammation, Stroke, Blood-Brain Barrier Dysfunction, and Imaging Modalities. Vol. 53, Stroke. Lippincott Williams and Wilkins; 2022. p. 1473–86.

93. Maida CD, Norrito RL, Daidone M, Tuttolomondo A, Pinto A. Neuroinflammatory mechanisms in ischemic stroke: Focus on cardioembolic stroke, background, and therapeutic approaches. Vol. 21, International Journal of Molecular Sciences. MDPI AG; 2020. p. 1–33.

94. Dzhauari S, Basalova N, Primak A, Balabanyan V, Efimenko A, Skryabina M, et al. The Secretome of Mesenchymal Stromal Cells in Treating Intracerebral Hemorrhage: The First Step to Bedside. Pharmaceutics. 2023 Jun 1;15(6).

95. Yin S, Ma X yue, Sun Y feng, Yin Y qing, Long Y, Zhao C lai, et al. RGS5 augments astrocyte activation and facilitates neuroinflammation via TNF signaling. J Neuroinflammation. 2023 Dec 1;20(1).

96. Glass CK, Saijo K, Winner B, Marchetto MC, Gage FH. Mechanisms Underlying Inflammation in Neurodegeneration. Vol. 140, Cell. Elsevier B.V.; 2010. p. 918–34.

97. Ferraris C, Cavalli R, Panciani PP, Battaglia L. Overcoming the blood–brain barrier: Successes and challenges in developing nanoparticle-mediated drug delivery systems

for the treatment of brain tumours. Vol. 15, International Journal of Nanomedicine. Dove Medical Press Ltd.; 2020. p. 2999–3022.

98. Wu D, Chen Q, Chen X, Han F, Chen Z, Wang Y. The blood–brain barrier: structure, regulation, and drug delivery. Vol. 8, Signal Transduction and Targeted Therapy. Springer Nature; 2023.

99. Daneman R, Prat A. The blood–brain barrier. Cold Spring Harb Perspect Biol. 2015 Jan 1;7(1).

100. Zlokovic B V. The Blood-Brain Barrier in Health and Chronic Neurodegenerative Disorders. Vol. 57, Neuron. 2008. p. 178–201.

101. Grabrucker AM, Ruozi B, Belletti D, Pederzoli F, Forni F, Vandelli MA, et al. Nanoparticle transport across the blood brain barrier. Vol. 4, Tissue Barriers. Taylor and Francis Inc.; 2016.

102. Osborne O, Peyravian N, Nair M, Daunert S, Toborek M. The Paradox of HIV Blood–Brain Barrier Penetrance and Antiretroviral Drug Delivery Deficiencies. Vol. 43, Trends in Neurosciences. Elsevier Ltd; 2020. p. 695–708.

103. Dabbagh F, Schroten H, Schwerk C. In Vitro Models of the Blood–Cerebrospinal Fluid Barrier and Their Applications in the Development and Research of (Neuro)Pharmaceuticals. Pharmaceutics. 2022;14(8):1729.

104. On NH, Kiptoo P, Siahaan TJ, Miller DW. Modulation of blood-brain barrier permeability in mice using synthetic E-cadherin peptide. Mol Pharm. 2014 Mar 3;11(3):974–81.

105. Sajesh B V., On NH, Omar R, Alrushaid S, Kopec BM, Wang WG, et al. Validation of Cadherin HAV6 Peptide in the transient modulation of the blood-brain barrier for the treatment of brain tumors. Pharmaceutics. 2019 Sep 1;11(9).

106. Ulapane KR, On N, Kiptoo P, Williams TD, Miller DW, Siahaan TJ. Improving brain delivery of biomolecules via bbb modulation in mouse and rat: Detection using mri, nirf, and mass spectrometry. Vol. 1, Nanotheranostics. Ivyspring International Publisher; 2017. p. 217–31.

107. Laksitorini MD, Kiptoo PK, On NH, Thliveris JA, Miller DW, Siahaan TJ. Modulation of intercellular junctions by cyclic-ADT peptides as a method to reversibly increase blood-brain barrier permeability. J Pharm Sci. 2015;104(3):1065–75.

108. Kumar V, Patiyal S, Dhall A, Sharma N, Raghava GPS. B3pred: A random-forest-based method for predicting and designing blood–brain barrier penetrating peptides. Pharmaceutics. 2021 Aug 1;13(8).

109. Stalmans S, Bracke N, Wynendaele E, Gevaert B, Peremans K, Burvenich C, et al. Cell-penetrating peptides selectively cross the blood-brain barrier in vivo. PLoS One. 2015 Oct 14;10(10).

110. Zhang Y, Zhai M, Chen Z, Han X, Yu F, Li Z, et al. Dual-modified liposome codelivery of doxorubicin and vincristine improve targeting and therapeutic efficacy of glioma. Drug Deliv. 2017;24(1):1045–55.

111. Wang F, Dong X, Xiu P, Zhong J, Wei H, Xu Z, et al. T7 peptide inhibits angiogenesis via downregulation of angiopoietin-2 and autophagy. Oncol Rep. 2015 Dec 1;33(2):675–84.

112. Zong T, Mei L, Gao H, Cai W, Zhu P, Shi K, et al. Synergistic dual-ligand doxorubicin liposomes improve targeting and therapeutic efficacy of brain glioma in animals. Mol Pharm. 2014 Jul 7;11(7):2346–57.

113. de Oliveira ECL, Hirmz H, Wynendaele E, Seixas Feio JA, Moreira IMS, da Costa KS, et al. BrainPepPass: A Framework Based on Supervised Dimensionality Reduction for Predicting Blood-Brain Barrier-Penetrating Peptides. J Chem Inf Model. 2024 Apr 8;64(7):2368–82.

114. Habib S, Singh M. Angiopep-2-Modified Nanoparticles for Brain-Directed Delivery of Therapeutics: A Review. Vol. 14, Polymers. MDPI; 2022.

115. Yang Y, Yang Y, Xie X, Cai X, Zhang H, Gong W, et al. PEGylated liposomes with NGR ligand and heat-activable cell-penetrating peptide-doxorubicin conjugate for tumor-specific therapy. Biomaterials. 2014 May;35(14):4368–81.

116. Wang Y, Zhang L, Liu C, Luo Y, Chen D. Peptide-Mediated Nanocarriers for Targeted Drug Delivery: Developments and Strategies. Vol. 16, Pharmaceutics. Multidisciplinary Digital Publishing Institute (MDPI); 2024.

117. Cui Y, Sun J, Hao W, Chen M, Wang Y, Xu F, et al. Dual-Target Peptide-Modified Erythrocyte Membrane-Enveloped PLGA Nanoparticles for the Treatment of Glioma. Front Oncol. 2020 Oct 21;10.

118. Hoyle CE, Lowe AB, Bowman CN. Thiol-click chemistry: a multifaceted toolbox for small molecule and polymer synthesis. Chem Soc Rev [Internet]. 2010 Mar 22 [cited 2024 Nov 9];39(4):1355–87. Available from: https://pubs.rsc.org/en/content/articlehtml/2010/cs/b901979k

119. Luceño-Sánchez JA, Díez-Pascual AM. Grafting of Polypyrrole-3-carboxylic Acid to the Surface of Hexamethylene Diisocyanate-Functionalized Graphene Oxide.

Nanomaterials 2019, Vol 9, Page 1095 [Internet]. 2019 Jul 31 [cited 2024 Nov 10];9(8):1095. Available from: https://www.mdpi.com/2079-4991/9/8/1095/htm

120. Kofuji K, Nakamura M, Isobe T, Murata Y, Kawashima S. Stabilization of α-lipoic acid by complex formation with chitosan. Food Chem. 2008 Jul 1;109(1):167–71.

121. Shen F, Zhong H, Ge W, Ren J, Wang X. Quercetin/chitosan-graft-alpha lipoic acid micelles: A versatile antioxidant water dispersion with high stability. Carbohydr Polym. 2020 Apr 15;234:115927.

122. Stawikowski M, Fields GB. Introduction to Peptide Synthesis. Curr Protoc Protein Sci [Internet]. 2012 Aug 1 [cited 2024 Dec 13];69(1):18.1.1-18.1.13. Available from: https://onlinelibrary.wiley.com/doi/full/10.1002/0471140864.ps1801s69

123. Navath RS, Wang B, Kannan S, Romero R, Kannan RM. Stimuli-responsive star poly(ethylene glycol) drug conjugates for improved intracellular delivery of the drug in neuroinflammation. Journal of Controlled Release. 2010 Mar 19;142(3):447–56.

124. Biswas S, Dodwadkar NS, Deshpande PP, Torchilin VP. Liposomes loaded with paclitaxel and modified with novel triphenylphosphonium-PEG-PE conjugate possess low toxicity, target mitochondria and demonstrate enhanced antitumor effects in vitro and in vivo. Journal of Controlled Release. 2012 May 10;159(3):393–402.

125. Sawtarie N, Cai Y, Lapitsky Y. Preparation of chitosan/tripolyphosphate nanoparticles with highly tunable size and low polydispersity. Colloids Surf B Biointerfaces. 2017 Sep 1;157:110–7.

126. Mahmood MA, Madni A, Rehman M, Rahim MA, Jabar A. Ionically cross-linked chitosan nanoparticles for sustained delivery of docetaxel: Fabrication, post-formulation and acute oral toxicity evaluation. Int J Nanomedicine. 2019;14:10035–46.

127. Leiva W, Toro N, Robles P, Gálvez E, Jeldres RI. Use of Multi-Anionic Sodium Tripolyphosphate to Enhance Dispersion of Concentrated Kaolin Slurries in Seawater. Metals 2021, Vol 11, Page 1085 [Internet]. 2021 Jul 7 [cited 2024 Dec 14];11(7):1085. Available from: https://www.mdpi.com/2075-4701/11/7/1085/htm

128. Pereira AGB, Muniz EC, Hsieh Y Lo. 1H NMR and 1H–13C HSQC surface characterization of chitosan–chitin sheath-core nanowhiskers. Carbohydr Polym. 2015 Jun 5;123:46–52.

129. Sahsuvar S, Guner R, Gok O, Can O. Development and pharmaceutical investigation of novel cervical cancer-targeting and redox-responsive melittin conjugates. Scientific Reports 2023 13:1 [Internet]. 2023 Oct 25 [cited 2024 Dec 1];13(1):1–15. Available from: https://www.nature.com/articles/s41598-023-45537-x

130. Tsai WH, Yu KH, Huang YC, Lee CI. EGFR-targeted photodynamic therapy by curcumin-encapsulated chitosan/TPP nanoparticles. Int J Nanomedicine. 2018 Feb 9;13:903–16.

131. Moura F, de Andrade K, Farias dos Santos J, Fonseca Goulart M. Lipoic Acid: Its Antioxidant and Anti-Inflammatory Role and Clinical Applications. Curr Top Med Chem. 2015 Feb 23;15(5):458–83.

132. Zhang F, Lin YA, Kannan S, Kannan RM. Targeting specific cells in the brain with nanomedicines for CNS therapies. Journal of Controlled Release. 2016 Oct 28;240:212–26.

133. Zhang W, Mehta A, Tong Z, Esser L, Voelcker NH. Development of Polymeric Nanoparticles for Blood–Brain Barrier Transfer—Strategies and Challenges. Vol. 8, Advanced Science. John Wiley and Sons Inc; 2021.

134. Ojeda-Hernández DD, Canales-Aguirre AA, Matias-Guiu J, Gomez-Pinedo U, Mateos-Díaz JC. Potential of Chitosan and Its Derivatives for Biomedical Applications in the Central Nervous System. Vol. 8, Frontiers in Bioengineering and Biotechnology. Frontiers Media S.A.; 2020.

135. Kumar B, Jalodia K, Kumar P, Gautam HK. Recent advances in nanoparticle-mediated drug delivery. Vol. 41, Journal of Drug Delivery Science and Technology. Editions de Sante; 2017. p. 260–8.

136. Augustine R, Hasan A, Primavera R, Wilson RJ, Thakor AS, Kevadiya BD. Cellular uptake and retention of nanoparticles: Insights on particle properties and interaction with cellular components. Vol. 25, Materials Today Communications. Elsevier Ltd; 2020.

137. Wei L, Guo XY, Yang T, Yu MZ, Chen DW, Wang JC. Brain tumor-targeted therapy by systemic delivery of siRNA with Transferrin receptor-mediated core-shell nanoparticles. Int J Pharm. 2016 Aug 20;510(1):394–405.

138. Wagner FB, Mignardot JB, Le Goff-Mignardot CG, Demesmaeker R, Komi S, Capogrosso M, et al. Targeted neurotechnology restores walking in humans with spinal cord injury. Nature. 2018;563(7729):65–93.

139. Tibullo D, Li Volti G, Giallongo C, Grasso S, Tomassoni D, Anfuso CD, et al. Biochemical and clinical relevance of alpha lipoic acid: antioxidant and anti-inflammatory activity, molecular pathways and therapeutic potential. Vol. 66, Inflammation Research. Birkhauser Verlag AG; 2017. p. 947–59.

140. Pondman K, Le Gac S, Kishore U. Nanoparticle-induced immune response: Health risk versus treatment opportunity? Immunobiology. 2023 Mar 1;228(2).

8. APPENDIX

Appendix 1. Calibration curves for prepared Cy3 dye solutions.

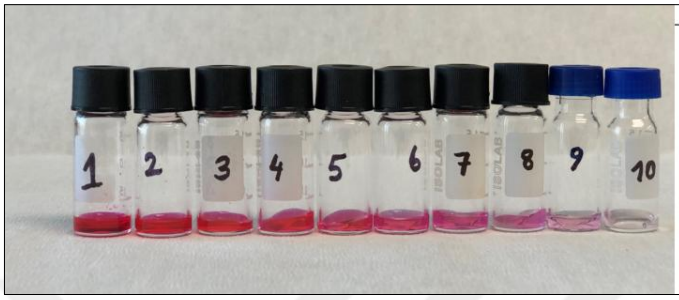

No	Conc. (µM)
1	1558,8
2	779,4232
3	389,7116
4	194,8558
5	97,4279
6	48,714
7	24,357
8	12,1785
9	6,0892
10	3,0446

Figure 8.1. Cy3 dye solutions at different concentrations prepared for the calibration curve.In the photograph, it can be seen that the Cy3 dye, which appears pink at visible wavelength, decreases in pinkness as the concentration decreases from left to right.

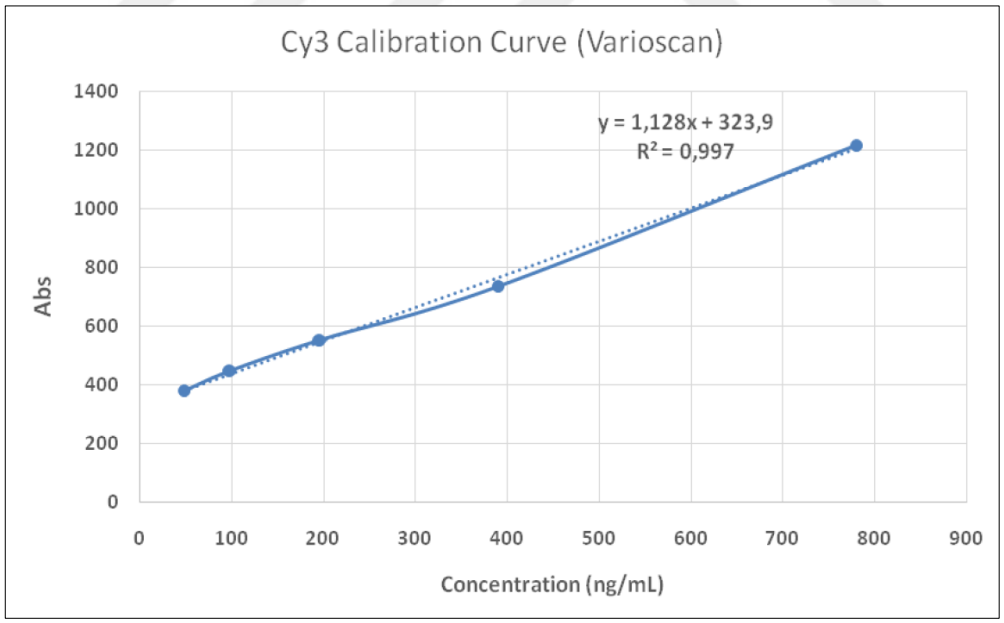

Figure 8.2. Calibration curve of Cy3 flourescent dye molecule on Vairoskan Flash.

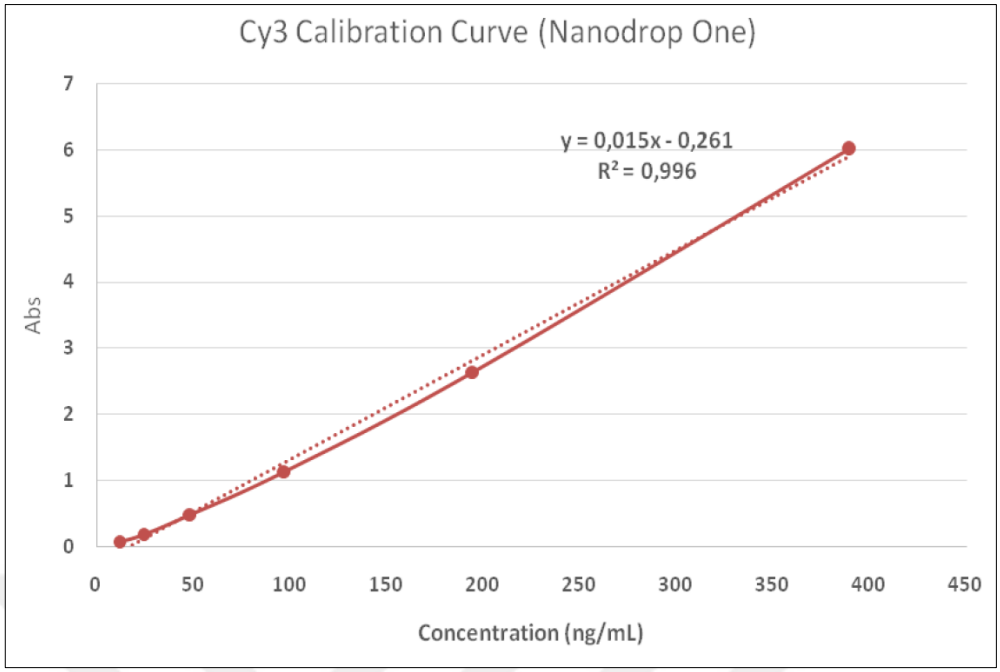

Figure 8.3. Calibration curve of Cy3 flourescent dye molecule on Nanodrop spectrophotometer.

Appendix 2. Calibration curve for BCA Assay.

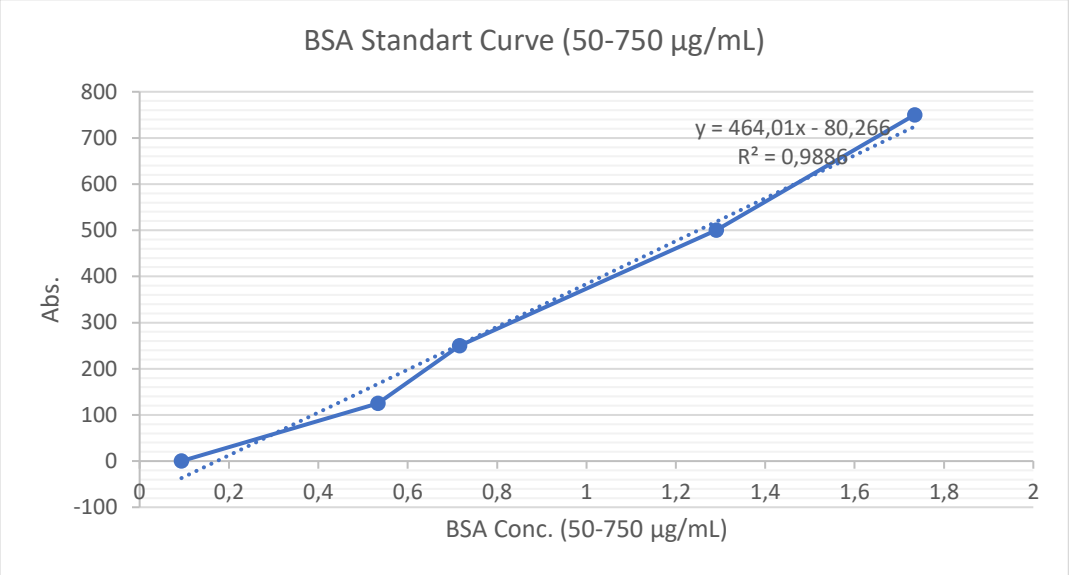

Figure 8.4. Calibration curve of BSA for BCA assay on Varioskan Flash.

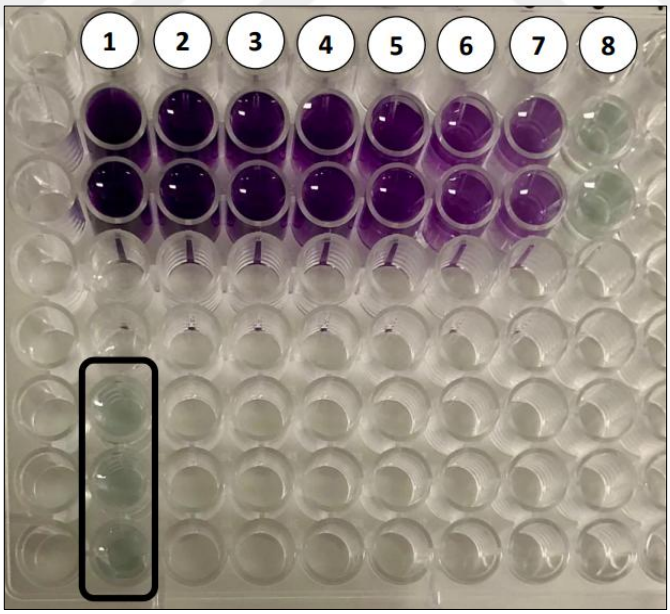

Figure 8.5. Calibration curve for BCA protein quantification method using the standards. Standards were prepared from high concentration to low concentration. (1) 2000 µg/mL, (2) 1500 µg/mL, (3) 1000 µg/mL, (4) 750 µg/mL, (5) 500 µg/mL, (6) 250 µg/mL, (7) 125 µg/mL and (8) 0 µg/mL. The prepared Cy3-Ant-Ch-NPs are shown in the section marked with a black box below.

9. CURRICULUM VITAE